# Experimental and Numerical Investigation of Solar Thermal Buffer Zone

# Experimental and Numerical Investigation of Solar Thermal Buffer Zone

**By**

**Asad M. Jan, B.Sc. Mechanical Engineering**

**A Thesis**

**Submitted to the School of Graduate Studies**

**In Partial Fulfillment of the Requirements**

**For the Degree**

**Master of Applied Science**

**McMaster University**

**Hamilton, Ontario, Canada**

**MASTER OF APPLIED SCIENCE (2013)** **McMaster University**

**(Mechanical Engineering)** **Hamilton, Ontario**

**TITLE:** **Experimental and Numerical Investigation of Solar Thermal Buffer Zone**

**AUTHOR:** **Asad M. Jan, BSc. Mech. Eng.**

**SUPERVISOR:** **Dr. Mohamed S. Hamed**

**CO-SUPERVISOR:** **Dr. Ghani Razaqpur**

**NUMBER OF PAGES:** **122**

## Abstract

Solar thermosiphons integrated into the thermal envelop of buildings has been studied for their potential to take advantage of solar energy in heating buildings. The annual performance of the Solar Thermal Buffer Zone cannot currently be predicted with the correlations from previous research. Also, no work has been done on using the thermal buffer zone with a natural convection for energy savings in a building even though it has the potential to provide heating. The goal of this project was to design, analyze and determine the feasibility of a thermal buffer zone in a building. A thermal buffer zone can be defined as a fluid filled cavity which envelopes a building. This cavity provides a building with additional insulation but also allows for collection of solar energy and to be distributed throughout the structure in order to heat the interior. To show the physical aspect, the flow visualization in the project, computational fluid dynamic (CFD) software was used which was experimentally not possible. A physical prototype was then designed and constructed in order to test the effectiveness of the TBZ.

This experiment included radiation as the heat source and the ability to vary geometric lengths. The performance parameters of mass flow rate were comparable between the numerical predictions and experimental results. However, due to uncertainties in the current experimental setup, full validation of the numerical model was not possible. These uncertainties would have to be addressed before the numerical model that was developed can be fully validated and used for generating correlations.

## Acknowledgements

I would like to thank my supervisor Dr. Mohamed S. Hamed, for his patience, guidance, advice and support throughout the project. I would also like to thank Dr. Ghani Razaqpur for his support and guidance during the project. I would like to thank all the technicians in the department, Joe, Mike, Ron, Mark and Jim for their help and advice. I would also like to acknowledge all the guys in the CFD lab, and the undergraduate group from when I started and up till the end. I need to thank Dr. Simon Foo of Public Works and Public Works Canada for their technical support and for allowing this work to happen through funding.

# Table of Contents

## List of Tables:

## List of Figures:

## List of Symbols:

| SYMBOL | DESCRIPTION | UNITS |
|---|---|---|
| $A_n$ | Calibration coefficient | $\frac{1}{V}$ |
| $C_p$ | Specific heat capacity | $\frac{J}{kg^oC}$ |
| $B$ | Spacing between glass and absorbing wall | $m$ |
| $e$ | Measured voltage | $V$ |
| $E$ | Inlet and outlet height | $m$ |
| $f()$ | Manufacturer provided calibration function | — |
| $g$ | Gravitational acceleration | $\frac{m}{s^2}$ |
| $Gr_H$ | Grashof number based on wall heating | — |
| $Gr_A$ | Grashof number based on air temperature | — |
| $h$ | Convection heat transfer coefficient | $\frac{W}{m^{2^o}C}$ |
| $H$ | Total cavity height | $m$ |
| $k$ | Thermal conductivity | $\frac{W}{m^oC}$ |
| $L$ | Spacing between glass and illumination system | $m$ |
| $\dot{m}$ | Mass flow rate | $\frac{kg}{s}$ |
| $Nu_H$ | Nusselt number based on height | — |

| | | |
|---|---|---|
| $p$ | Measured atmospheric pressure | $kPa$ |
| Pr | Prandtl number | — |
| $q$ | Heat flux | $\frac{W}{m^2}$ |
| $r$ | Relative humidity | % |
| R | Calculated result | — |
| $Ra_H$ | Rayleigh number based on height | — |
| $Re$ | Reynolds number | — |
| $T_{@exit}$ | Air temperature surrounding exit | $^oC$ |
| $T_{@inlet}$ | Air temperature surrounding inlet | $^oC$ |
| $T_{exit}$ | Mass flow averaged exit air temperature | $^oC$ |
| $T_{inlet}$ | Mass flow averaged inlet air temperature | $^oC$ |
| $T_w$ | Uniform temperature of wall | $^oC$ |
| $T_\infty$ | Temperature of fluid far from wall | $^oC$ |
| $u(\ )$ | Uncertainty in ( ) | — |
| $V$ | Velocity | $\frac{m}{s}$ |
| $\bar{V}$ | Area averaged velocity | $\frac{m}{s}$ |
| $W_n$ | $n^{th}$ variable | — |
| $\alpha$ | Thermal diffusivity | $\frac{m^2}{s}$ |

| | | |
|---|---|---|
| $\beta$ | Thermal expansion coefficient | $\frac{1}{^oC}$ |
| $\nu$ | Kinematic viscosity | $\frac{m^2}{s}$ |
| $\mu$ | Dynamic viscosity | $\frac{kg}{m\ s}$ |
| $\rho$ | Density | $\frac{kg}{m^3}$ |

# Chapter 1

# 1. Introduction

## 1.1 Background

One of the biggest problems our society will face in the coming years pertains to energy conservation and management. Our population is growing at an increasing rate while our planet's resources are slowly diminishing. This is creating an increase in demand for more efficient, clean and more sustainable methods of energy production, consumption and possible storage. In the past few decades we have witnessed an enormous interest in the impact of human activities on the environment. Despite the fact that fossil fuel use has an adverse effect on the environment, fossil fuels still contribute significantly towards energy production in developed countries. As per the Natural Resources Canada's Energy Use Data Handbook (2009), buildings are known to use more than 40% of primary energy used in North America. The need for Sustainable development has been on the increase in the recent past.

A large portion of energy is spent every year on space heating and cooling. In Canada, this is of great concern due to very harsh, varying climate which often reaches extremes from year to year. In Table 1-1 below, it can be seen that the most amount of energy used is for space heating. In Table 1-2, we can also see that most of this energy is being supplied by natural gases and other non-renewable resources. (Natural Resources Canada, 2009)

**Table 1-1 Total Energy Use in buildings (Natural Resources Canada, 2009)**

| Total Energy Use (%) | 1990 | 2005 | 2006 | 2007 | 2008 | 2009 |
|---|---|---|---|---|---|---|
| Space Heating | 61.8 | 61.3 | 60.3 | 62.8 | 63 | 62.8 |
| Water Heating | 19.1 | 18.1 | 18.8 | 17.9 | 17.5 | 17.3 |
| Appliances | 14.3 | 13.8 | 14.4 | 13.4 | 13.9 | 14.4 |
| Lighting | 4 | 4.4 | 4.5 | 4.1 | 4.2 | 4.3 |
| Space Cooling | 0.8 | 2.5 | 2 | 1.9 | 1.5 | 1.2 |

**Table 1-2 Total Energy Use in buildings (Natural Resources Canada, 2009)**

| Total Energy Use (%) | 1990 | 2005 | 2006 | 2007 | 2008 | 2009 |
|---|---|---|---|---|---|---|
| Electricity | 36.5 | 39 | 39.7 | 38.2 | 39.3 | 40.6 |
| Natural Gas | 41.2 | 46.3 | 46.3 | 47.4 | 47.2 | 46.4 |
| Heating Oil | 14.5 | 6.6 | 6.2 | 6.1 | 5.2 | 4.5 |
| Other | 1.7 | 1 | 1.1 | 1.1 | 1.2 | 1.1 |
| Wood | 6.1 | 7.1 | 6.8 | 7.1 | 7.1 | 7.5 |

In the 1970's and 80's, the aim of net zero energy buildings (NZEB) was taken into consideration earnestly due to the rise in oil prices. NZEB is the reduction of energy obtained from fossil fuels in building operations and maintenance. It can be accomplished by taking conservation measures or replacing fossil fuels with renewable energy sources incident on the building. With rising fossil fuel prices and the increasingly publicized connection between fossil fuel use and climatic changes, achieving NZEB has become a prominent goal in building design and is the long term goal of professional associations such as the American Society of Heating, Refrigeration and Air-Conditioning Engineers (ASHRAE) and LEED. Amongst renewable technologies utilized in the implementation of NZEB are wind turbines, geothermal heat pumps and more commonly passive and active solar technologies.

The goal of this project is to reduce the amount of non-renewable energy spent on space heating in buildings by utilizing naturally present solar energy. This has been done

successfully already in several different ways with main focus on residential building. This concept of solar energy use is known as passive solar heating. Active methods of utilizing solar energy incident on a building include photovoltaic electrical generation; pump driven solar hot water and hot air collection systems. Passive technologies include shading, natural day lighting, natural ventilation and air heating. Passive air heating is the main focus of this work.

It was highly desirable for passive technology to not only make use of solar radiation incident on a building to provide heating, but also to supply fresh air. This is imperative since humans release carbon dioxide when they breathe, thus increasing its concentration in the air. This led to the investigation of solar thermosiphons, which can provide heating and ventilation by using buoyancy to drive the airflow through them. The supply mode of Solar Air Flow Window (SAW) was chosen as the most effective method for research at first.

A Solar Airflow Window (SAW) is able to switch between the different modes, and is hence not restricted to operating in just one mode when constructed like current solar thermosiphons. The supply mode that can provide natural ventilation and at the same time warming up the air as it enters the building was the focus of the previous research. A SAW setup for supply mode can operate in exhaust mode, allowing warm air to exit the building in winter time; much like an open window would, increasing the heating load of the building. There are many causes of this backwards flow. External pressures on the SAW such as being on the leeward side when wind is blowing on a building, stack effect above the neutral pressure line in a building, and a mechanical ventilation system that is pressurizing the building will force air to exhaust out through SAWs when the desired is to supply hot air with them. Also when no radiation is incident SAW, such as

night time on the, the warm inside air that contacts the glass will cool and fall, resulting in exhaust by sucking air out of the building.

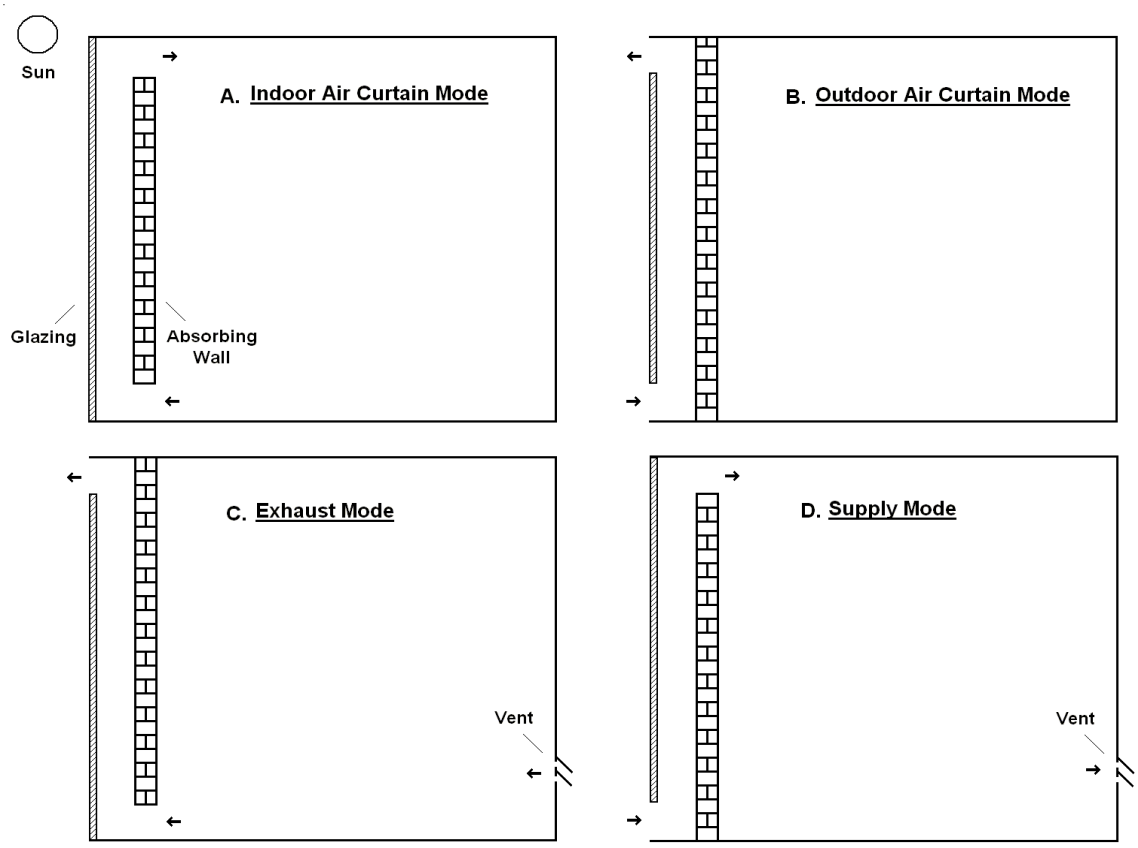


**Figure 1-1 Modes of SAW: A. Indoor Air Curtain, B. Outdoor Air Curtain, C. Exhaust, D. Supply**

There is a potential for overheating the occupants that are close the thermal envelope. So where and how the fresh supply air enters the building is of importance. Humidity being too low may also be a problem as cold air does not hold much moisture and when heated will be even less humid. Since this air is warmer, it will tend to rise and stratify on the ceiling, and typically be out of contact with the occupants. While rising and stratifying along the ceiling, this air will mix with the air in the room, cooling the supply air

from the SAW but raising the overall temperature of the room. So the degree of discomfort from overheating decreases the further the supply air enters into the building.

The case study for the optimal conditions showed that only 6% of the mass flow for ventilation could be met (Friedrich, 2011). Given the fact that not every day is always sunny, the ventilation potential of the decreases when averaged over a month. Just from the number of cloudy days in Ottawa, which only allow diffuse radiation to fall on the SAW, the monthly average of the mass flow ventilation load that could have came from the SAW in supply mode is 4%. Taking into account the practical requirements of a valve, a screen cover, and possibly a filter, the pressure drop will increase in the cavity, and we can expect the flow rate to decrease even more. Due to the low flow rates of a practically implemented SAW in supply mode in winter time, it is unlikely a SAW in supply mode would justify the energy saved in not mechanically pumping the ventilation air into the building compared to the extra energy needed due to losses of the SAW during non sunny periods, and certainly would not justify the extra costs of the control system.

## 1.2 Solar Thermal Buffer Zone

Due to the above results a new idea/method was chosen for research, Thermal Buffer Zone (TBZ). It is the Semi-conditioned space with temperature between inner fully conditioned space and outside. It is completely passive-Driven by Natural Convection. Designed to absorb solar radiation and distribute throughout the building, equalizing the temperature between North/South and Top/Bottom. The higher the temperature difference between South and North the higher will be the flow rate. Another benefit

compared to the Solar Air Flow window is that it allows day lighting and visibility. It can also store energy in thermal mass during day to keep building warm at night and also minimize the heat losses.

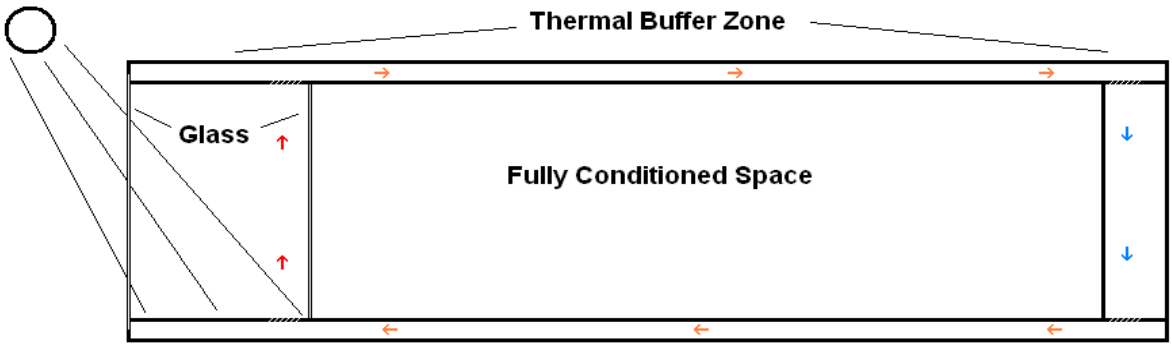


**Figure 1-2 Solar Thermal Buffer Zone**

Due to the orientation of the sun, a building receives an uneven amount of solar gain (solar radiation energy). The south facing side of a building receives more energy than the north facing side, which creates an uneven temperature distribution. This is undesirable as it can cause discomfort for building occupants as well as make it more difficult to control and maintain a set interior temperature. In the winter the temperature difference can create other issues; sometimes the north side of the building requires heating while the south side requires cooling. By better managing solar gain, we can eliminate these problems without having to spend energy on mechanically driven air conditioning or heating.

This can be done by creating a thermal buffer zone (TBZ) around the building. A TBZ consists of two layers of insulation separated by an air cavity. Due to the solar gain of the building, this air cavity is heated on one side while the other side remains cool.

This configuration will create a density difference between the two columns of air which will cause a flow around the building envelope. This is referred to as a thermally-induced, buoyancy-driven flow. The amount of solar gain can be manipulated by changing the conditions of the south facing side, such as the envelope size, materials used and geometries constructed.

The thermally-induced, buoyancy-driven flow will be the main focus of this project. A mathematical model was created by an undergraduate group to predict the conditions which must be met in order for this flow to occur, as well as how effective the design is at heating and stabilizing a structure's temperature. A scale model was designed and constructed to allow for physical experiments to be conducted.

TBZ allows solar gain from whole south side instead of just spandrel areas (**3 times** the potential just due to larger surface area). It is fully integrated with the building, and does not need to rely on the HVAC system for mixing like SAWs do. TBZ provides heating even when ventilation is not needed (unlike the supply mode or an active transpired system like SolarWall which always has to provide ventilation). Basically it is a better version of the indoor air curtain.

Given the time consuming nature of setting up and taking measurements with experiments, as well their variability in results, it is often much simpler to setup a numerical simulation. Changing parameters in numerical models are typically much easier to do than in experiments. This is why numerical models are often preferred to experiments. However, the drawback is that without some form of validation, their results cannot be trusted, as the assumptions made may not capture the phenomenon investigated properly.

There has been no research work done previously with a thermal Buffer Zone with a Convection Loop; Convection Loop being the main idea here. The ability to take the hot air from the south side to all around the building passively is the main idea of this research. (R. Richman, 2010)

Solar Thermal Buffer Zone (TBZ) is the new technology which has been selected for research that would help achieve net zero energy buildings. This is a passive method that provides a means of heated air by utilizing solar radiation. This technology will reduce the amount of conditioned air that needs to be provided by the mechanical ventilation system, reducing the consumption of non-renewable energy consumption such as natural gas and electricity just like Solar Air Flow Window. As mentioned previously, the main difference is that it is a closed system since it was recommended by building engineers at Halcrow Yolles. The air heated by solar radiation from the South side rises and the cold air from the North side falls, therefore creating a convection loop.

## 1.3 Buoyancy Effects

To understand solar thermosiphons, an understanding of the fundamental forces driving them is required. Less dense fluids have less gravitational force pulling them down, and will rise relative to denser fluids. The hydrostatic force acting on a fluid particle can be described by: *Eq. 1-1*

$$P = \rho g H$$

For solar thermosiphons, the force that drives the system can be found by comparing the hydrostatic force developed in the cavity to that developed outside of the cavity. *Eq. 1-2*

$$P = \Delta \rho g H$$

Gravity can be assumed to remain constant. This means that the driving force in a solar thermosiphon can be controlled by changing the density difference or the height of the cavity. Air follows the ideal gas law at atmospheric pressures and temperatures; hence the density of air can be reduced by increasing the temperature at the same pressure. The hotter the air becomes in the solar thermosiphon cavity relative to the outside, the larger the pressure force will be, to drive the flow through the cavity.

## 1.4 Pressure Drop Effects

As with any internal flow system there is resistance to flow due to friction. The losses from friction with fluid shearing past the cavity walls are typically minor losses in natural convection, as the velocities in the cavity are very small. However, what are known to be the minor losses, pressure drop caused by flow changing direction around bends, are larger losses in this natural convection case, as the number of bends is large relative to the total height of the cavity. Increasing the spacing between parallel plates, B, increases the cross sectional area. The average velocity decreases as the cross sectional area increases. Typically, the decrease in average velocity reduces the pressure drop. Hence, the increase in cross sectional area is typically more than the reduction in average velocity and the flow rate increases with a larger B spacing. However, once certain B spacing is reached for a given driving hydrostatic pressure, circulation within the cavity becomes larger resulting in more pressure drop. Bigger than this B value the mass flow rate will decrease for a given driving hydrostatic pressure due to the increase in pressure drop. So the optimal B spacing for mass flow rate is defined by the pressure losses that give the lowest pressure drop for the given hydrostatic

pressure. For a given driving hydrostatic pressure B would need to be optimized to get the highest mass flow rate through the cavity.

## 1.5 Radiation and Optical Properties

Since the system is driven by solar radiation, in order to have a better understanding of radiation, radiation heat transfer will be discussed. When solar radiation strikes the outside surface of the glazing, it can be reflected, transmitted or absorbed on the surface. The relative amounts of this depend on the material properties, incident angle, and the wave length of the source radiation. The solar radiation that is reflected off the outside surface is the first source of loss in the system. The radiation that gets absorbed at the outside surface, acts as heat source at the surface, heating the glass, from here the heat can travel by conduction through the glass to the inside, or be lost by convection to the outside air or by infrared radiation to the outside surroundings. A distinction needs to be made between the solar radiation that has a much shorter wave length, and the thermal radiation emitted by a surface at a much lower temperature with long wave lengths in the infrared spectrum, as optical properties can and do change for different wave lengths. Some of the solar radiation that is being transmitted through the glass is absorbed while passing through it. For constant material properties this is typically a liner decrease in the transmitted radiation with the thickness of glass. This solar radiation that gets absorbed while being transmitted acts as volumetric heating in the glass. Again this heat can be conducted through the glass to the inside or outside; the later results in losses. Once the transmitted solar radiation has made its first pass through the glass, it strikes the second glass surface, the inside of the pane of glass. Here again it can be reflected, transmitted or absorbed on the inner surface. That which

is reflected is sent back through the outside pane, part of it being absorbed as it goes into the inside ambient, once again acting as volume heating of the glass. Upon striking the second glass, the same three options are available, that which is transmitted is acts as volumetric heating, and that which is reflected in sent back into the first glass. It can quickly be seen that the radiation can be reflected between surfaces indefinitely. However, each pass through the glass results in some being absorbed, and not all is reflected back at the surfaces, and after a few passes back and forth the original radiation becomes dissipated till it is insignificant. The solar radiation from the first incidence on the inside surface that was absorbed as heat, can be transferred to the inside of the cavity by convection and infrared radiation, or travel by conduction through the glass to be lost to the outside. The solar radiation that is transmitted through the inside surface of the glass can travel uninhibited, as air does not measurably absorb or scatter solar radiation in the small gap, to the second glass. The solar radiation energy that is absorbed in the second glass surface, becomes a surface heat flux, and can either be conducted away from the surface, typically into the building, transmitted as infrared radiation to the glass plane, again not necessarily lost, or be transferred by convection to the air in the cavity which is the desired form of the energy.

As demonstrated above, the solar radiation conversion to thermal energy in the form of warm air is quite complex in a single glazed solar thermosiphon. The perpetual reflections for different wave lengths make it quite tedious to find the total radiation transmitted through the glass. However, by use of geometric series and adding the effect of all the systems together the total system transmission and absorption coefficients can be found as derived in Duffie and Beckman (1974). The product of these two terms, which make up the optical efficiency, multiplied by the incident solar radiation on the

outside of the glass, will give the total solar radiation that gets converted into heat at the second glass. Changing the glass optical properties will change the system coefficients. To improve the optical efficiency, it is better to have glass that is less reflective, more transmittance, with a low surface and volumetric absorption, and to have a high absorbing surface absorptivity. The optical efficiency results in losses that are typically larger than the losses from convection and infrared radiation off the outside of the glass. For an industry standard single 6 mm thick pane of clear float glass the system transmittance is around 0.83. Coupled with second glass with absorptivity 0.54, the optical efficiency of the system is 69%, meaning a third of the incoming energy is lost due to optical properties. Switching to a double pane insulating glazing unit drastically reduces the conduction losses through the glazing by the addition of the air gap between the panes. However, the additional pane also adds extra reflection surfaces and glass to absorb solar radiation, reducing the system transmittance to typically 0.60. So the question becomes, does the reduction in conduction losses through the glass make up for the reduction in optical efficiency for double pane windows? Given that conduction losses are temperature differential driven and optical properties are not, only in cases where there is extreme difference between inside and outside temperatures, would the savings from reduced conduction losses overcome the reduction in optical efficiency of a double pane window.

Not only do windows optical properties depend on wave length of the incoming radiation but also on the incident angle. If not specifically mentioned the values given assume the optical properties of glass when the radiation is perpendicular to the surface, or $90^0$. The reflectivity and transmittance of glass do not change from the perpendicular value much until values greater than $50^0$ from perpendicular; however they change

drastically after this point, with the glass becoming perfectly reflective at $90^0$ from perpendicular, or when parallel to the surface. For the low attitude of the sun during the winter, south facing vertical surfaces would have incident angles less than $50^0$. Hence, it would only be in the summer time that the incident angle may become large enough to reduce the radiation entering the system.

Now that the optical properties have been discussed for the solar radiation wavelengths, the infrared radiation losses from the heated surfaces should be analysed. Every surface emits radiation depending on temperature it is at and the emissivity. The surface temperature determines the wave length and the intensity, the emissivity determines the intensity relative to a black body surface. If the surface is surrounded by other surfaces at the same temperature, the amount of radiation emitted to the other surfaces will equal what is received from them and there will be no net transfer of heat. However, if the temperature is greater than the other surfaces, heat will be transferred from the warm surface to the cooler surfaces based on the absolute temperature to the fourth power difference. For the low absolute temperatures, and small temperature differentials, this heat transfer is very small compared to forced convection cases, and typically negligible. Natural convection heat transfer is also very small compared to forced convection, and since natural convection is the only form of convection in the thermal buffer zone, neglecting wind on the outer surface, infrared radiation heat transfer is no longer negligible. In fact with low enough natural convection, radiation losses may be larger than natural convection. This is especially important when looking at the heat transfer from the warm inside glass to what can be the cold glass surface. The air right next to the inner glass is warm from being heated at the lower sections, so the temperature differential between the air and the inner glass may not be as large as the

temperature differential driving radiation exchange between the two glasses. The same can also be said for the outer glass surface. Here the surface temperature of the ground and the sky can be colder than the air temperature that is in contact with the outside of the glass. The clear sky is cooler than a cloudy sky because it does not emit radiation back. However, this infrared radiation is at a different wave length then the solar, so there can different optical properties for this radiation. Probably the most significant is the fact that glass is opaque to infrared radiation. This means that no infrared radiation is transmitted through it. At the surface of the glass either the infrared radiation is reflected or is to be absorbed. Uncoated glass has high absorptivity in the infrared spectrum. So all losses below the solar spectrum from the inside of the cavity must be conducted through the glass, and cannot be transmitted and lost.

The difference in optical properties based on wave length can be taken advantage of by spectrally selective materials, simply meaning they have different optical properties at different wave length source radiation. Low emissivity coatings on windows are an example of these. The low emissivity coating allows solar radiation, which is at a much shorter wave length, to pass right through it, there by not affecting the solar optical properties of the glass. At the infrared wave length the coating is very reflective, and not very absorptive. As fundamentally proven in radiation heat transfer the absorptivity at a given wave length is also equal to the emissivity if the surface was to emit at that wavelength. So the low emissivity coating changes the infrared emissivity of glass, which is the wave length it would emit around room temperature, from being high to being low. So this coating will reduce the radiation heat loss off a surface that is near room temperature compared to uncoated glass. So this allows for the higher optical efficiency

of glass in the solar spectrum to be maintained while reducing the infrared losses through the glass.

Not to be forgotten in the heat transfer analysis is the energy absorbed on surface of the glass and also throughout the volume. As with the inner glass surface if the inside surface of the glass is warmer than the air going passed it, it will warm the air and contribute to the useful output energy. Of course the temperature of the glass depends on the convection and radiation heat transfer on both sides of the glass, the conduction through it, and the volumetric heating. The colder the outside air temperature gets compared to the inside, the more energy will be conducted through the glass to the outside surroundings. With a cold enough surroundings, all the energy absorbed in the glass will be conducted to the outside, and the glass inside temperature will become below the temperature of the air on the inside of the cavity. Outside temperatures below this will remove useful energy from the hot air in the cavity. However, the energy absorbed in the glass is not completely lost as it does heat the glass to a higher temperature than the glass would be without the heating being there, thereby reducing the temperature differential between the glass and the inside cavity, reducing the losses out of the inside. So heating of the glass is better than the energy being reflected out of the system.

## 1.6 Dimensionless Analysis

To non-dimensionalize the setup and allow for scalability, dimensionless groups are applied to physical problems. For solar thermosiphons such as thermal buffer zone, the ratio of buoyant forces to momentum and thermal diffusivity is important and can be characterised by the Rayleigh number. The Rayleigh Number is found by multiplying the

Grashof number and the Prandtl number. The Grashof number is the ratio of buoyancy forces to forces of viscosity. The Prandtl number is the ratio between momentum diffusivity and thermal diffusivity. In natural convection situations, an important dimensionless group is the Grashof number. To provide some physical significance to this group prior to defining it, we use a simple order of magnitude estimate of the natural convection velocity in the above examples. When fluid with a density ρ moves at a velocity V, the kinetic energy per unit volume can be written as ½ $\rho V^2$. This must come from some other form of energy, namely, potential energy lost by the fluid.

Over a vertical distance L, the difference in potential energy between the less dense fluid in the boundary layer and the more dense fluid outside it can be approximately expressed as g L $\Delta\rho$, where g is the magnitude of the acceleration due to gravity, and $\Delta\rho$ is a characteristic density difference between the boundary layer fluid and that far away. We can equate these two order of magnitude estimates, and neglect the factor of 1/ 2, because this is only an order of magnitude analysis.

There are two forms on the Grashof number; one for constant temperature walls, the other is called the modified Grashof number for constant heat flux applied to walls.

$$Ra_H = \Pr Gr_H \qquad \textit{Eq. 1-3}$$

$$\Pr = \frac{\nu}{\alpha} = \frac{C_p \mu}{\kappa} \qquad \textit{Eq. 1-4}$$

$$Gr_H = \frac{g\beta(T_W - T_\infty)H^3}{\nu^2},\ Gr_H = \frac{g\beta q H^4}{\nu^2 \kappa} \qquad \textit{Eq. 1-5}$$

A Rayleigh scaling analysis was done in order to verify the validity of experimental results as well as the feasibility of predicting the operation of a full size build compared to a lab apparatus. As shown in Table 3 we are able to see that at 22 $^{o}$C the experimental results would only hold valid for aspect ratios as high as 0.4 which justifies the gap width chosen to be investigated.

**Table 1-3 Rayleigh Scaling (22 $^{o}$C Ambient)**

| B | Ra(d) | | d | Ra(d) | | Model | Real |
|---|---|---|---|---|---|---|---|
| 0.1 | 6.5E+05 | | 0.3 | 1.8E+07 | | T1 | T2 |
| 0.2 | 5.2E+06 | | 0.6 | 1.4E+08 | | T2 | T2 |
| 0.3 | 1.8E+07 | | 0.9 | 4.8E+08 | | T2 | T2 |
| 0.4 | 4.2E+07 | | 1.2 | 1.1E+09 | | T2 | T2 |
| 0.5 | 8.2E+07 | | 1.5 | 2.2E+09 | | T2 | TU |
| 0.6 | 1.4E+08 | | 1.8 | 3.8E+09 | | T2 | TU |
| 0.7 | 2.2E+08 | | 2.1 | 6.0E+09 | | T2 | TU |

One of the uses of the Rayleigh number is it allows the prediction of when the flow will change from laminar to turbulent. However, the Rayleigh number is very specific to the geometry case considered and the flow pattern and correlations used for a single flat plate for a given Rayleigh number, will not be the same as the flow pattern in a parallel plate cavity. Also an asymmetric heated parallel plate cavity will not give the same flow pattern as a symmetric heated parallel plate cavity with the same Rayleigh number. So comparisons across different boundary conditions are not straight forward, and one cannot simply rely on the absolute value of the Rayleigh number alone to indicate the flow pattern.

## 1.7 Design and Construction

### *1.7.1. Size and Scaling*

The physical prototype needed to be scaled appropriately in order to properly simulate how a thermal buffer zone would work in a building. The original design was to create a one meter cube inner box with a uniform gap size around it, keeping in mind that the inside cube is open to ambient for measurement purposes. However, in order to better simulate a building the final prototype was extended in length so it would be

longer than it is taller. This is more similar to a building story, which is always rectangular. Due to the constraints of the lab space available and ease of construction, a scaling ratio of 0.3 was used for the final prototype.

The average height of an entire floor in a building is approximately 3.6 meters and has gaps below the floor and above the ceiling (between each floor) of approximately 0.3 meters. This means in order to maintain this relationship our prototype would be 1.2 meters in height and have upper and lower gap sizes of 0.1 meters. However, the overall height of the design had to be changed. It was extended to approximately 1.3 meters in order to accommodate the supports for the inner box.

It was originally desired to have the ability to change the upper and lower gap sizes so the gap could be kept uniform around the inner box. Due to testing much larger gap sizes with the new design, this feature was omitted. Instead, it was decided to use constant upper and lower gap sizes of 0.1 meters and to solely look at the effect of changing south gap size. These gap sizes can vary between 0.1 to 0.7 meters from the inner glass to the outer glass. This means we can adjust the dimensionless aspect ratio — the ratio of the gap width to the inner wall height — from approximately 10% to 70%. The general dimensions for the constructed prototype can be seen in the figure below.

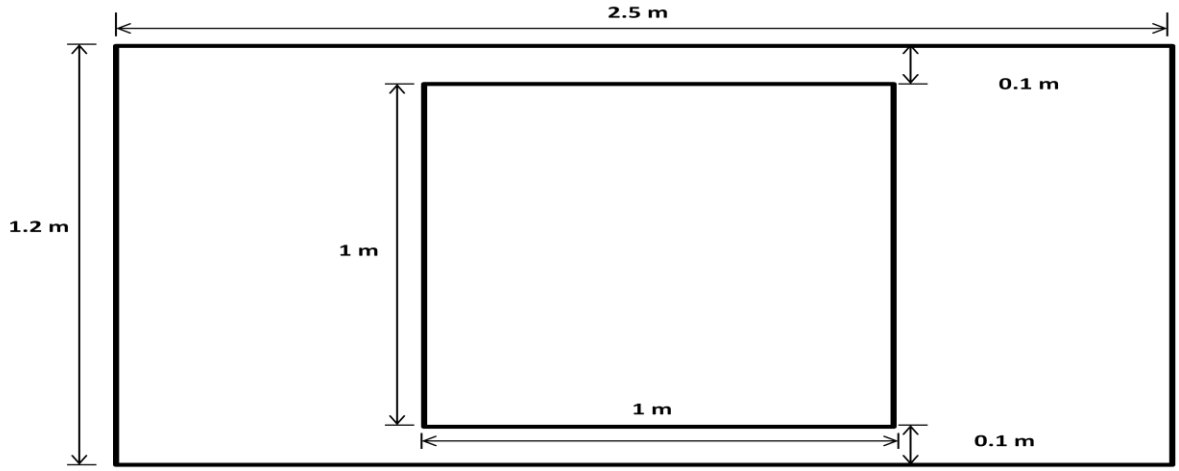


**Figure 1-3 General Dimensions for Physical Prototype**

Some other dimensionless values that could indicate system performance are the aspect ratios. The spacing between the parallel plates to total height, B/H, is an example of influential aspect ratio. The Grashof number comparing the buoyant forces due to the difference in temperature of the air that enters the inlet and the air that the flow exits into, and the viscous forces would represent a parameter that has a large impact on the system.

*Eq. 1-6*

$$Gr_A = \frac{g\beta(T_{@inlet} - T_{@exit})H^3}{\nu^2}$$

Nusselt number was the main focus of the previous researchers that worked on solar thermosiphons, which is the ratio of convective heat transfer to conductive heat transfer. This is not discussed in the current work because it does not affect the performance metric for solar thermosiphons.

$$Nu_H = \frac{hH}{k}$$ *Eq. 1-7*

## 1.8 Literature Review

A solar thermosiphon is a differentially heated open cavity. Therefore, research related to predicting performance of solar thermosiphons can be traced back to work of natural convection over a single heated vertical plate and flow between a differentially heated parallel plate open cavities. The air flow in solar chimneys, Trombe wall, and airflow windows, has often been treated as separate subjects. However, the basic assumption of modelling them as flow between parallel plates is universal in all the research done on these methods. This discussion will treat all three methods of buoyancy induced flow under the same heading as flow between heated vertical parallel plates. Experimental and numerical modelling of the heated vertical parallel plate channel has been done extensively and the flow within the channel is well understood (Gan 2006).

## 1.9 Previous Studies Related to Thermal Buffer Zone

There has been no research work done previously with a thermal Buffer Zone with a Convection Loop, the main idea here is the Convection Loop. The ability to take the hot air from the south side to all around the building passively. (R. Richman, 2010)

Solar Thermal Buffer Zone (TBZ) is the new technology which is selected for research that would help achieve net zero energy buildings. This is a passive method that provides a means of heated air by utilizing solar radiation. This technology will reduce the amount of conditioned air that needs to be provided by the mechanical ventilation system, reducing the consumption of non-renewable energy consumption such as natural gas and electricity just like Solar Air Flow Window. The main difference is, as mentioned previously it is a closed system as it was recommended by building

engineers at Halcrow Yolles. The heated air due to solar radiation from the South side rises and since the air on the north side of the building being cold will fall therefore creating a convection loop.

Some of the previous work done which is closest to the proposed area of research is Solar Dynamic Buffer Zone (SDBZ) (Richman R. C., 2009), a curtain wall system which “works by ventilating a cavity within a wall with heated exterior air to control moisture migration across the assembly”. SDBZ is also employed with in the spandrel area just like the Solar Air Flow Window. In the heating season from October 1$^{st}$ to March 31$^{st}$, the average overall seasonal efficiency based on the model was found to be 35%. (Richman R. C., 2009). “The experimental results show the SDBZ curtain wall to be an effective means of collecting solar energy in a relatively passive manner ... with experimental efficiency of 25 – 30% on average”. “The practical restraints of incorporating such a system into a building’s air handling system is required” (R.C. Richman, 2009), Just like the SAW duct work is needed in order for the preheated air to be supplied to the inside.

Another research that is similar to a thermal buffer zone is the concept of double facades in a building. “Double Skin façade is a special type of envelope, where a second skin, usually transparent glazing, is placed in front of the regular building façade. The air space in between called the channel is ventilated (naturally or mechanically) in order to diminish overheating problems in summer and to contribute to energy saving in winter.” (M.A. Shameri, 2011). It has been installed and monitored for at least 1 year at the Siemens building in Dortmund, Victoria. The research was carried out at the University of Dortmund. “The solar gains of the permanently ventilate facade saved approximately 15-18% of heating energy in winter.” (Pasquay, 2004). The average temperature in the

façade rises from 10 to 15 degrees compared to the outside in this system. One of the drawbacks in the system is that “the wind speed and wind direction must have a significant influence on the ventilation of the façade gap.” (Pasquay, 2004)

### *1.9.1. Double Skin Façade (DSF):*

According to (DeHerde, 2004), “a second skin façade is an additional building envelope installed over the existing façade.” This additional façade is mainly transparent. The new space between the second skin and the original façade is a buffer zone that serves to insulate the building. This buffer space may also be heated by solar radiation, depending on the orientation of the façade. For south oriented systems, this solar heated air is used for heating purposes in the winter.

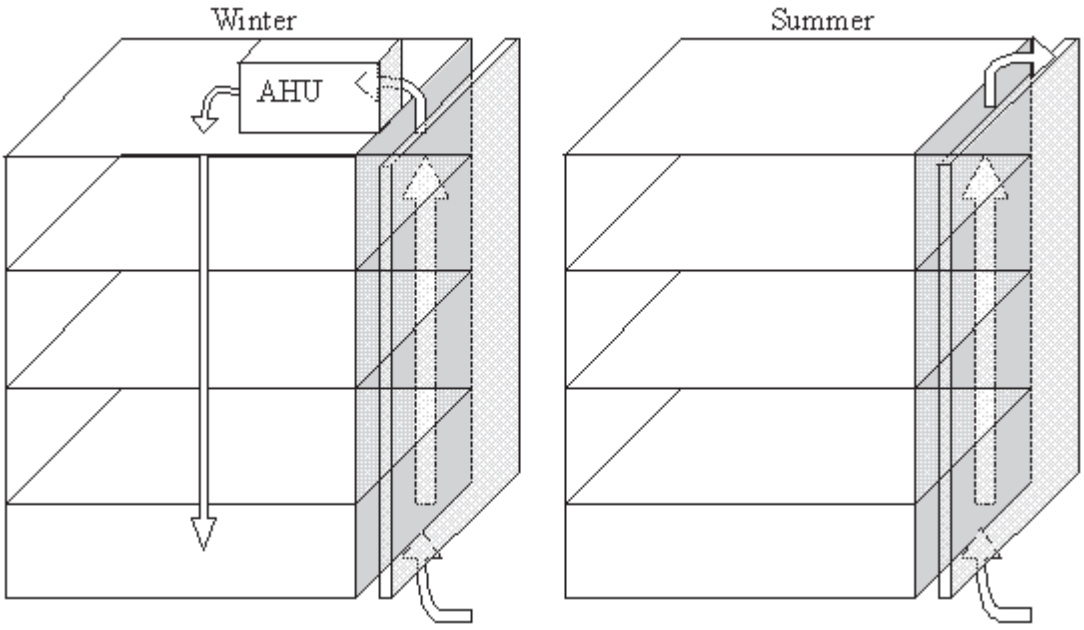


**Figure 1-4 Double Skin Façade Design for different seasons (Porazis, 2004)**

(Saelens, 2002) explains in his Ph.D. thesis the concept of the Double Skin Façade. According to him, “a multiple-skin facade is an envelope construction, which

consists of two transparent surfaces separated by a cavity, which is used as an air channel". Naturally Ventilated Wall: "An extra skin is added to the outside of the building envelope. In periods with no solar radiation, the extra skin provides additional thermal insulation. In periods with solar irradiation, the skin is naturally ventilated from/to the outside by buoyancy (stack) effects - i.e. the air in the cavity rises when heated by the sun (the solar radiation must be absorbed by blinds in the cavity). Solar heat gains are reduced as the warm air is expelled to the outside. The temperature difference between the outside air and the heated air in the cavity must be significant for the system to work. Thus, this type of façade cannot be recommended for hot climates".

In most of the literature, one can read that the most common pane types used for Double Skin Facades are:

• For the internal skin (façade): Usually, it consists of a thermal insulating double or triple pane. The panes are usually toughened or unhardened float glass. The gaps between the panes are filled with air, argon or krypton.

• For the external skin (façade): Usually it is a toughened (tempered) single pane. Sometimes it can be a laminated glass instead.

(Lee, 2002), claims that the most common exterior layer is a heat strengthened safety glass or laminated safety glass. The second interior façade layer consists of fixed or operable, double or single-pane, casement or hopper windows. Low-emittance coatings on the interior glass façade reduce radiative heat gains to the interior.

The CFD modeling of passive solar space heating is not an easy matter. Jaroš, Charvát, Švorèík and Gorný, presented a paper in the Sustainable and Solar Energy Conference in 2001, which deals with critical aspects of these problems, touches

possibilities and drawbacks of some CFD codes in this area and, on basis of several solved cases, presents outcomes which can be obtained by this method. (Jaroš, 2001)

According to the authors mentioned previously “simulation methods are a very useful tool for the optimization of the solar building performance, since they enable to predict performance parameters still in the stage of the design. The CFD simulation has become very popular, because of its capability to model particular details of the temperature fields and airflow patterns. These features are essential just in the case of solar-heated rooms with the intense heat fluxes and natural convection. The CFD simulation of the performance of solar air systems can significantly improve their operation parameters and effectiveness. Moreover, new structures or systems can be evaluated still in the stage of their design. However, the applicability of the CFD simulation is still restricted to the relatively simple cases. The simulation of airflow and heat transfer inside the whole building is still difficult due to the computer performance. The capabilities of CFD simulation will grow with the increasing capabilities of hardware and software”.

### *1.9.2. Depth of DSF:*

The range of cavity varies significantly. In existing buildings, the range tends to be between 200mm and 1400mm as measured face to face between the inner and outer skins. There are three predominant styles: the compact style is usually from 200mm to 500mm, the latter allowing enough space to allow for maintenance occupation of the cavity primarily to accommodate cleaning of the surfaces within the cavity. The wide style is typically about

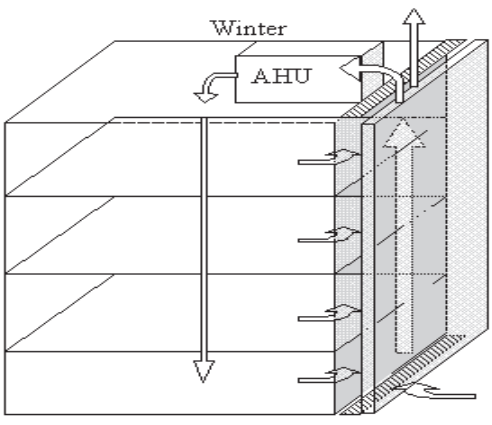

1m wide. Additional installed costs for the DSF above typical static façade system have ranged significantly from 20% to perhaps 300% (Arons, 2000).

**Figure 1-5 Double Skin Façade Design for winter (Porazis, 2004)**

During the heating season some direct radiation will be desirable. It is easy to overheat the area adjacent to the window. Therefore control of the position and deployment of the shading device is desirable. The solar factor SF can be adjusted by adjusting the blinds. The U-values will be improved if the blinds absorb some heat, thereby increasing the cavity temperature and reducing the difference in temperature between the cavity and interior.

### *1.9.3. Occupant productivity and contact with the environment:*

It has been estimated that wages and salaries can represent about 90% of all costs of a typical office building (Ternoey, 1985). Certainly, in the commercial market energy efficiency is probably only one tenth the cost of personnel. For this reason, owners will be driven towards solution that increase their return on investments made in people before those that are made in infrastructure, but the two of them are linked.

Reduced sickness, absenteeism coupled with increased performance would more than offset any increased initial cost of life cycle costs [Robbins, 1986] associated with providing more workers visual access to windows [Franta and Anstead 2000].

If a more comfortable, controllable and visually pleasing environment can be created then workers may well be more productive.

## 1.10 Objectives of Present Research

Based on the knowledge gaps identified in the prior literature review of solar thermosiphons, the following are the objectives of the current work:

1) Carry out experiments to check the working and effectiveness of the TBZ

2) Develop a numerical model to include real world parameters not considered before, such as conduction through the glazing surface.

3) Use the developed numerical model results for the flow patterns in the experiments

4) Draw conclusions from the results about the effectiveness of the use of the Thermal Buffer Zone

# Chapter 2

# 2. Experimental Work

## 2.1 Experimental Setup

To accomplish the goal of creating an experimental apparatus that is representative of the real world building, an experimental setup was constructed that can be seen in figure 2-1 below. The configuration of the solar thermal buffer zone and radiation was used as the heat source, features only implemented before by a previous graduate student for Solar Air Flow Window. The apparatus also allowed for variation of parameters that previous researchers found to have an effect on the performance of solar thermosiphons. Two parameters that can be varied include the parallel plate spacing gap ratio, B/H and the radiation intensity. For this experiment only parameter gap ratio was changed. The optical properties of the system can be changed by changing the type of glass.

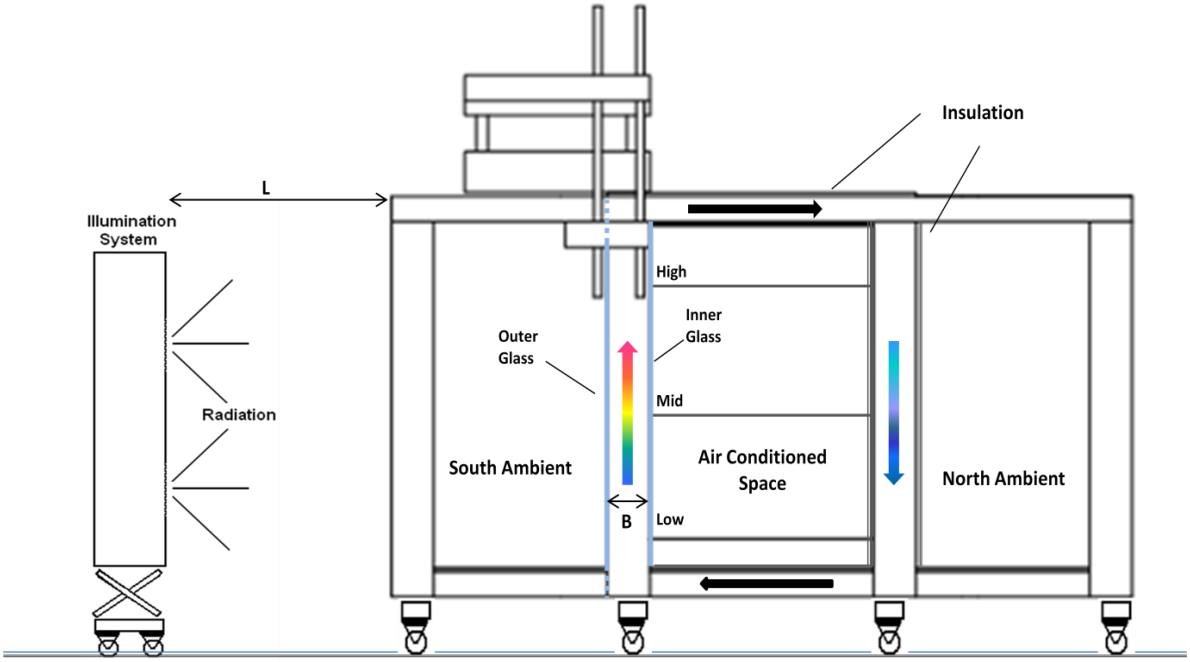


**Figure 2-1 Experimental Setup**

The heat flux can be varied for this setup as is the case in a real application due to the varying radiation intensity throughout the day. The heat flux in the current set up can be varied by varying the distance between the cavity and the radiation source. One heat flux level was selected for the current work to model the thermal buffer zone in winter in a Canadian climate. This was accomplished by considering a south facing window in Ottawa, Canada, in January. The heat flux considered was the average heat flux over the daylight hours, on a perfectly clear day. The value was roughly 380 W/m$^2$, and was calculated based on standard solar resource calculations as seen in Duffie and Beckman (1974).

## 2.2 Structural Frame

A custom structural frame made of softwood lumber was used to hold the various components in place to replicate a solar thermal buffer zone. A one and half inch thick Expanded Polystyrene board, R-7.75, with reflective radiant barrier facing the outside of the setup was used as insulation to reduce heat losses from the surfaces exposed to the ambient.

### *2.2.1. Frame and Enclosure*

The prototype was designed as per the dimensions in Figure 2-1. The experimental set up was designed to consist of 4 vertical glass surfaces. It was decided for the current investigation, only south side to consist of glass surfaces, to investigate the optimum gap width on one side only. A frame made of softwood lumber had to be created to support the additional weight and all of the external walls. This would provide enough support to house the glass, as well as mount all of the pieces required to make an enclosure. The entire structural frame was also mounted on castors to facilitate moving it around the lab. The centre cube is open on both sides and therefore at the same temperature as the lab.

The frame was lined with a combination of Plexiglas, plywood and corrugated sheet plastic. Plywood was used as the base to make construction easier, as well as to support some of the weight. Transparent Plexiglas was utilized for one side of the frame so that the velocity probe is visible during taking measurements, preventing the fragile tip from touching any surfaces. The remaining surfaces of the frame were made of white corrugated plastic sheets,

since it is lighter, considerably less expensive and is easier to work with as opposed to plywood and Plexiglas. The materials Plexiglas and plastic sheets were also used because of their pliable nature, making it easier to manipulate for fitting them into position. To join and seal the pieces together, transparent silicon caulking and masking tape were used.

## 2.3 Window Frame

One of the major challenges while designing was to create a way to vary the gap size on the south side of the wall. Since the outer pane of glass on the south side is large, heavy and fragile, it has to be moved in a quick, easy and safe way. Also to reduce the size and weight of the window frame compared to commercial ones, a custom frame had to be made. This was done by hanging the glass from another softwood constructed frame, which was suspended above the original one by four threaded steel rods. A lightweight aluminum structure for the glass was designed and machined to house the glass and suspend it from the frame. Drawings of the frame can be seen in Appendix D in Figures 8-8 and 8-9.

### *2.3.1. Glass*

In order to better collect the incident solar radiation from the heat source, it was necessary for the glass used in the physical prototype to have specific properties. Hence, a standard 6 mm thickness, which is a typical size for windows' glass in buildings, was used for both panes. For the start of the project, only two panes of glass; the outer and inner panes on the south side were purchased and mounted in the frame. Corrugated sheet plastic was used for the

north side surfaces instead of glass. The apparatus would first be tested with only two glass panes, before moving to four of them. The outer glass was selected as standard clear window glass. This has a high solar heat gain coefficient of 0.83 which describes the amount of solar radiation energy which is allowed to pass through the window and enter the thermal buffer zone. A Solarshield Grey glass was used for the inner glass surface. It is tinted, has higher absorption and lower transmittance properties which leads to a lower solar heat gain coefficient of 0.54. This means that less solar energy will be transferred through the glass, directly into the room. The energy will instead be transferred to the air in the fluid cavity. Holes were drilled through the inner glass to insert the velocity probe into the air gap.

## 2.4 Instrumentation and Key Components

### 1.4.1 Illumination System

2 The desired radiation source would have the same intensity for every wavelength as that of the sun light that passes through the earth's atmosphere. This requires a black body source at the same temperature as the sun surface (5777 $^{o}$K) that has the radiation pass through a 1.5 air mass filter, which is the standard filter to remove the intensities of the wavelengths that the earth's atmosphere absorbs or reflects. However, getting a radiation source with the exact same light spectrum as the sun was not practical. A custom made illumination system, purchased for the SAW research project, was used as it was the most economical way of simulating the sun radiations. The illumination system could provide over a meter square area, an average of 1000 W/m$^2$. The light bulbs that were used were the Quarts

Tungsten Halogen (QTH) light bulbs and they have black body spectral properties of 3000 $^{o}$K to 3300 $^{o}$K.

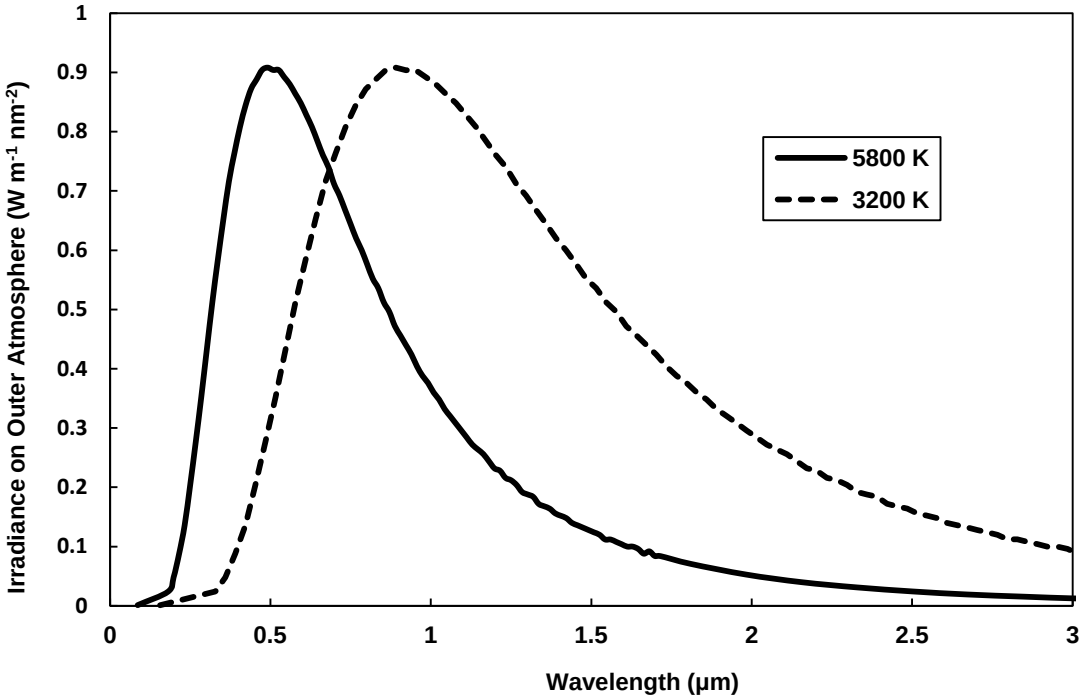


**Figure 2-2: Spectral Distribution of Solar and Black Body Temperature of 3200 $^{o}$K**

As seen in the Figure 2-2, the QTH light bulbs have a black body spectrum that has less intensity in the visible spectrum than in the solar radiation. For the purpose of the current experiment, radiation energy is converted into thermal energy. If material properties are uniform across all wavelengths and the total amount of energy from the light source is the same as would be from the sun, the source radiation intensity with wavelength should not be a concern. However, real surfaces do have optical properties that change with wavelength. For this experiment, the two surfaces of importance are the glasses on the south side. The optical properties of glass are more sensitive to the radiation spectrum, particularly the fact that glass is opaque to long wavelength radiation, and has high

transmittances to short wavelength radiation. The spectrum of a black body source at 3200 $^{o}$K has most of its energy in wavelengths that glass transmits at. Hence, the QTH light bulbs, although a different spectrum, will give close thermal results.

**The four QTH light bulbs acted as point sources with light diverging from them and them and this resulted in the non-uniform heating pattern seen in F**

Figure 2-3. There are hot spots directly in front of the light bulbs and the intensity decreases with radial distance from these hot spots. The intensity from the bulbs overlaps in the center of the illuminated area, causing a higher heat flux in the center of the cavity relative to the sides and the top and bottom. The non-uniform heating pattern results in a non-uniform flow, as the center receives more energy and reaches higher temperatures on the second glass, inducing more flow in the center of the cavity relative to the sides.

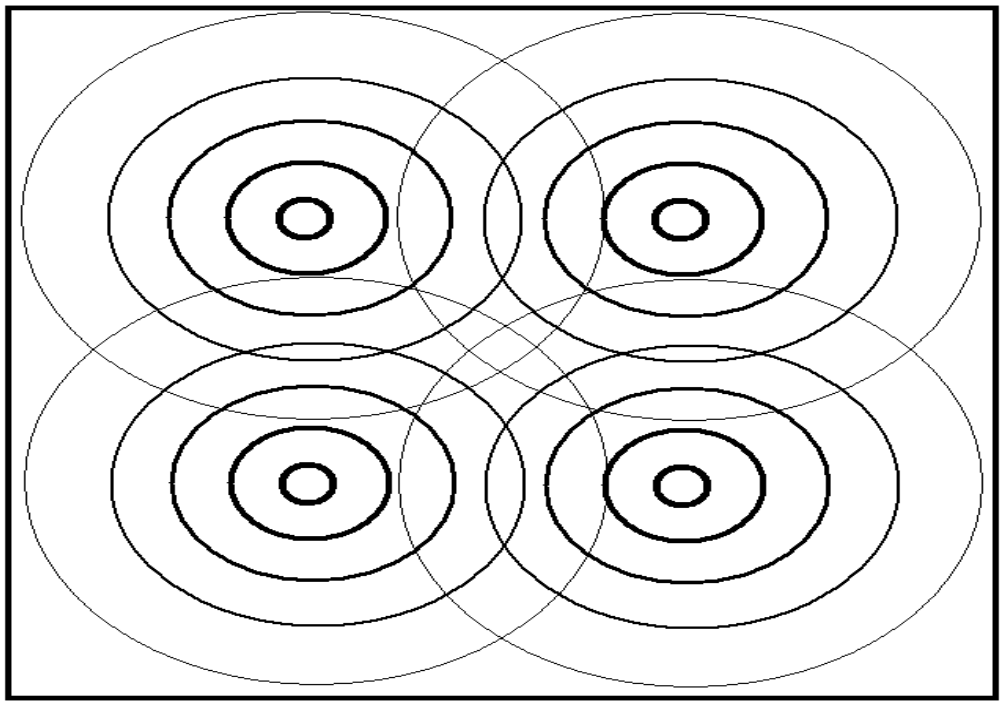

**Figure 2-3: Overlapping heat flux intensities on the illuminated surface from the heat source**

## 2.5 Pyranometer

Along with a radiation source comes the need to measure the intensity from the source. A solar pyranometer which was already available was selected as the measurement device mainly due to its ease of use and applicability to the experiment. A Hukseflux LP02, ISO second class, was the unit used, which was bought for previous research. It is not as accurate as the first class, but it provides the same functionality. The unit's accurate operational range is 305-2800 nm, which contains the majority of the energy for the solar spectrum. A two dimensional square grid with 9 cm spacing between the pyranometer

measurement locations was used to find the heat flux intensity over the illuminated south surface.

## 2.6 Data Acquisition System

Voltage readings from the pyranometer, thermocouple and velocity probe were gathered with a Hydra Data Logger Series II. Interchangeable input cards that had 20 channels were used to allow for easy switching between different measurement components, rather than rewiring them every time. There were over 50 thermocouples, and it was not possible to get reading of all at the same instant. Steady state experiments were conducted so that temperatures and velocities gathered at different times could be assumed to be constant over the test. Steady state was considered achieved when the temperature measurements in the cavity did not change by 0.5 $^{o}$C during a 15 minutes period. After the air temperature measurements were taken, the temperature in the cavity was checked again and in most cases the temperature had gone up less than 1 $^{o}$C from when steady state was assumed to be reached. The temperature increases greater than this were associated with the ambient room temperature increasing from the start of steady state.

## 2.7 Temperature Measurements

The different locations in the thermal buffer zone where the air temperature was measured can be seen in figure 2-4. Also, in order to be able to compare it with the numerical model, temperature profiles on the center line of the vertical surfaces were collected. Thermocouples were selected as the measurement method due to economy and flexibility. Type T thermocouples

were selected as they have the lowest measurement uncertainty. The thermocouples used were custom made by welding the 0.5 mm diameter wire together, resulting in diameters of 2 mm at the junction.

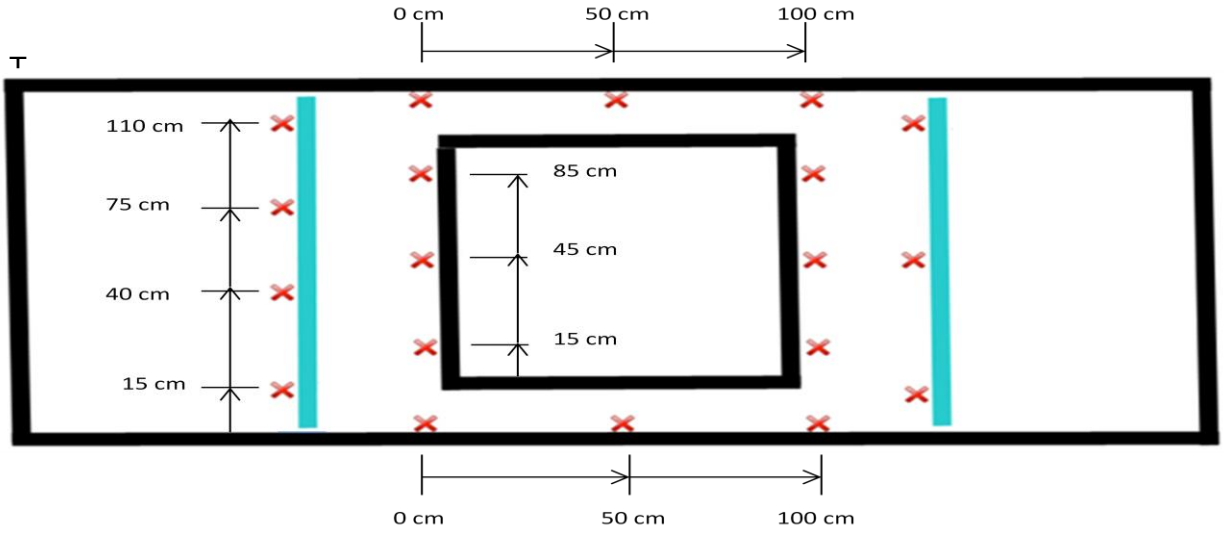


**Figure 2-4: Thermocouples placement for temperature measurement in the Experimental Setup**

To measure the temperatures on the surfaces, thermocouples were attached with clear tape. In order to shade them from the solar radiation, tiny strips of tin foil were placed in front of them. The room air temperature was measured by means of 5 thermocouples, with paper tube covers placed around them to avoid the air current from blowing directly on them, but at the same time, air could flow down the tube as air temperature changed in the room. It was found that the room temperature could vary considerably; a range of 22 $^{o}$C to 26 $^{o}$C was noticed for different days. During an experiment the room temperature could vary by 4 $^{o}$C during a few hours.

A single thermocouple was used to measure the air temperature in the cavity. To achieve better results, measurements were taken after a steady state was reached, and the average of these was used to indicate the temperature at that spatial location. By comparing the standard deviation, it was found that 50, one second interval readings, had the same standard deviation as higher number of readings, so this was the number of readings collected for all spatial points. For a given spatial location, the standard deviation never went greater than 0.2 $^{o}$C, giving confidence that the average value was very consistent. As for the spatial resolution, this was adjusted from 1 mm to 5 mm depending on the temperature gradient in the area. In general, it was found that the temperature did not vary greatly across the gap, even close to the glass surface. One of the reasons for not being able to capture high temperature gradients at the wall is likely due to the conduction down the thermocouple wire from the tip. One of the other issues that could lead to uncertainty with the temperature profiles is the sealing of the thermocouple probe, although care was taken to reduce this. The thermocouple used to measure the air temperature profile contacted the glass for the last reading.

Shading from direct radiation from the illumination system was provided for the velocity and air temperature profile measurements. Other forms of radiation were allowed to be incident on the thermocouple, including reflected solar radiation and emitted long wave radiation.

## 2.8 Velocity Measurements

In order to measure the air flow velocity in the gap, a high sensitivity velocity probe was used. As mentioned earlier, holes were drilled in the inner glass for inserting the probe into the gap. Since the gap sizes to be tested can be quite large, up to 70 cm, a large range traverse had to be purchased in order to mount the velocity probe and accurately locate its position in the gap. The velocity measurements were taken by means of a ComfortSense probe. This probe is omnidirectional, meaning it can measure the velocity at almost any direction the air flows towards it due to its spherical shape. The main disadvantage is that it does not take into the account the direction of velocity. Some of the benefits of the ComfortSense hotwire probe are that it has a temperature sensor built in and is factory calibrated to almost near zero velocities. There are other velocity probes available; 3-hole and 5-hole probe which will measure the direction of the velocity therefore taking into account the recirculation zones.

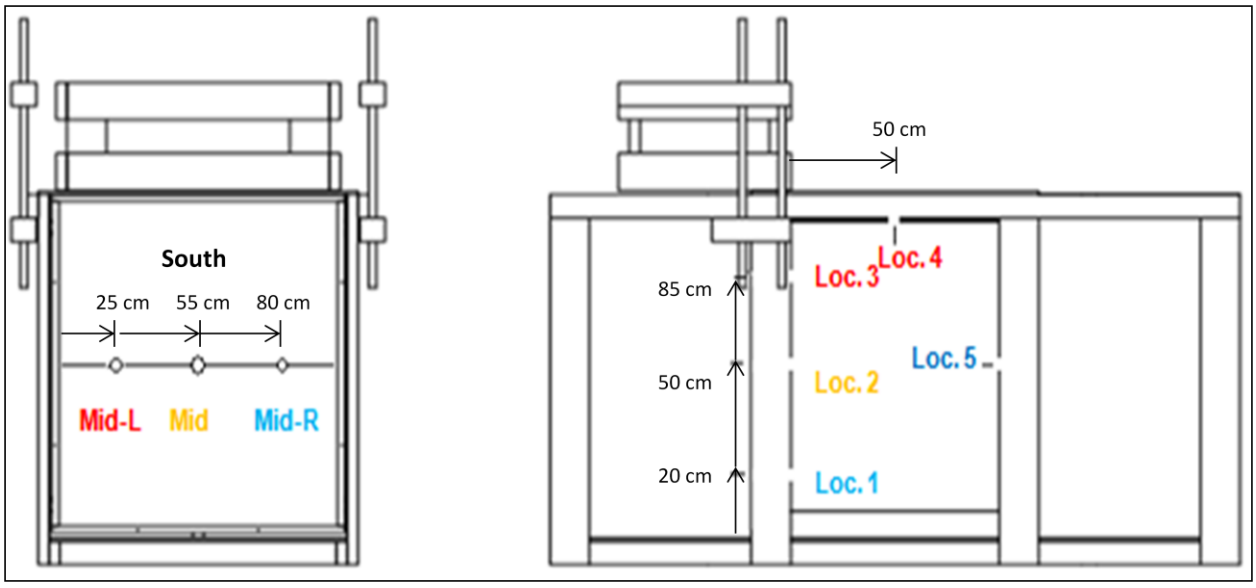


**Figure 2-5: Velocity and temperature measurement locations in the Experimental Setup**

The 7 locations that the velocity was measured at can be seen labelled in 2-5. The velocity measurements were taken by means of a ComfortSense probe. This probe is omnidirectional, meaning it can measure the velocity at almost any direction the air flows towards it due to its spherical shape. Some of the benefits of the ComfortSense hotwire probe are that it has a temperature sensor built in and is factory calibrated to almost near zero velocities. Some of the limits of the ComfortSense probe are that it is 3 mm in diameter, rendering it hard to capture the high velocity gradients close to the wall, and since it only has a frequency response of 2 Hz, it is unable to get turbulent properties. Due to the fact that the built in temperature sensor is 3.5 cm behind the velocity probe along the axial length, it does not measure in the same vicinity as the velocity probe. The ComfortSense probe cannot get a full temperature profile when traversing from one side of the channel to the other as the velocity probe would have to go through the glass for the temperature probe to traverse the whole length of the cavity.

A Microsoft Office Excel spread sheet provided from the supplier allowed conversion of the output voltage for both the velocity and temperature from the probe to the respective values, as well as a final correction to the velocity value for the effect of temperature, pressure and humidity. The details of the conversion can be seen in Appendix A. Also supplied with the probe was the calibration data required for the conversion.

Due to the turbulent nature of the flow, noticed by the variations in measured velocity, time averaging the measured velocity was done to represent the mean velocity at a spatial location. Following in the work of previous

researchers (Ryan and Burek 2010) and (Kelton 2011), it was decided to use 100 samples per spatial location. The time per spatial location was less than 2 minutes with a second between every reading. It should be noted that the mean of a first hundred samples could be 5% different than the mean of the second hundred samples, resulting in quite variability in velocity. This is also seen in the standard deviation of the velocity reaching 35% of the mean value in the flow close to the second glass. For the lowest horizontal profile, Location 1, in the region where smoke visualisation of the flow by previous researchers La Pica et al. (1993) indicated recirculation, the standard deviation is higher than the mean velocity found. One would have hoped that for this region the mean velocity would have gone close to zero, and then gone back up again. This would have indicated a switch from upward to downward flow. The current experimental results, which have no clear indication of a switch from upward to downward flow, may be a sign that the recirculation zone is constantly changing in size. This would make it hard to compare the current experimental work at this location to steady state numerical results that predict a single size recirculation zone. As would be expected, the downward velocities in the cavity are shown as positive absolute velocities when measured with the velocity probe. Hence the mass flow rate for the lowest horizontal profile, Location 1, turns out to be higher than all the other mass flow rates found in the cavity.

Measurements at near zero velocities are very uncertain with hotwire probes. One of the phenomenon's of hot wires is the natural convection flows that they cause due to overheat. Hence, owing to natural convection, there is always some velocity going past the probe, even in what would be still air. The

manufacture limit of ± 0.02 m/s uncertainty only applies down to 0.05 m/s. However, the calibration data that came with the velocity probe goes down to 0.0027 m/s. The problem comes in the regions close to the wall and in recirculation zones. In these regions many of the readings would be below 0.05 m/s, and the question becomes what value should be put in for this reading. If zero is put in for everything below 0.05 m/s, the mean will be lowered, increasing the standard deviation of the readings artificially. So to reduce this lowering bias error, it was decided to use the calibration curve down to 0.0027 m/s, and a zero reading would be used only for values under 0.0027 m/s. It is understood that the accuracy is not going to be good for measurements under 0.05 m/s, but the method mentioned will have less bias to it than putting in zero for all readings below 0.05 m/s.

Time averaging to find the mean value of the velocity was done by converting all 100 measured velocity voltages at a spatial location into a velocity, then calculating average of all the velocities to get the mean velocity. The spatial resolution was varied depending on the velocity gradient. Near the inner glass the velocity goes from zero to reaching its maximum 2 to 3 cm away from the glass. In this region the spacing was typically 1 to 2 mm, outside this region the spacing was increased to a maximum of 5 mm. Since the probe is 3 mm in diameter, the spatial resolution is often less than the size of the probe which gives the measurement of the averaged heat loss over the diameter of the probe. This entails an additional uncertainty in the high velocity gradients as one edge of the probe will experience one velocity and the opposite edge would experience a

different one. The velocity probe was not in contact with the glass surface to make sure that it will not be damaged.

## 2.9 Calibration

### *2.9.1. Pyranometer*

The pyranometer was factory calibrated. There was a linear calibration of 14.8 μV per $W/m^2$, which is valid from 0 to 2000 $W/m^2$.

### *2.9.2. ComfortSense Probe*

The ComfortSense probe was factory calibrated as well. The calibration curve is a nonlinear relation between the velocity and temperature.

### *2.9.3. Thermocouples*

A Hoskin RTD was used to perform a two point check on the thermocouples. The RTD had a 0 to 200 $^oC$ range with 1/10 DIN accuracy, giving a max error of ±0.08 $^oC$ at 100 $^oC$. Two calibration points were used by using an ice bath and a boiling bath. For the ice bath both the RTD and built in type T calibration curve on the Hydra Series II for all thermocouples gave a reading of 0.0 $^oC$. For the boiling bath the RTD was reading 100.0$^o$ C, most thermocouples with the built in calibration curve gave this as well, however a few gave higher reading with the max being 100.3$^o$ C. Given that only two points were taken, a linear curve would fit perfectly. But the built in calibration curve is not linear, so it was expected that the built in calibration curve would perform much better than a linear one, and thus the built in calibration curve in the Hydra Series II was used

for all the thermocouple readings. The calibration was based on the RTD, meaning the atmospheric pressure didn't affect its calibration. The atmospheric pressure was still recorded, for ice bath it varied from 100 to 101 KPa where for boiling bath it was 99.8 to 101.2 KPa.

Thermocouples are simple instruments that are crucial in proving the basic functionality of the experimental set-up. We will need to place thermocouples around the gap, to prove that the temperature trends are as expected around the thermal buffer zone. With the assistance of *ANSYS CFX*, we have noted the location of critical regions in the buffer zone. Using this information, we can allocate sufficient number of thermocouples in order to properly understand the difference between temperature gradients.

In total, there will be 52 Thermocouples, 36 of which will be used from a former prototype. The arrangement of the thermocouples was shown in figure 2-4 and it's worth noting that the vertical walls are having thermocouples placed on both sides, but the horizontal walls do not have thermocouples except the out walls of the TBZ having them on the inside only.

The left side of the figure is the south side wall, and because it has the most temperature variation, it has a denser concentration of thermocouples. The top and bottom gaps do not have much temperature variation, and thus there is sparse distribution.

## 2.10 Uncertainty Analysis

The uncertainty for each measuring device was approximated using the manufacturer's data and accounting for experiment dependant uncertainty.

These independent uncertainties are then propagated through the respective equations to find the uncertainty of the dependant variable.

The equation for propagation of uncertainty is:

$$u(R) = \left[\left(u(\mathrm{W}_1)\frac{\partial \mathrm{R}}{\partial \mathrm{W}_1}\right)^2 + \left(u(\mathrm{W}_2)\frac{\partial \mathrm{R}}{\partial \mathrm{W}_2}\right)^2 + \cdots + \left(u(\mathrm{W}_\mathrm{n})\frac{\partial \mathrm{R}}{\partial \mathrm{W}_\mathrm{n}}\right)^2\right]^{1/2} \qquad \textit{Eq. 2-1}$$

Where: u()=uncertainty in ( ), R= calculated result, and Wn=nth variable.

Using uncertainty values of ±0.02 m/s for velocity, ±1.0 $^{o}$C for air temperature measurements, ±0.0001 m for spatial distances, and ±10% for the pyranometer readings, the propagated uncertainty could be calculated. Looking at the example case of 380 W/m$^2$ on the outer surface and 10 cm spacing behind the glass, the following uncertainty was found and represents the propagated uncertainty for the other experiments as well. The uncertainty in the total mass flow was ±10.7%.

# Chapter 3

# 3. Experimental Results

## 3.1 Experimental Results

The physical experimental setup, along with the locations where the air velocity and temperature measurements were taken in the cavity, is shown in the figure 3-1. Locations 1, 2 and 3 are 25 cm, 50 cm and 80 cm from the bottom ledge, respectively. Location 4 is 50 cm from the inner glass and Location 5 is 50 cm from the bottom ledge. The Natural convection loop in the Thermal Buffer Zone is indicated by the arrows in the cavity.

The parameter that changed was the spacing between the inside of the outer glass and the inner glass, B, changing the aspect ratio of B/H in the cavity. All other geometrical parameters remained constant in all experiments conducted. In table 3-1, the average vertical centerline heat flux incident on the second glass can be seen to decrease with increasing B/H ratio. This is due to the fact that radiation diverged as the distance between the second glass and the illumination system increased. The second parameter that can be changed is the

space between the illumination system and the outside of the glass, L, resulting in a change in the heat flux incident on the outer surface.

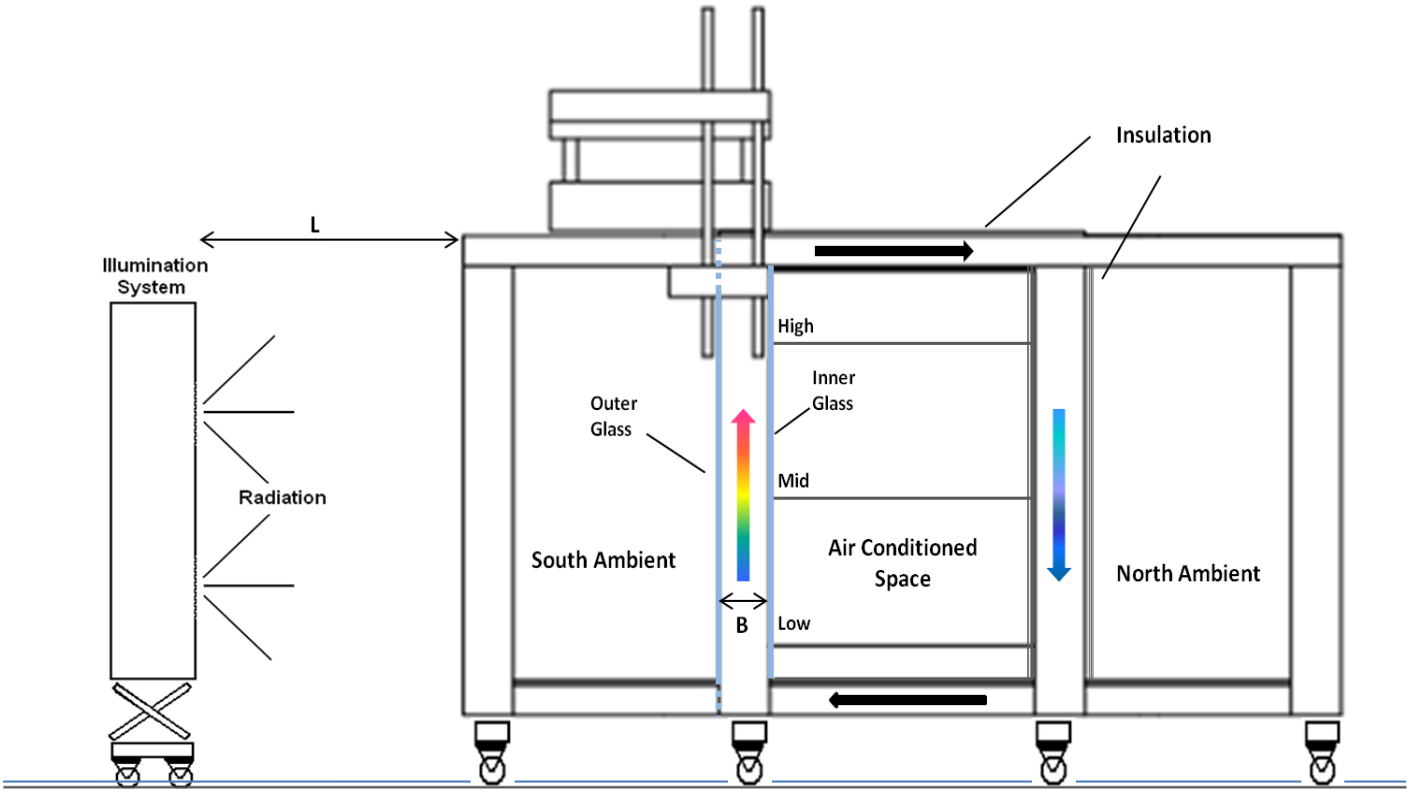


**Figure 3-1 Experimental Setup**

Due to the high absorptivity of the second glass, it is assumed that once solar radiation enters the cavity, most of it will stay there. So, for a constant L spacing and increasing B, the total energy in should be roughly the same. However, the radiation energy will be spread over a larger surface area as the

top and bottom ledge surface area increases with increasing B. This results in the decreasing heat flux incident on the second glass.

**Table 3-1 Experiment Configuration**

| Experiment | B/H | L (m) | Avg. Vertical Heat Flux Outside Glass ($W/m^2$) | Avg. Vertical Heat Flux Inside Glass ($W/m^2$) |
|---|---|---|---|---|
| 1 | 0.1 | 1.38 | 380 | 258 |
| 2 | 0.2 | 1.38 | 380 | 233 |
| 3 | 0.3 | 1.38 | 380 | 208 |
| 4 | 0.4 | 1.38 | 380 | 189 |

Pyranometer measurements on the two dimensional vertical surface were taken in front of the glass for the distance L which was used to calculate the total energy incident on the south facing glass. The same measurements were taken behind the glass for all four experiments to calculate the total energy incident on the inner glass. Refer to Tables and plots of all these values listed in Appendix B.

As previously mentioned in the literature review, the initial loss of energy comes from the optical properties of the system. The ratio of the radiation measured behind the glass to what is incident on the front of the glass is its optical efficiency. Figure 3-2 shows the optical efficiency based on the average heat flux incident on the vertical center line of the glass. The optical efficiency

decreased with increasing the B/H aspect ratio. This is due to the increase in surface area of the cavity that the radiation is spread over.

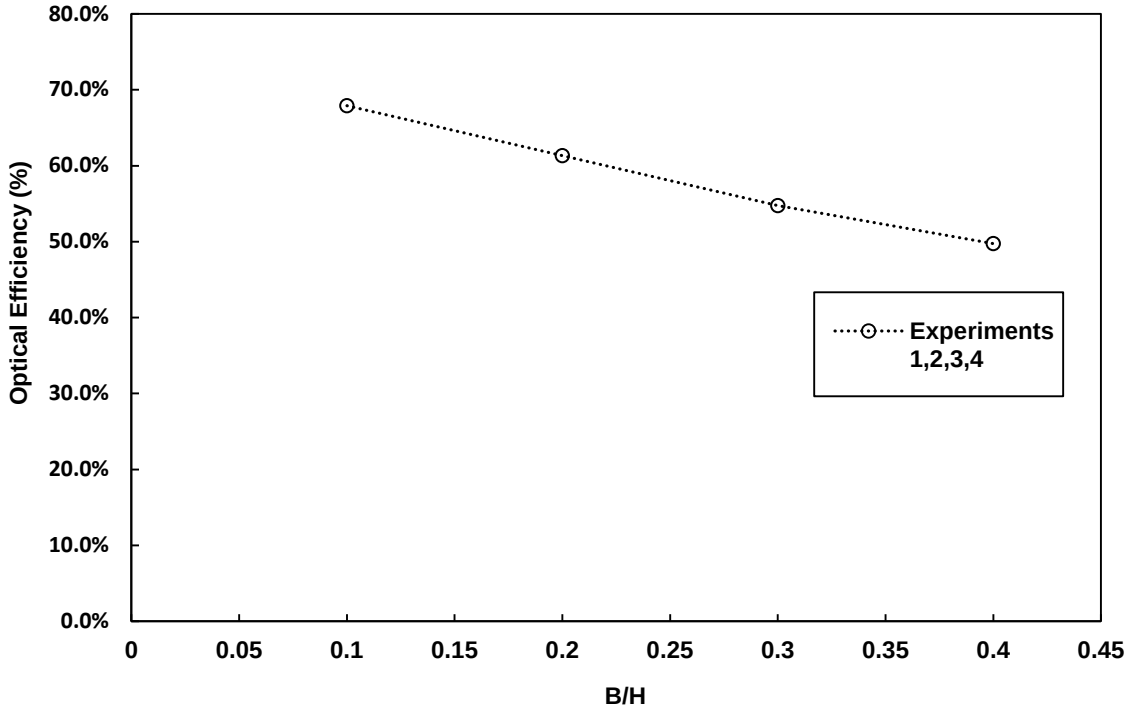


**Figure 3-2 Optical efficiency vs. B/H aspect ratio for each experiment**

The velocity and air temperature profiles for the seven locations are shown for all experiments in Figures 3-4 to 3-27.

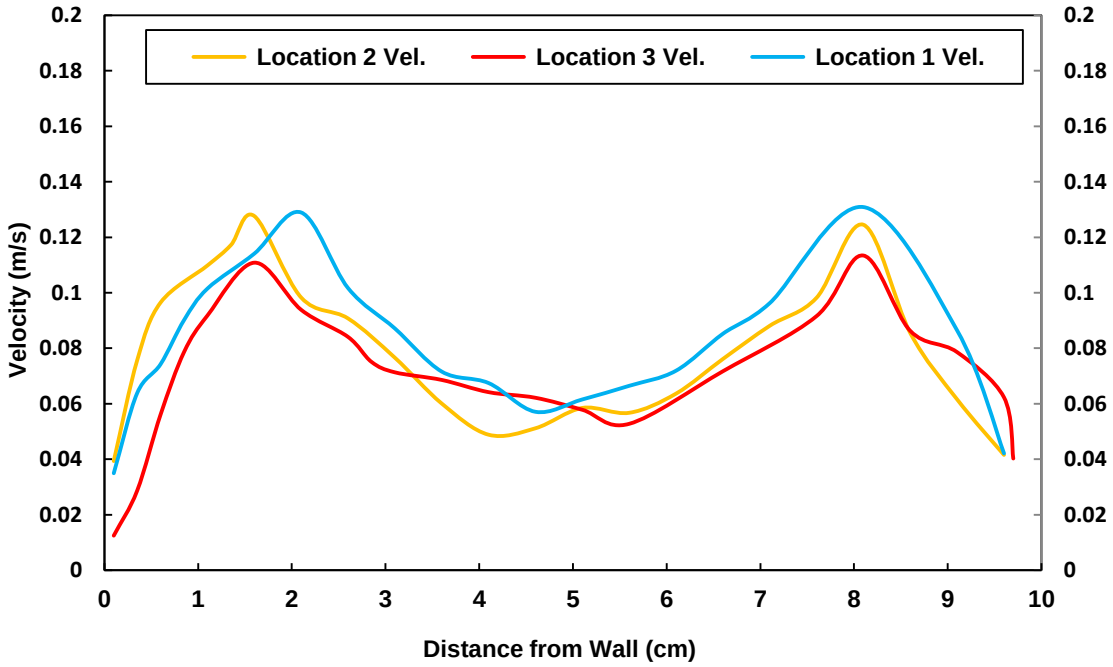


**Figure 3-3 Velocity profile for Experiment 1 at locations 1, 2 &3**

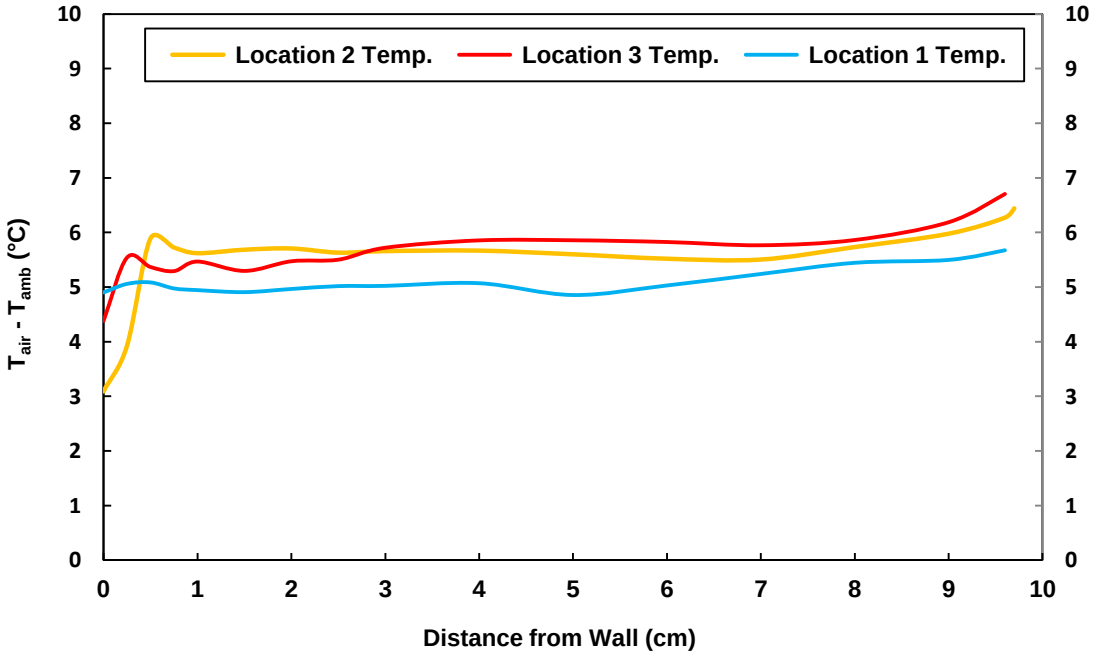


**Figure 3-4 Horizontal temperature profile for Experiment 1 at locations 1,2 &3**

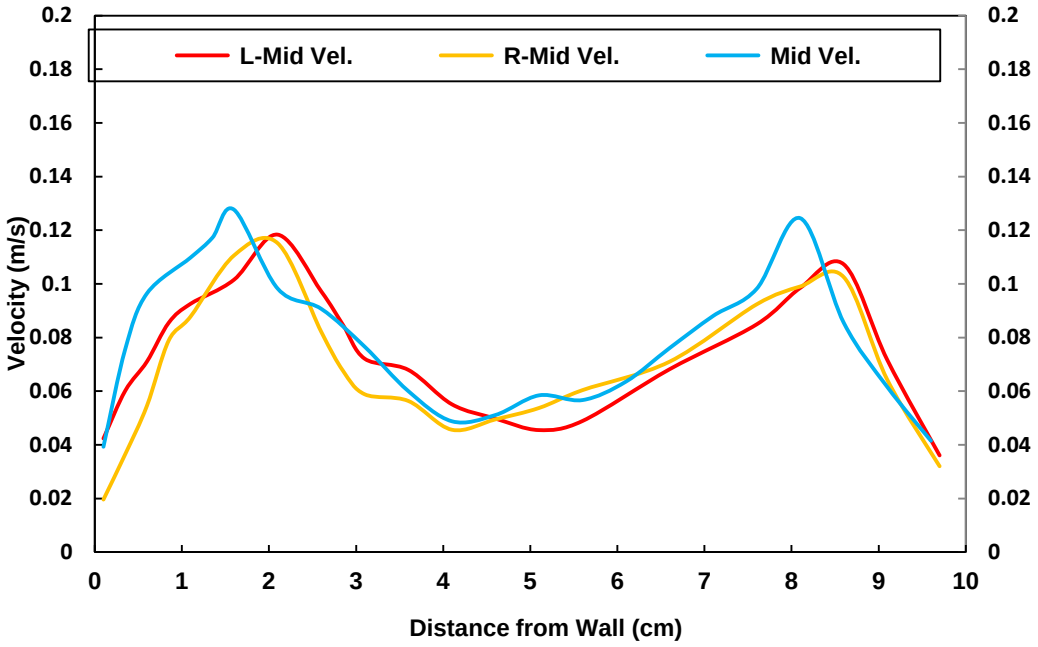


**Figure 3-5 Velocity profile for Experiment 1 at locations Mid, Mid L & Mid R**

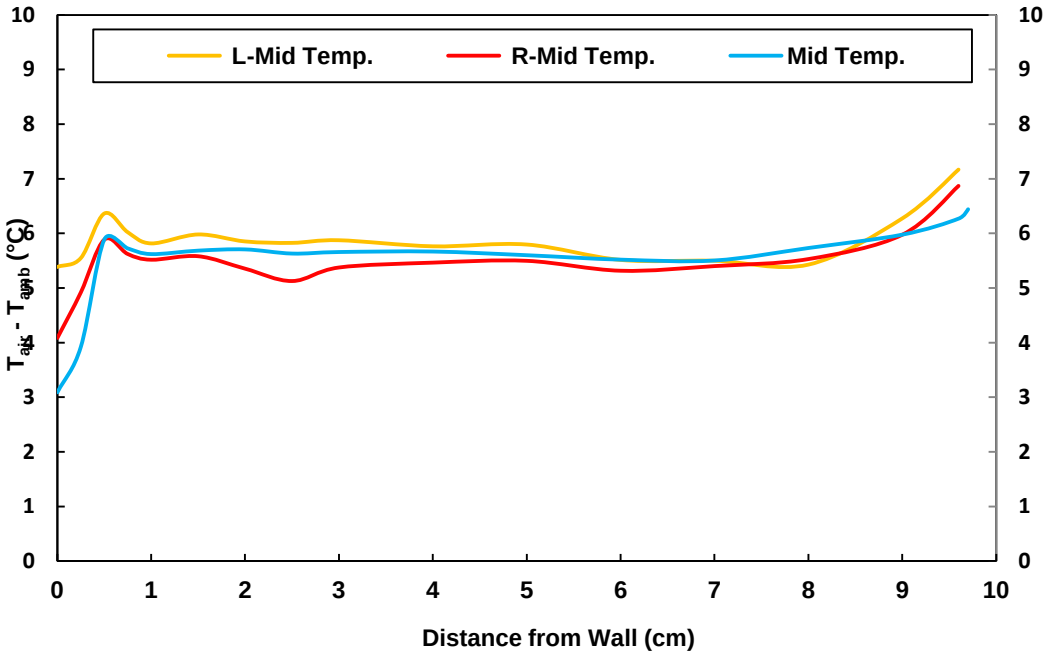


**Figure 3-6 Horizontal temperature profile for Experiment 1 at locations Mid, Mid L & Mid R**

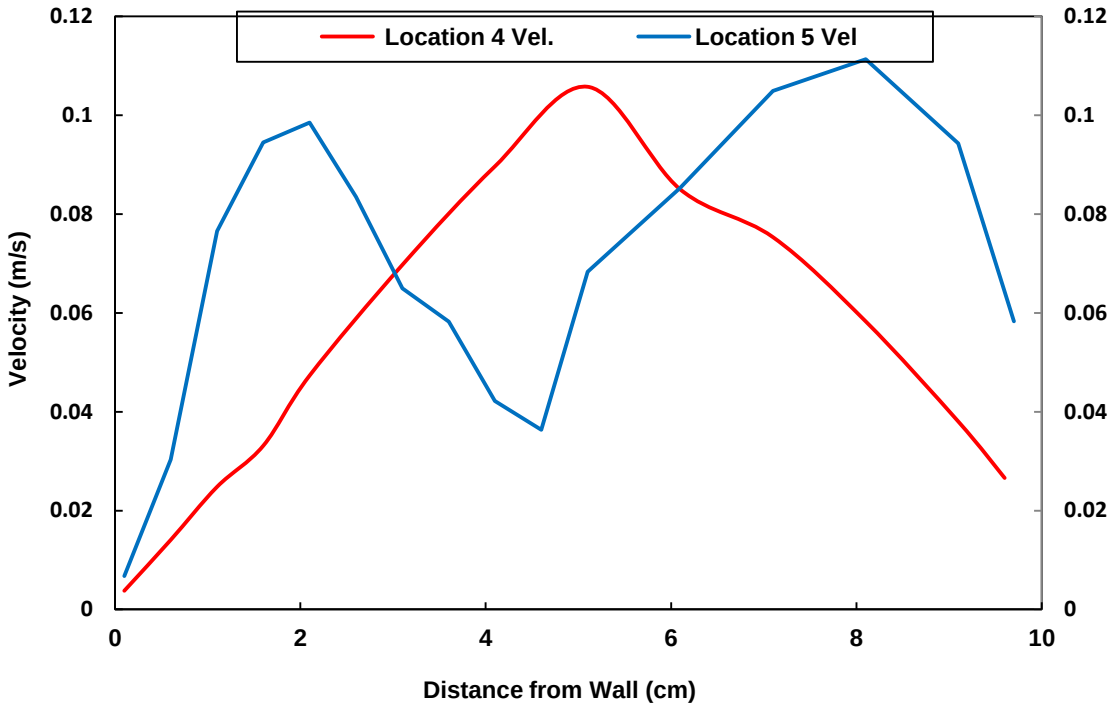


**Figure 3-7 Velocity profile for Experiment 1 at locations 4 & 5**

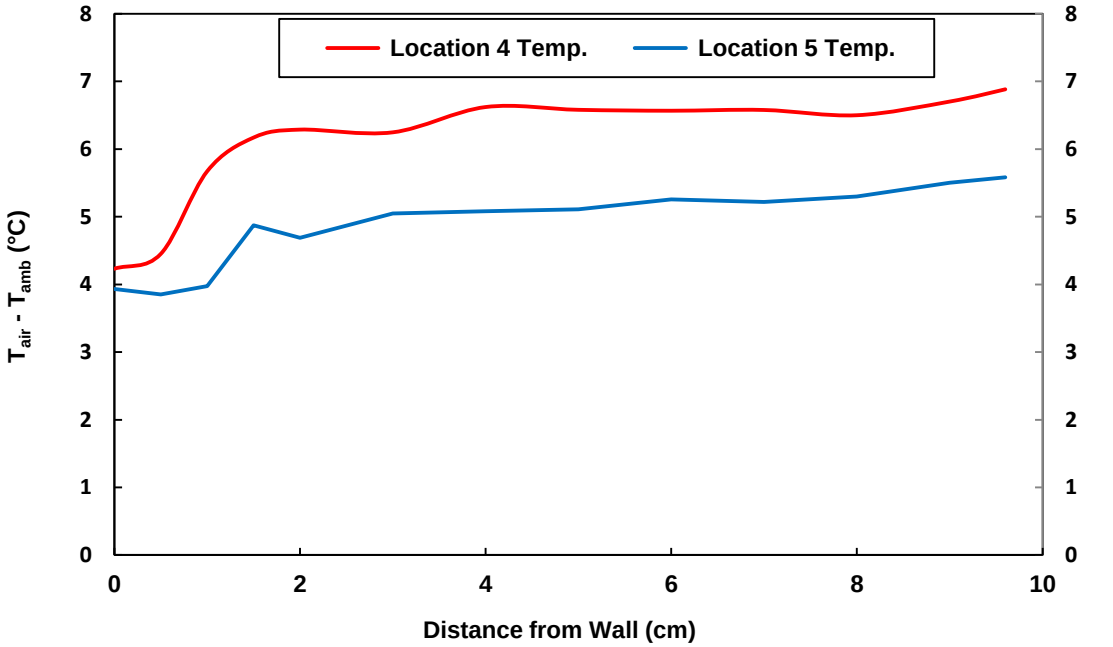


**Figure 3-8 Temperature profile for Experiment 1 at locations 4 & 5**

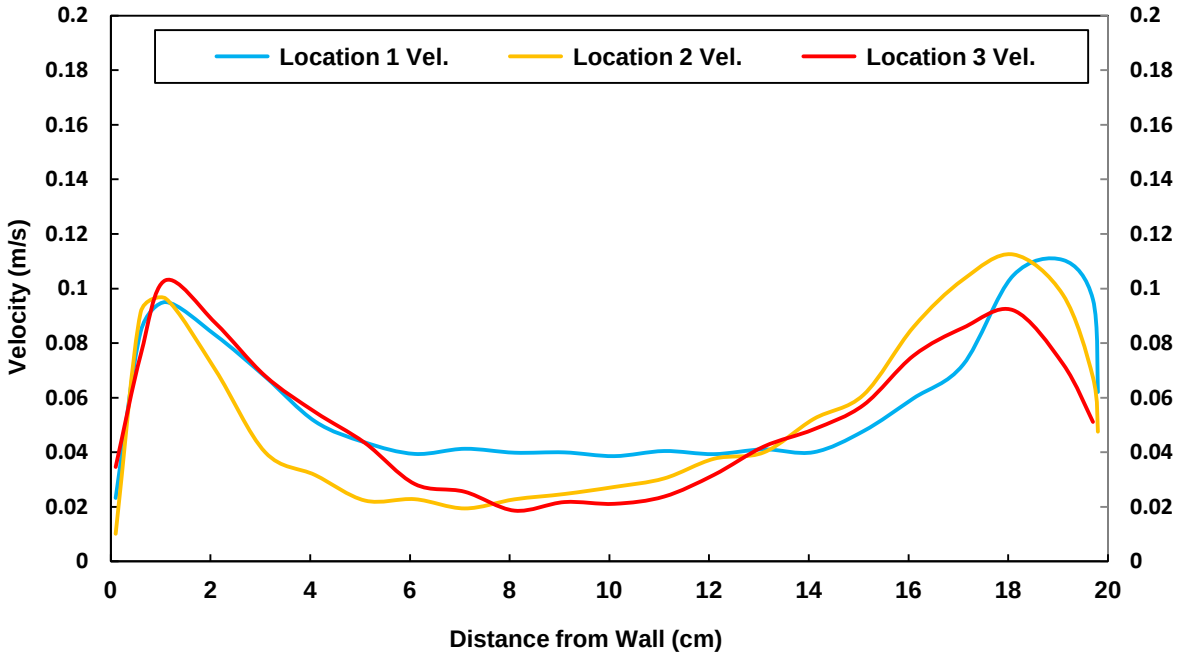


**Figure 3-9 Velocity profile for Experiment 2 at locations 1, 2 &3**

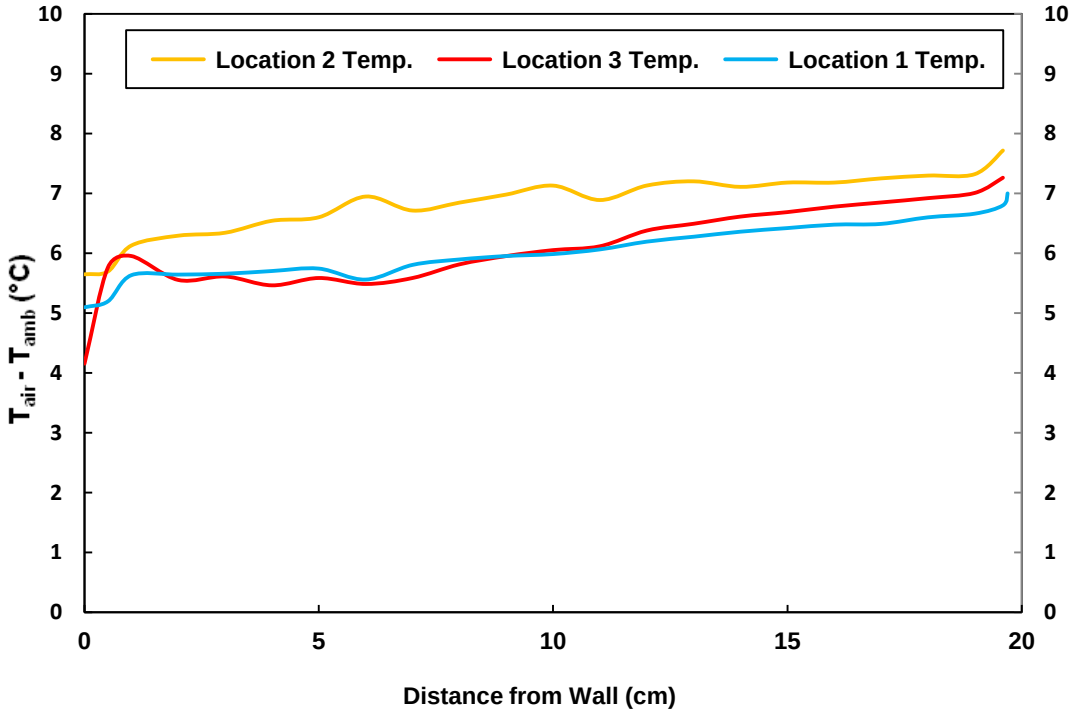


**Figure 3-10 Temperature profile for Experiment 2 at locations 1, 2 &3**

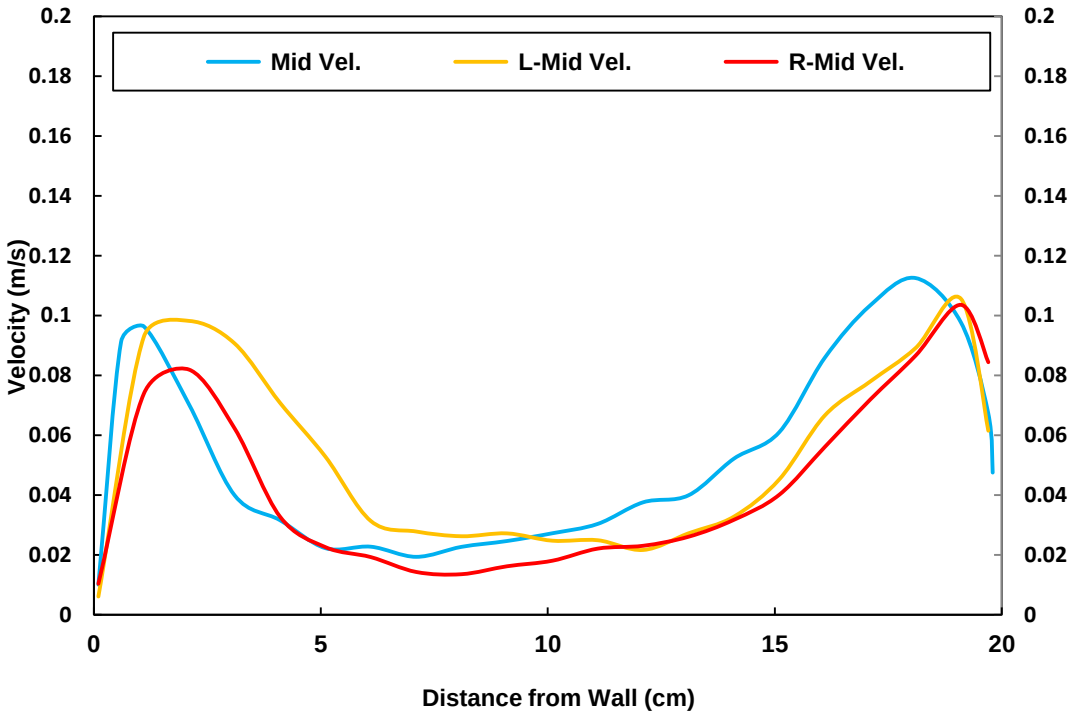


**Figure 3-11 Velocity profile for Experiment 2 at locations Mid, Mid L & Mid R**

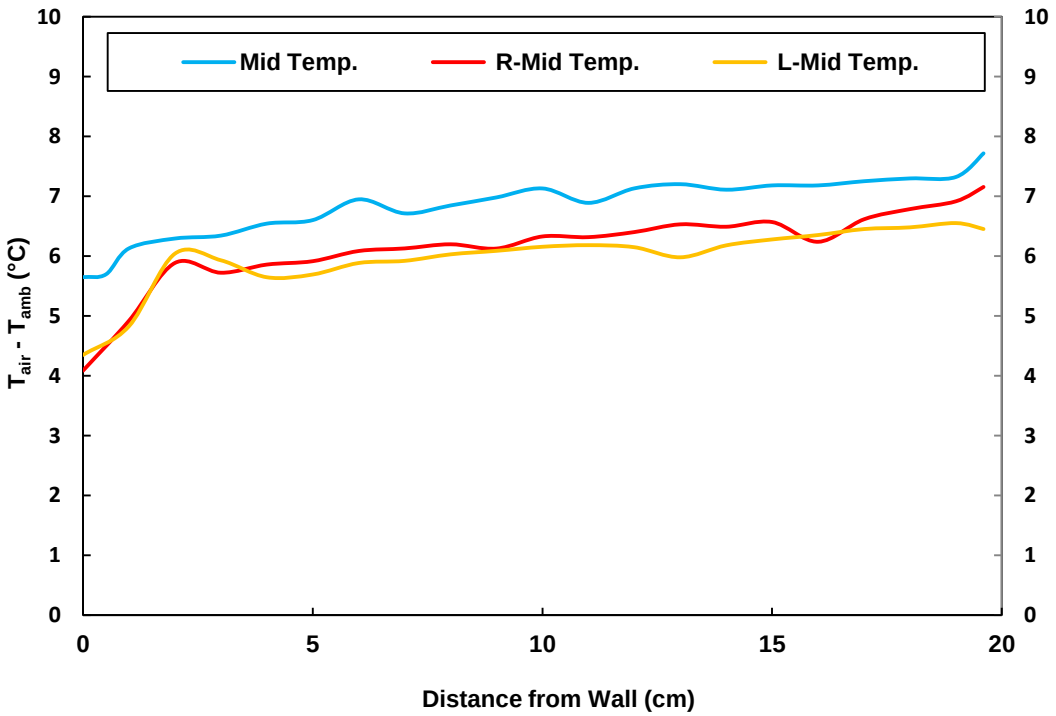


**Figure 3-12 Temperature profile for Experiment 2 at locations Mid, Mid L & Mid R**

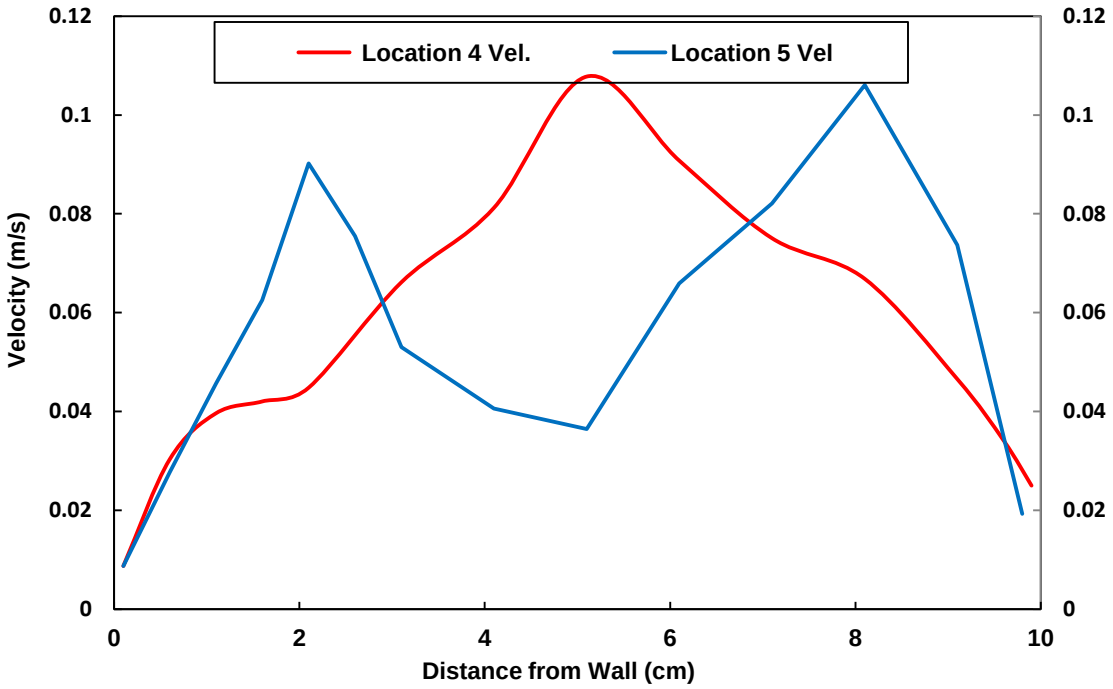


**Figure 3-13 Velocity profile for Experiment 2 at locations 4 & 5**

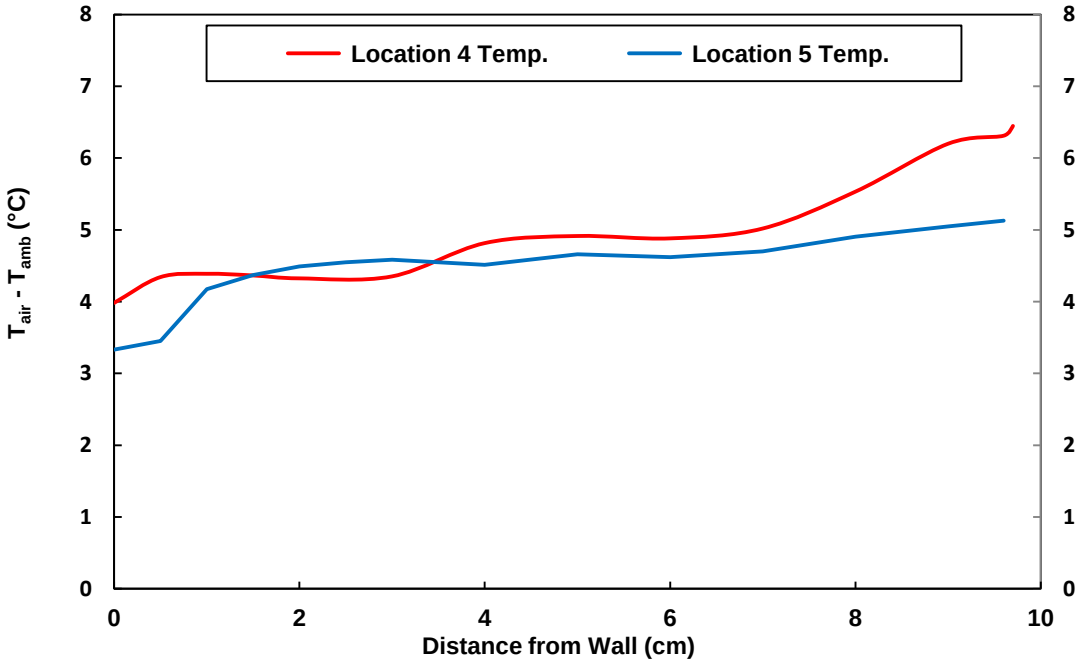


**Figure 3-14 Temperature profile for Experiment 2 at locations 4 & 5**

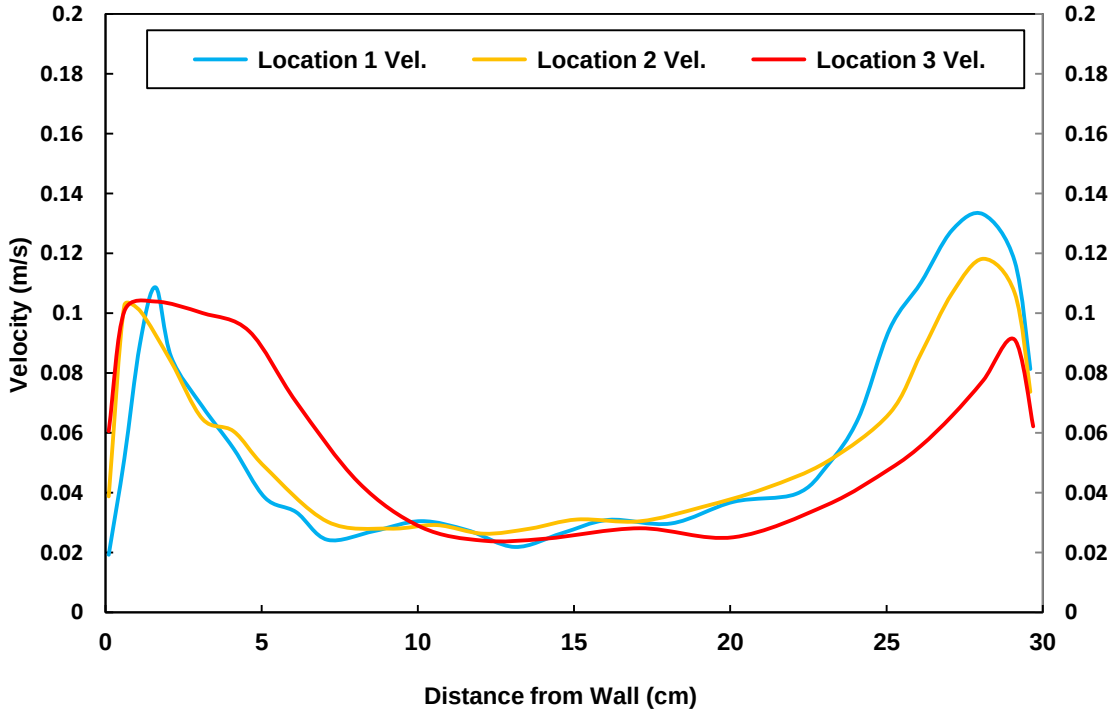


**Figure 3-15 Velocity profile for Experiment 3 at locations 1, 2 &3**

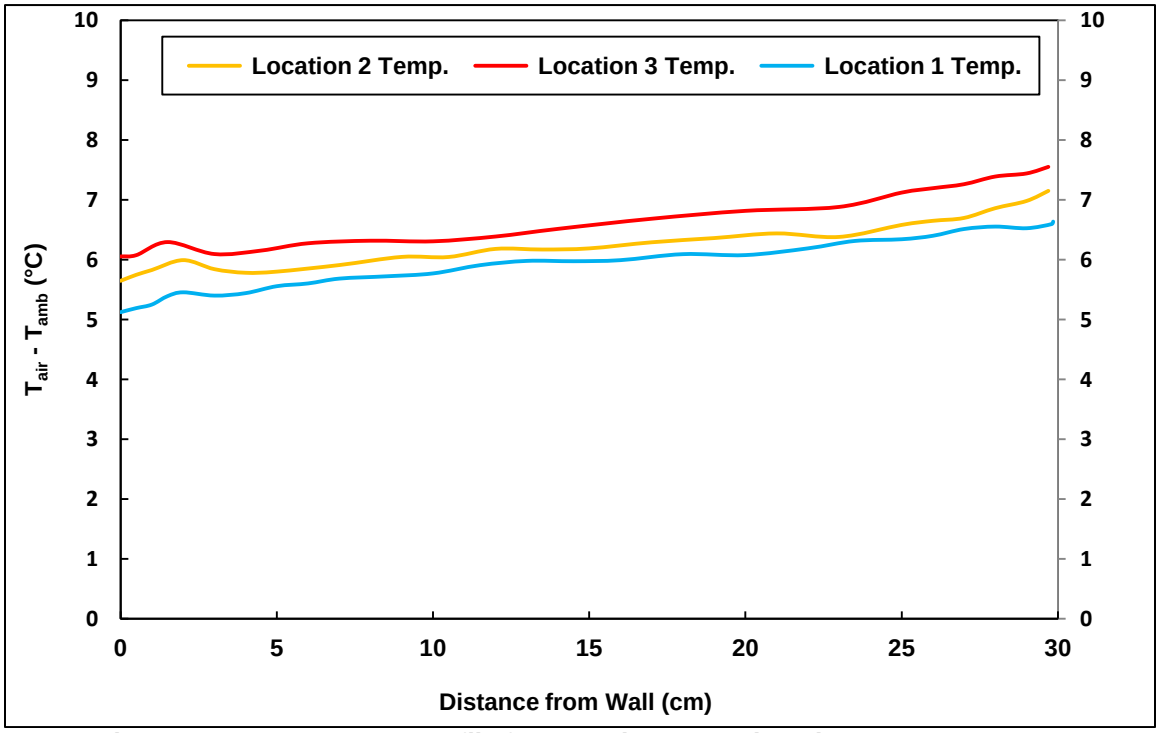


**Figure 3-16 Temperature profile for Experiment 3 at locations 1, 2 &3**

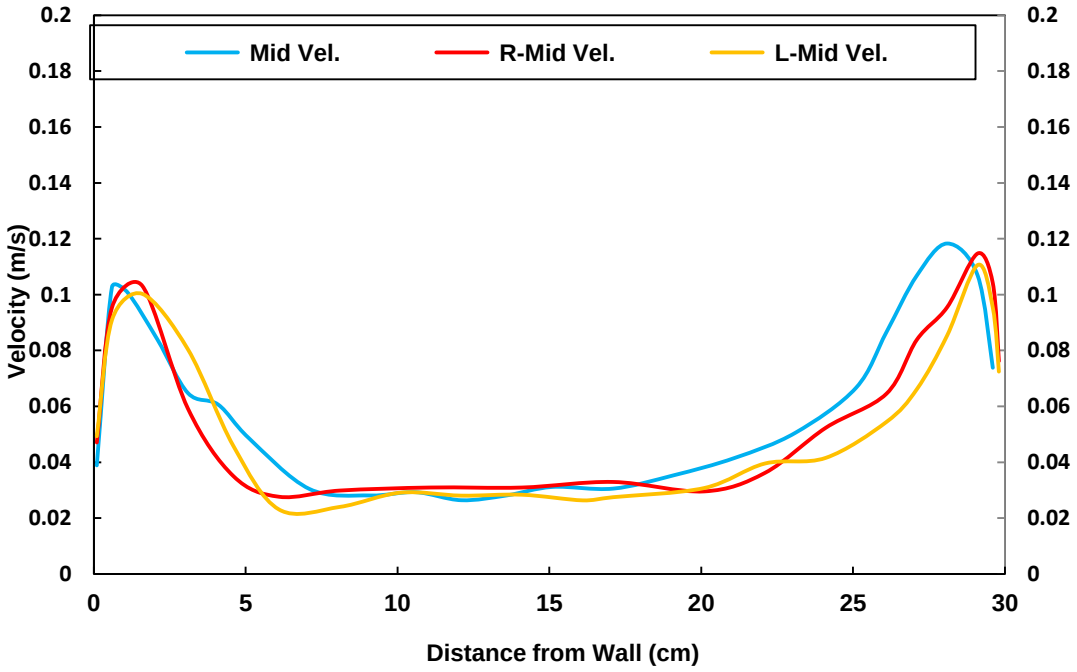


**Figure 3-17 Velocity profile for Experiment 3 at locations Mid, Mid L & Mid R**

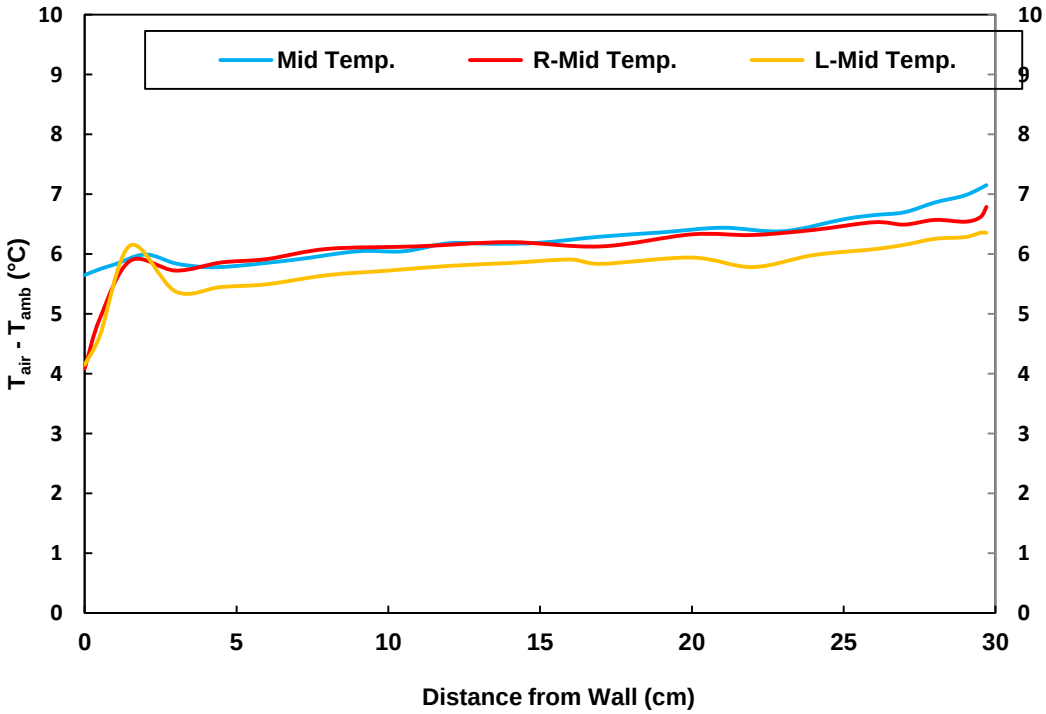


**Figure 3-18 Velocity profile for Experiment 3 at locations Mid, Mid L & Mid R**

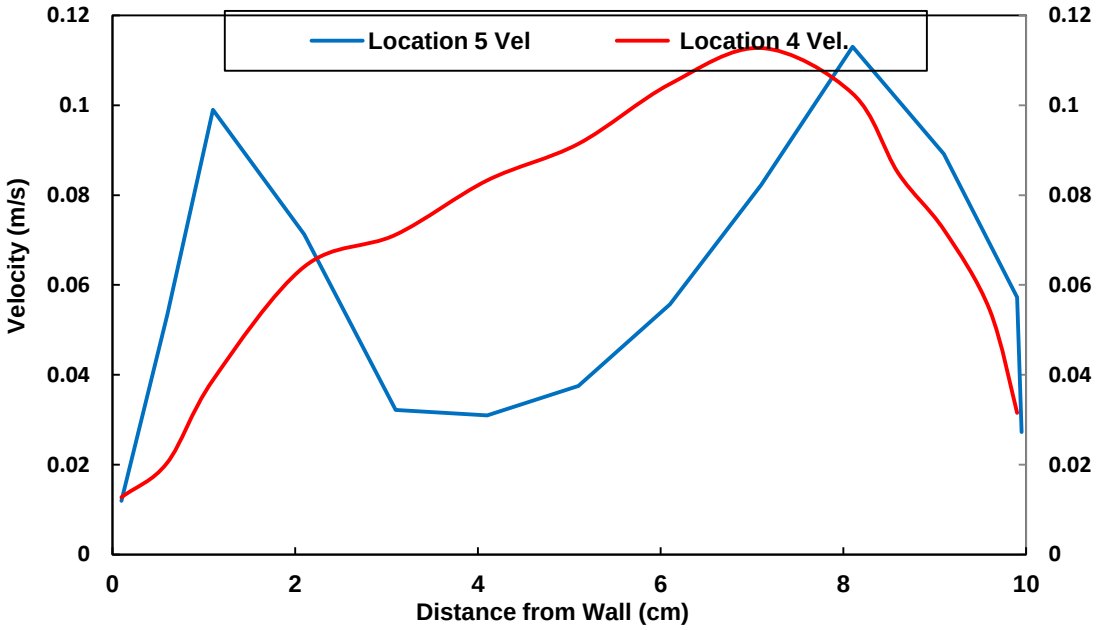


**Figure 3-19 Velocity profile for Experiment 3 at locations 4 & 5**

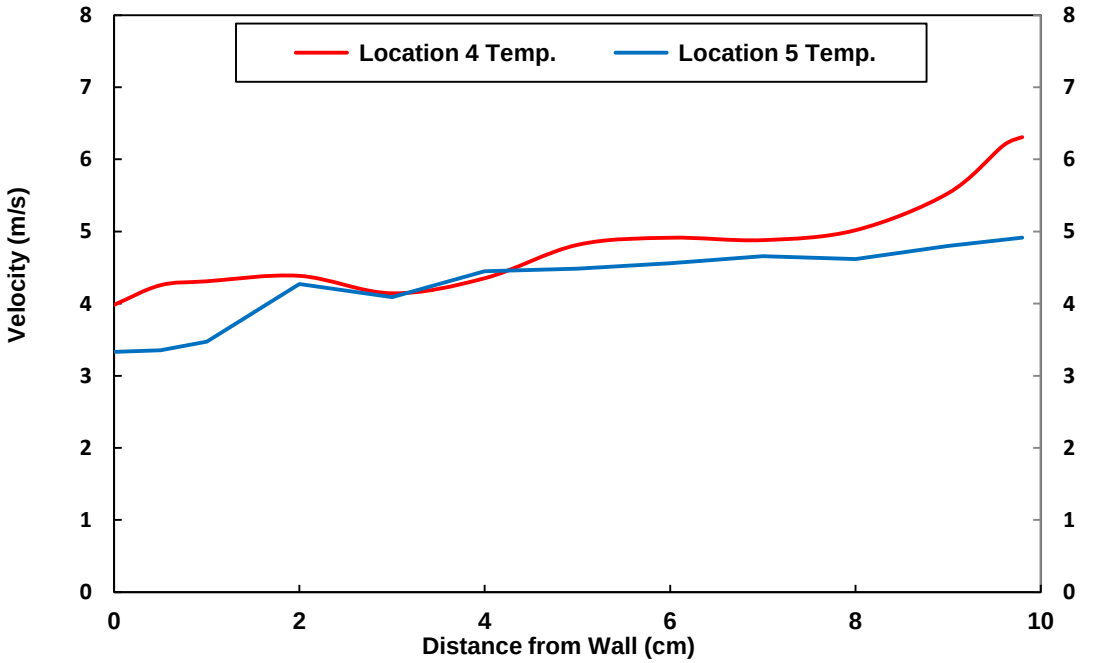


**Figure 3-20 Temperature profile for Experiment 3 at locations 4 & 5**

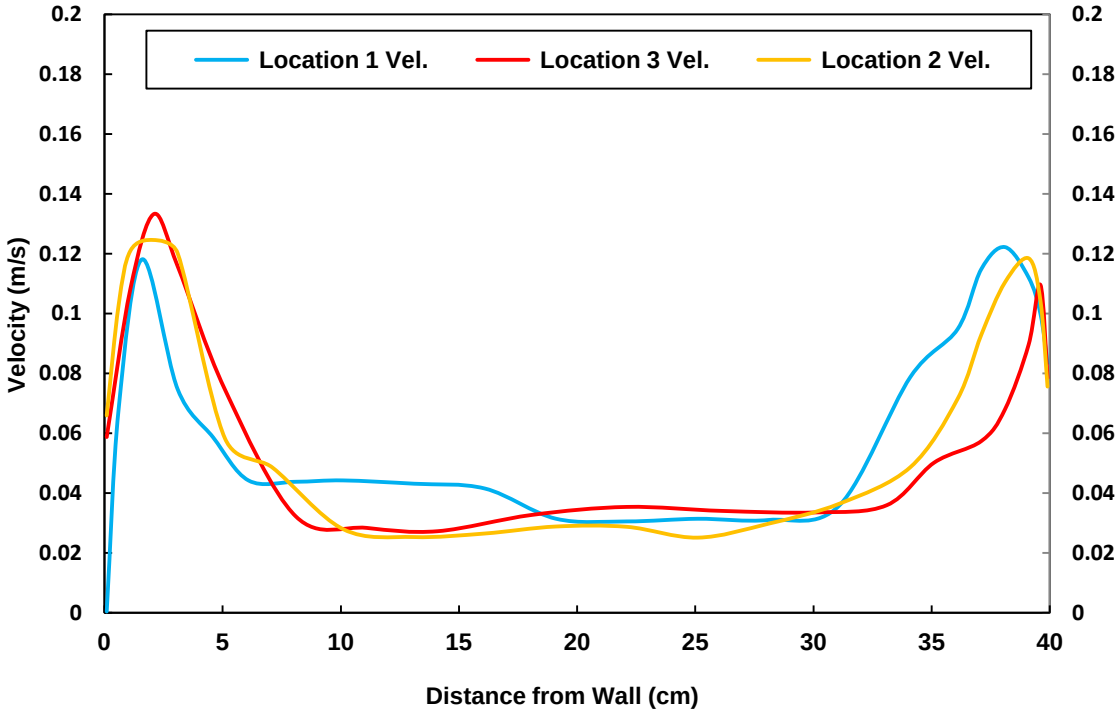


**Figure 3-21 Velocity profile for Experiment 4 at locations 1, 2 &3**

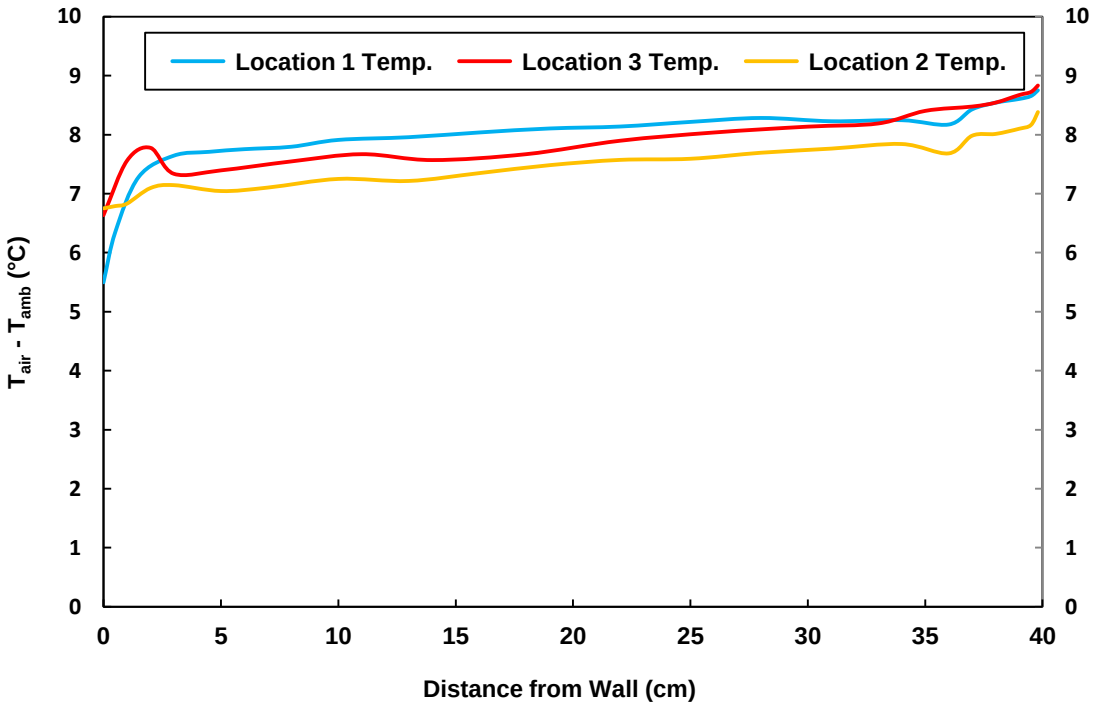


**Figure 3-22 Temperature profile for Experiment 4 at locations 1, 2 &3**

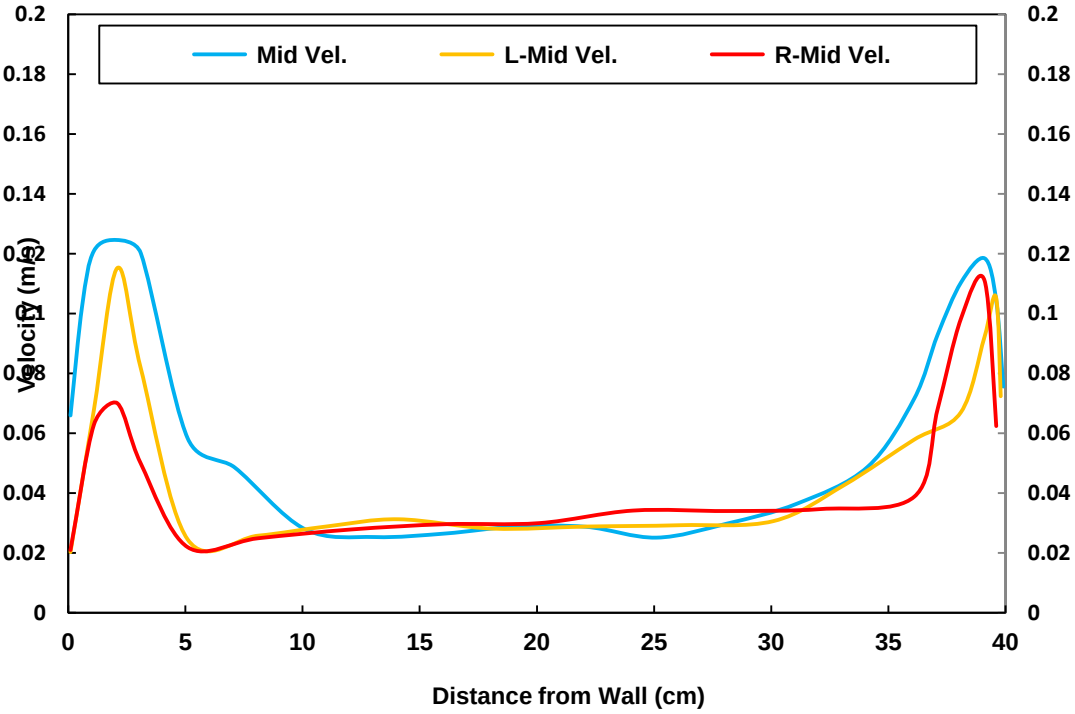


**Figure 3-23 Velocity profile for Experiment 4 at locations Mid, Mid L & Mid R**

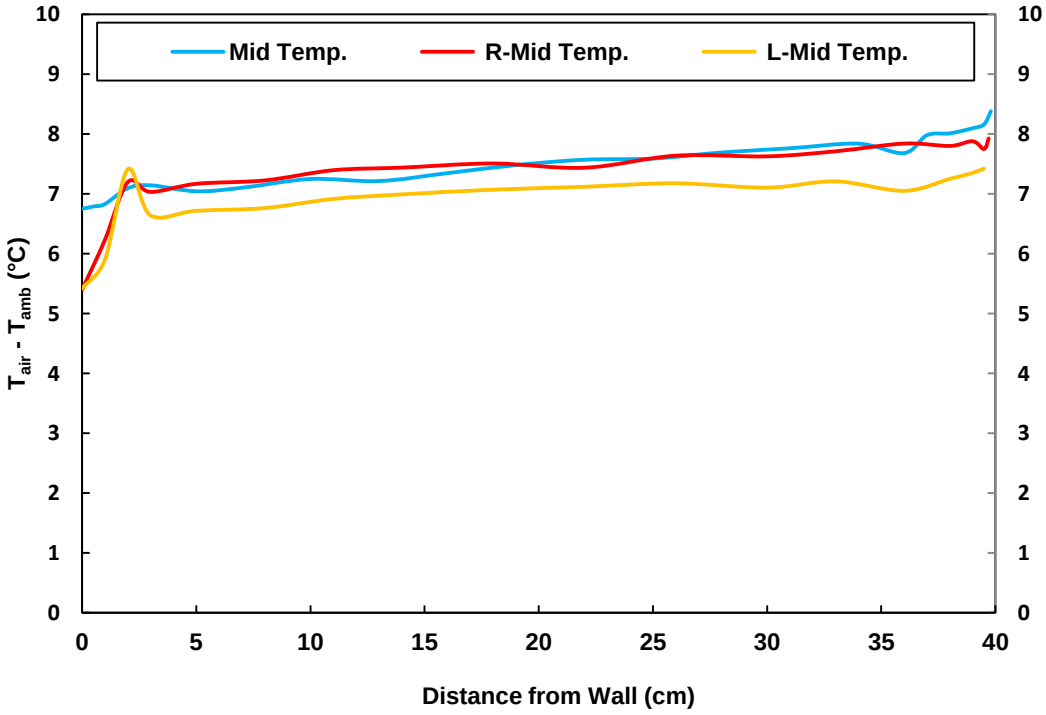


**Figure 3-24 Temperature profile for Experiment 4 at locations Mid, Mid L & Mid R**

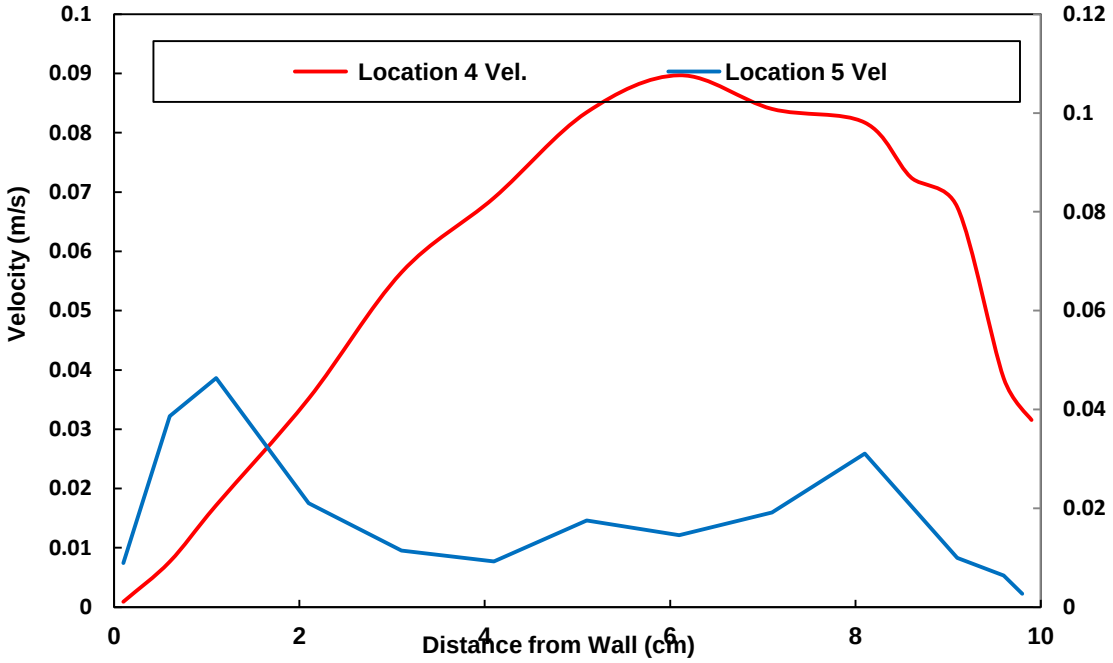


**Figure 3-25 Velocity profile for Experiment 4 at locations 4 & 5**

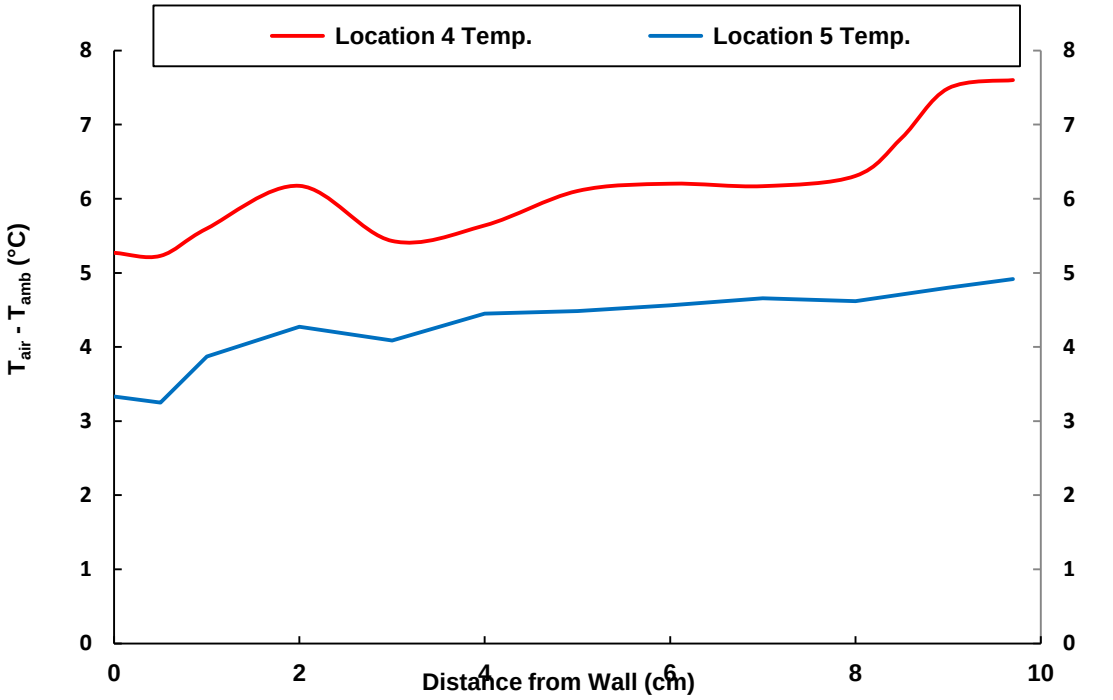


**Figure 3-26 Temperature profile for Experiment 4 at locations 4 & 5**

Figures 3.4 - 3.26 show two peaks for the velocity profile; the velocity increases to a maximum a few centimetres from the inner glass surface, decreases after this and peaks once more a few centimetres before the outer glass surface. The location 4 velocity only peaks once compared to location 1, 2, 3, and 5. The maximum velocity decreases as the B/H aspect ratio is increased, as there is more area for the flow to pass through. After a certain gap width not all the hot air from the south side makes it to the north side of the TBZ but creates a convection loop on one side since there is more resistance in the whole system. The velocity profiles are asymmetrical and it changes according to the recirculation zones, whereas the temperature profile is not dependent on them. The temperature profile has hydrodynamic and thermal boundary layers and there is certain difference between them, depending on the prandtl number the thermal boundary layer develops faster than the other. The air in the cavity is heated by both of the adjacent walls by means of natural convection. This creates an upwards buoyancy driven flow along each wall. The velocity profile would only be the same in the case of flow in channel.

As expected, the air temperature inside the cavity increases as the air passes upward through the cavity. The air temperature peaked close to the inner and outer glass; it either stayed constant or increased gradually moving towards the outer glass, and increased right at the outer glass wall. This increase at the glass wall indicates that some of the solar radiation energy absorbed in the glass has transferred to the air inside the cavity.

The dimensional comparison makes it hard to directly compare results as the glass spacing changed. To make direct comparison easier, variation of the

velocity, V, as a function of the dimensionless spacing, X/B, are shown in figure 3-27 at Location 3. This location was selected because it is least influenced by recirculation, so the assumption of upward vertical velocity was most accurate at this location. The spacing was made dimensionless by dividing the spacing by the gap spacing, B, of the experiment. The velocity was kept as measured during each experiment.

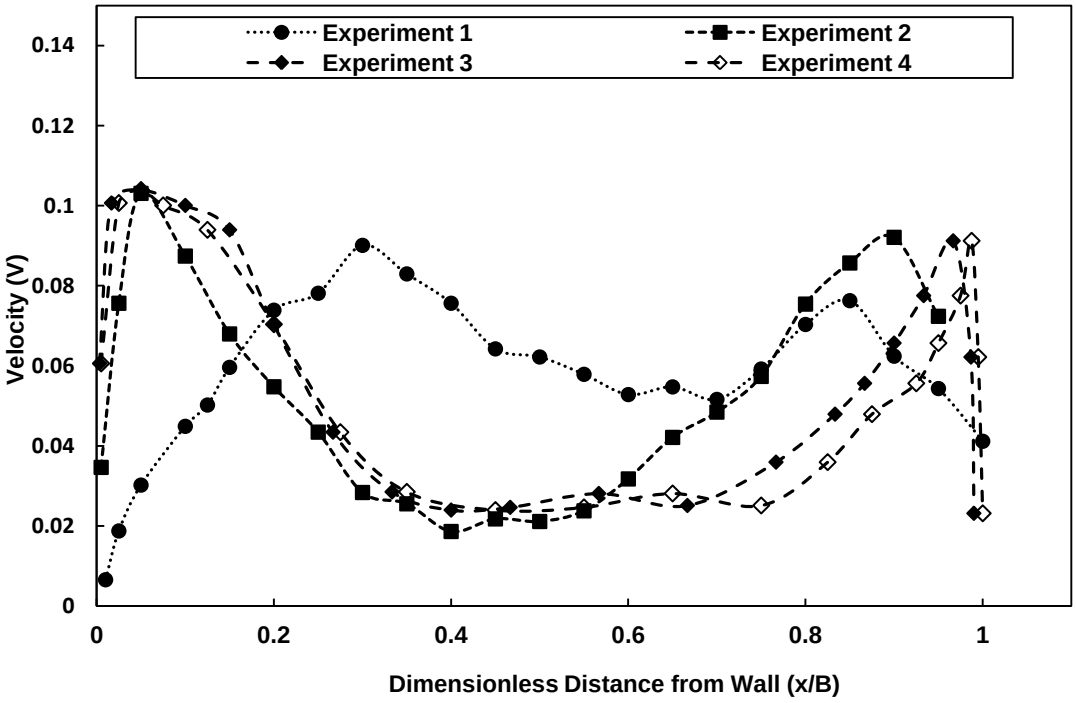


**Figure 3-27 Dimensionless velocity, characterized by the mass flow average velocity of each experiment, vs. dimensionless distance from the absorbing wall, characterized by B, at Location 3**

The mass flow rate for each experiment is compared at every location in the table below. One of the reasons for the difference in the calculated mass flow rate is that the hot wire probe only measures the absolute value of the air

velocity. So, if the flow is not perpendicular to the profile line, or if the flow is going in the opposite direction to that assumed, the integration of the velocity profile would reflect larger mass flow rate than what is measured.

**Table 3-2 Mass flow rate (Kg/s per m width) for locations 1,2,3,4 and 5**

| Experiment | Location 1 | Location 2 | Location 3 | Location 4 | Location 5 |
|---|---|---|---|---|---|
| 1 | 0.00971 | 0.00889 | 0.00883 | 0.00696 | 0.00647 |
| 2 | 0.01172 | 0.01083 | 0.01067 | 0.00801 | 0.00719 |
| 3 | 0.01636 | 0.01628 | 0.01604 | 0.00977 | 0.00845 |
| 4 | 0.02578 | 0.02501 | 0.02480 | 0.00743 | 0.00237 |

**Table 3-3 Mass flow rate (Kg/s per m width) for south side along horizontal line**

| Experiment | Mid-L | Mid | Mid-R |
|---|---|---|---|
| 1 | 0.00853 | 0.00889 | 0.00850 |
| 2 | 0.01062 | 0.01083 | 0.01063 |
| 3 | 0.01547 | 0.01628 | 0.01576 |
| 4 | 0.01740 | 0.02501 | 0.01715 |

There is considerable variation in the calculated mass flow rate at each location for the experiments. More confidence in the results would be evident if the mass flow rate calculated at each location for an experiment were the same as the results of Experiment 3. With the absolute velocity measured in the experiment, it could be expected that the calculated mass flow rates at some locations would be larger than other locations without recirculation. However, as we can see from Table 3.2, mass flow rate is high at Location 1 in the beginning and gradually decreases around the thermal buffer zone. Recirculation alone

cannot account for the differences, one of the cause for decrease in mass flow rate is the three dimensional effects caused by the illumination system. In Locations 1, 2 and 3 the energy intensity added was greatest in the center where the measurement was taken. The mass flow rate would be higher in the center as there is more energy to drive the flow in the center than at the sides. On the top horizontal ledge no energy is added and the flow would mix if there was turbulence. The high velocity fluid in the center would go to the sides and the slower velocity fluid at the sides would go to the center. The net result is that the fluid velocity would become more uniform, reducing the overall mass flow rate. So this three dimensional effect would cause the mass flow rate at Location 3, where more energy is added, to be higher than Location 4 where mixing has caused the mass flow rate in the center to be lower. All the calculated mass flow rates are largest at Location 1 and decrease through Location 2, 3 and 4 and are smallest at Location 5. This trend in the results is due to the three dimensional effects of non-uniform heating from the illumination system and mainly due to the losses/ hot air escaping to the ambient from the holes within the system. Thermocouples had to be placed within the TBZ to monitor the temperatures. The experimental setup is not perfectly insulated due to thermocouples coming out of the cavity for temperature readings, which is the main cause of decrease in the mass flow rate in the TBZ.

To give a single value of the calculated mass flow rate for each experiment to represent the mass flow rate for the average centered vertical heat flux applied uniformly in a cavity, the average of the mass flow rates calculated for Locations 2 and 3 was used for calculating the mass flow rate for each

experiment. Only Locations 2 and 3 were used as they were very similar and did not appear to be affected by recirculation.

The variation of the mass flow rate as a function of the B/H aspect ratio is shown in figure 3-28. Following the expected trend, the mass flow rate increased with increasing the aspect ratio. The increase in the mass flow rate for Experiment 4 was quite high, which is because of the recirculation on the south side. It was not possible to find the recirculation zones experimentally because of the velocities being very low. The second line for north side showed how the mass flow rate went down once it crossed 30 cm case. Most of the hot air stayed on the south side and did not make it to the north side of the TBZ.

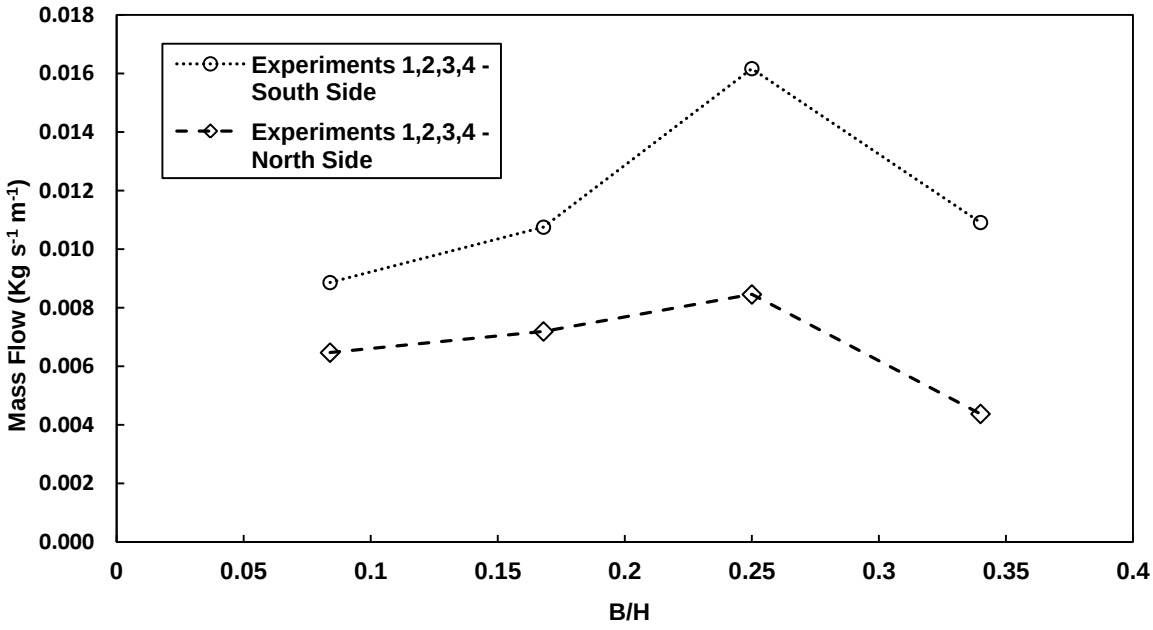


**Figure 3-28 Mass flow rate per m width vs. B/H aspect ratio for each experiment**

The variation in $T_{avg}$ as a function of the B/H aspect ratio is shown in table 3-4. The $T_{avg}$ on location 5 decreases as the B/H aspect ratio goes up. This is because the mass flow goes up as the B/H aspect ratio goes up and there is

more mass to be heated by the nearly constant input energy. In experiment 4, the temperatures in locations 1, 2 and 3 are quite high because of the recirculation.

**Table 3-4 Average temperature ($^{o}$C) at each location for all the experiments**

| Experiment | Location 1 | Location 2 | Location 3 | Location 4 | Location 5 |
|---|---|---|---|---|---|
| 1 | 30.69 | 30.84 | 31.09 | 29.66 | 28.25 |
| 2 | 30.80 | 32.17 | 32.64 | 30.65 | 28.45 |
| 3 | 30.61 | 32.15 | 32.39 | 30.52 | 28.17 |
| 4 | 30.42 | 33.12 | 32.48 | 29.65 | 28.04 |

## 3.2 Effect of Lab Temperature

The initial condition of the experiment will not change whereas the lab temperature/conditions may change. The amount of air in the cavity is changing and so are the byuoncy forces. The heat loss to the lab is continuously varying because of the variance in the temperature of the lab. The amount of heat gained by the air in the gap is dependent on the outside lab condition, therefore in order to achieve accurate results the lab conditions needs to be controlled. The velocity measured which was used to calculate the mass flow rate at one single line does not give solid values. In order to capture the bulk velocity which could be representative of the actual mass flow rate, the velocity needs to be measured at several locations. A graph showing the temperature inside the cube can be seen below in figure 3-29.

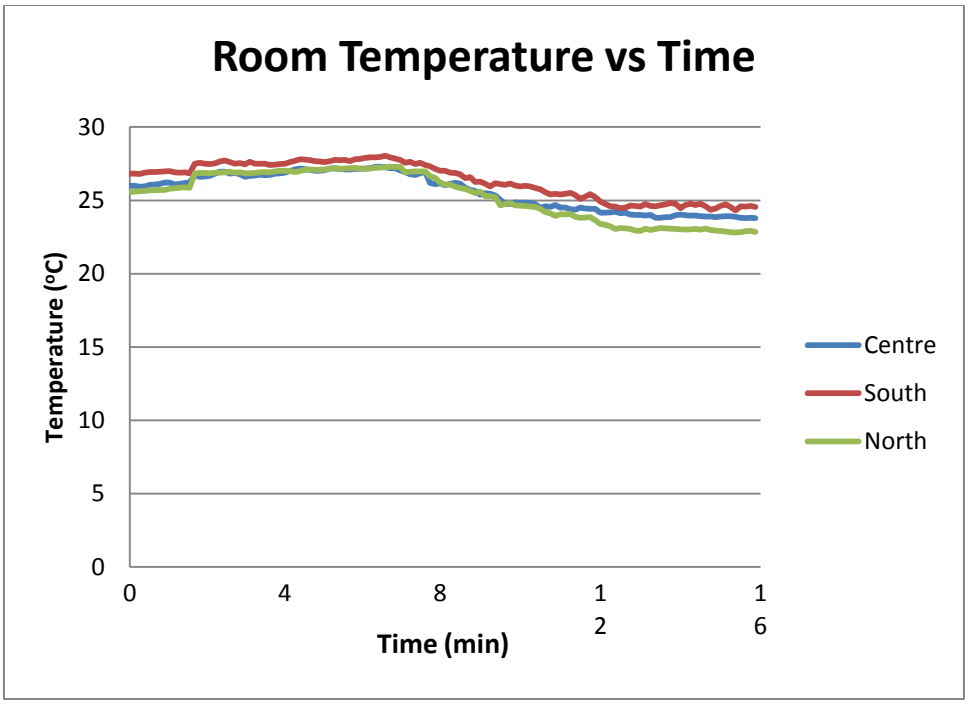


**3-29 Inside space temperature vs. time**

# Chapter 4

# 4. Numerical Investigation

## 4.1 Development of the Numerical Model

The commercial CFD software program of ANSYS CFX was used to develop a two-dimensional numerical model. The main objective for developing numerical model was to assist with the flow pattern/velocity direction in the experimental results. It is imperative to simplify the problem so that a numerical model can be developed. The following section outlines the assumptions made to develop the numerical model. A diagram of the computational domain can be seen in Figure 4-1.

## 4.1 Constant Density Assumption

The Boussinesq approximation was used to model the effect of buoyancy on the momentum equations. The constant properties of air at 25$^{o}$C were used in the fluid model. Using constant air properties and the Boussinesq approximation allows for keeping density constant which was found to cause convergence issues when left as a variable. Given the small change in temperature of the bulk fluid in the experiment, the density variation is small and therefore can be neglected.

## 4.2 Glass and Fluid Domains

Previous numerical researchers have used a single surface to model the glass. However, as mentioned in the literature review, this does not allow to

accurately accounting for the effect of the glass on the heat transfer in the cavity. For the current work, a glass domain is interfaced with the fluid domain. An interface between the two domains is required to conserve the energy exchange between them.

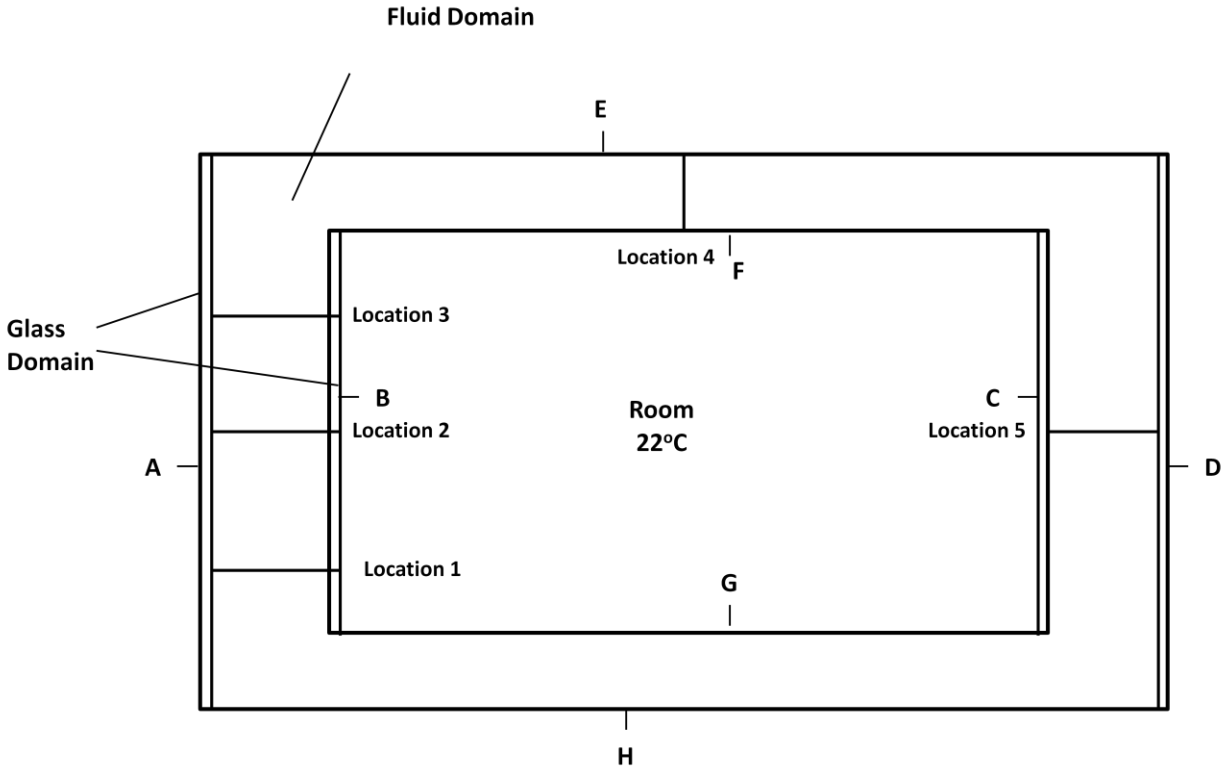


**Figure 4-1: Numerical computational domain with labelling of boundaries and locations of measurements**

## 4.3 The Turbulence Model

The Shear Stress Transport (SST) model developed by Menter (1994) was used. The SST model is known to be a robust model for predicting flow separation and reattachment compared to the standard k-ε model. As with all two equation models the SST model assumes flows are isotropic. Buoyancy is an

anisotropic effect on turbulence. The SST model proved to be an accurate prediction of the flow, as seen by the validation discussed at the end of this chapter.

## 4.4 Geometry

The geometry used in the 10-domain method involved modeling the TBZ along with all the physical walls. A layout of this setup can be seen in Figure 4.2. Dimensions used reflect the new prototype built and will be discussed later in this chapter. The geometry was extruded for 0.0005 m (which is the size of one mesh element) in order to eliminate all 3-dimensional effects and to reduce the computational time of the simulation. All solids were made using the "Add Frozen" option as opposed to the default "Add Material" option.

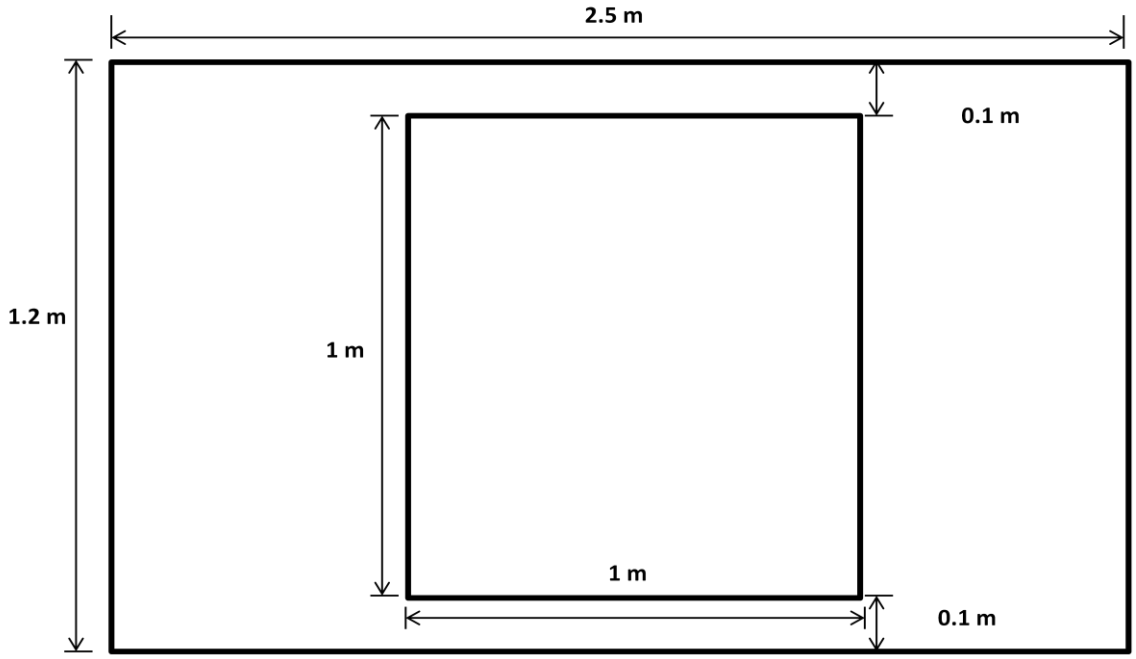


**Figure 4-2: General Dimensions of the Physical domain**

## 4.5 Mesh Settings

The following settings were used to construct the mesh.

**Table 4-1 Mesh Settings**

| | |
|---|---|
| Default Body Spacing | 0.002 m |
| Default Face Spacing | Angular Resolution, 30 degrees, 0.0005 m minimum edge, 0.002 m maximum edge |
| Mesh Options | Delaunay Surface Meshing with Advancing Front Meshing Strategy and Volume Meshing |

Inflation and extrusion were not used in the mesh due to the already miniscule size of elements. The final mesh resulted in 1,250,106 nodes and 49,225,377 elements for the 10 cm case. The nodes and elements would increase as we increase the gap.

## 4.6 Setup

The setup for this simulation involved 10 Solid-Fluid boundaries with the use of default "Glass Plate" and "Wood Board" materials. All other boundaries were set to symmetry except the top and bottom boundaries (E and H, Fig. 4.1) which, for our purposes, were set to be adiabatic as previously mentioned. Energy inputs into the system were made by use of sub-domains with "Specific Source" Energy Sources ($W \cdot m^3$). The values used were obtained from the mathematical model done by undergraduate group by analyzing the radiation input and the amount of flux that will be absorbed by each surface. The per-volume source quantity can be obtained by dividing the flux source by the thickness of the walls. For example,

$$q'' = 135.07\ W \cdot m^{-3}$$

$$q''' = q'' \cdot t^{-1} = 135.07 * 0.006 = 22511\ W \cdot m^{-3}$$

The inner wall source used had a specific energy of 22511 $W \cdot m^{-3}$.

Fluid properties used included: buoyant fluid with standard gravity, shear stress transport turbulence, thermal energy heat transfer and an initial density of 1.196 $kg \cdot m^{-3}$ (air density at 25 °C). All other settings remained at default.

## 4.7 Solver Controls

Solver controls used a timescale factor of 0.1 with the target residual RMS of $10^{-5}$. Solver run used the Double Precision setting as to aid the convergence of buoyancy driven system.

## 4.8 Model Verification

Using the current experiment's data with a vertical centerline average of 380 $W/m^2$ on the outside of the glass and a B/H ratio of 0.1, independence tests were done. The convergence criterion was increased from a minimum root mean squared (RMS) change in velocity from one iteration to the next of $1 \times 10^{-5}$ to $1 \times 10^{-6}$ and there was a difference of less that 1% in the mass flow rate. This gives confidence that a RMS of $1 \times 10^{-5}$ will give results independent of the convergence. A finer mesh with 1,966,544 nodes with the same Y+ value of the first node of 1.5 was compared against the original 1,250,106 nodes case. The difference in mass flow was less than 2%, allowing use of the original mesh with confidence that finer meshes will not change the results. It should be noted that an unstructured mesh was used with 5 inflated layers off all wall surfaces and can be seen in Appendix C.

## 4.9 Boundary Conditions in the Numerical Model

The following boundary conditions were applied in the numerical model to simulate the conditions of the current experimental setup. The top and bottom walls of the fluid domain, boundaries E and H in figure 4-1, were assumed to be perfectly insulated, so that there were no losses from the top and bottom. This assumption is not correct because a value for the heat flux loss is not known. Also, to avoid counter flow of the air if the TBZ were stacked and to bring all the useful heated air to the north side instead of losing the heat to the surroundings. This needs to be investigated in the future, so that accurate values can be used.

To model the incident solar radiation on the second glass, boundary B in figure 4-1, a parabolic equation that best fits the vertical centerline pyranometer readings for behind the glass was used. The pyranometer readings can be found in Appendix B. To introduce heating in the glass domain to account for the absorption of solar radiation of the glass, 16% for the outer glass and 46% for the inner glass multiplied by the average measured heat flux on the vertical centerline on the outside of the glass was used. The thermal conductivity of the glass was set as 0.81 W/(m$^{o}$C).

The outside glass surface, boundary A in figure 4-1, was bounded by a heat transfer coefficient of 5 W/(m$^2$ $^{o}$C) and was selected as this is the natural convection heat transfer coefficient used for flat plate solar collectors in no wind conditions as seen in Duffie and Beckman (1974). The emissivity of the glass, boundary A and B in figure 4-1, as provided by the glass manufacturer was 0.88 and 0.54 respectively.

## 4.10 Comparison between numerical and experimental results

Numerical results were compared with experimental data from the four experimental configurations. A comparison between the numerically predicted and the experimentally found mass flow rate can be seen in Table 4-2. The mass flow was consistently lower for the numerical case than the experimental data in the smaller gap widths. Once the optimum gap width was reaches the results were quite close and the numerical predicted higher mass flow rates. The three dimensional effects of non-uniform heating from the illumination system, the infiltration in the system and other uncertainties could attribute to the difference. One of the major reasons that contribute to the lower mass flow rates is the numerical model includes flow in every direction, which takes into account the flow going in the opposite direction. The numerical model predicted higher temperature which is due to the constant heat flux that was used instead of radiation as the heating source. Due to the time constraint radiation model was not used in the numerical model. Flow pattern and the velocity vector contour can be seen for all four experiments in figure 4-3 to 4-12.

**Table 4-2 Experimental and Numerical mass flow comparison**

| Experiment | Mass Flow Experimental ($Kg\ s^{-1}\ m^{-1}$) | Mass Flow Numerical ($Kg\ s^{-1}\ m^{-1}$) | Difference (%) |
|---|---|---|---|
| 1 | 0.0069 | 0.0039 | 43 |
| 2 | 0.0080 | 0.0042 | 46 |
| 3 | 0.0162 | 0.0178 | 2 |
| 4 | 0.0075 | 0.0089 | 2 |

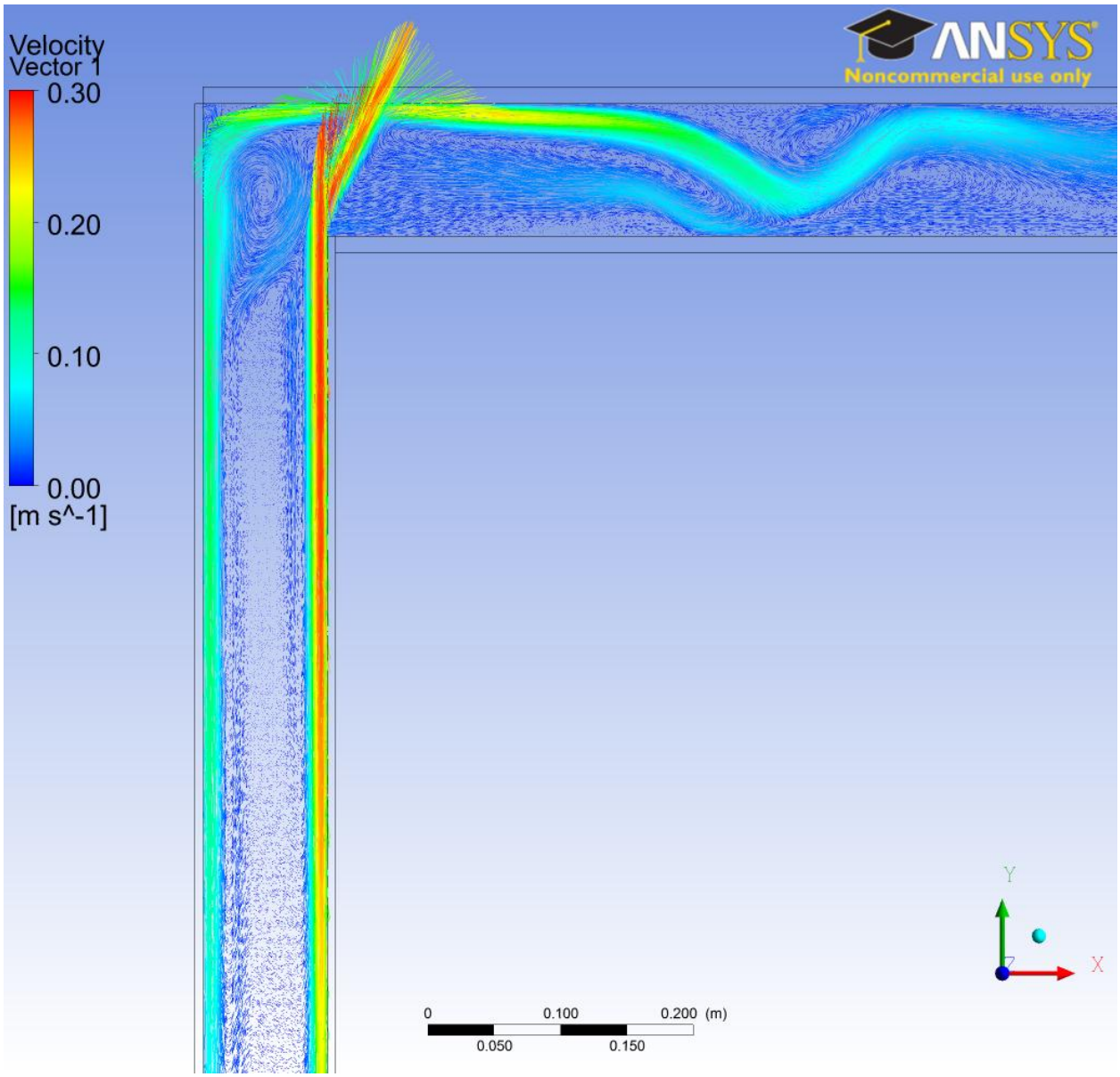


**Figure 4-3: Numerical velocity vectors for Experiment 1, B/H = 0.089**

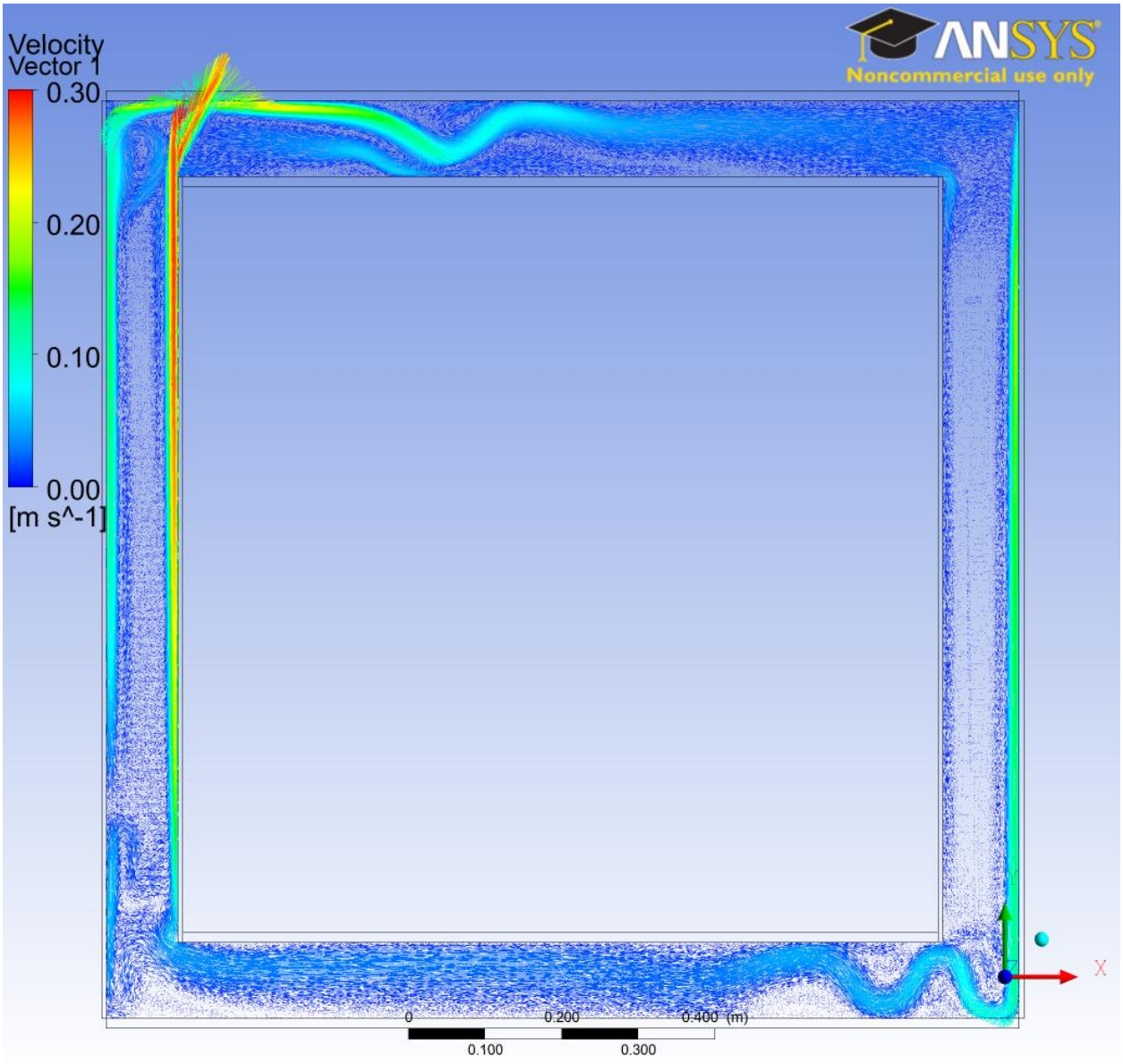


**Figure 4-4: Numerical velocity vectors for Experiment 1, B/H = 0.089**

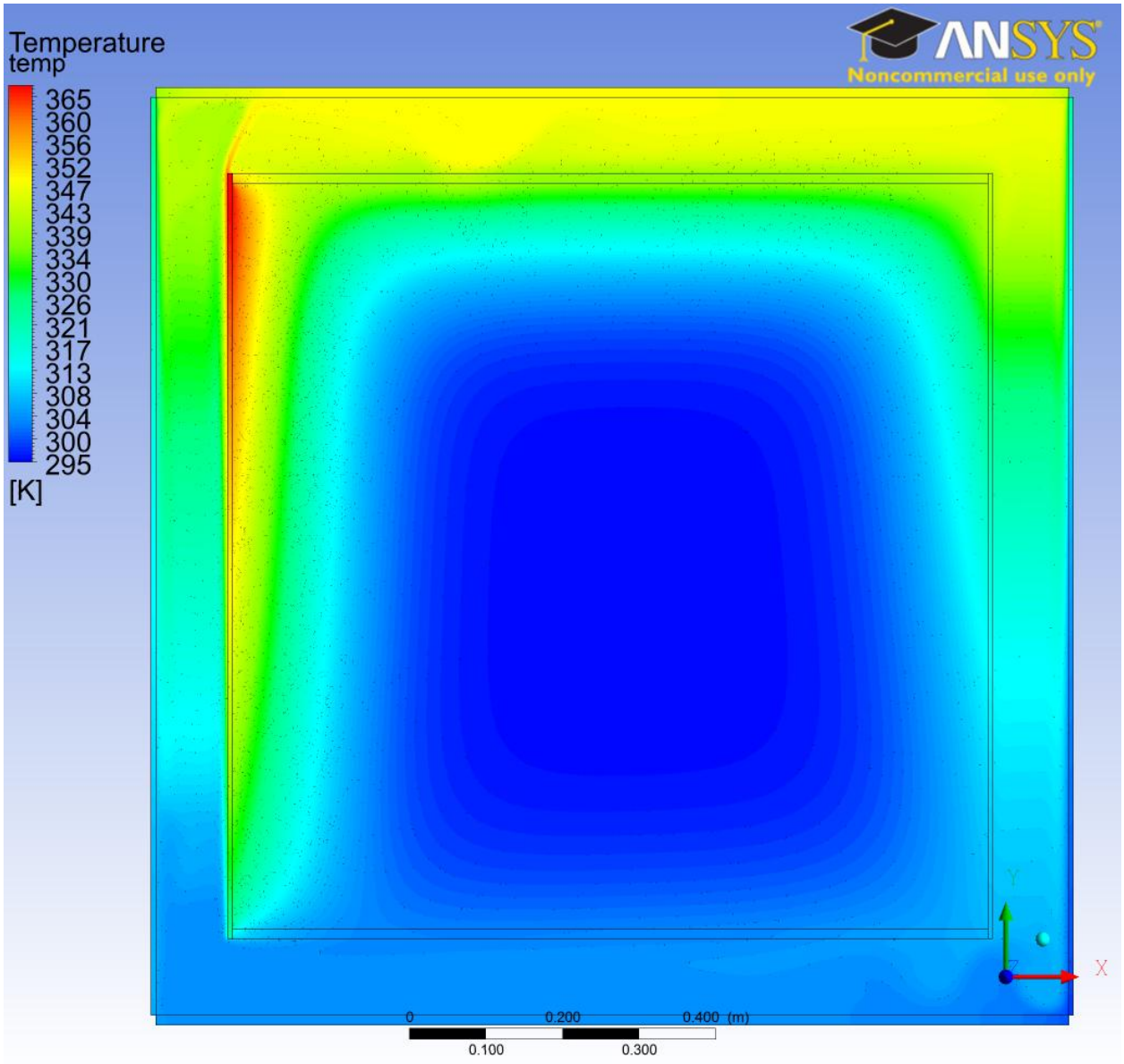


**Figure 4-5: Numerical temperature contour for Experiment 1, B/H = 0.089**

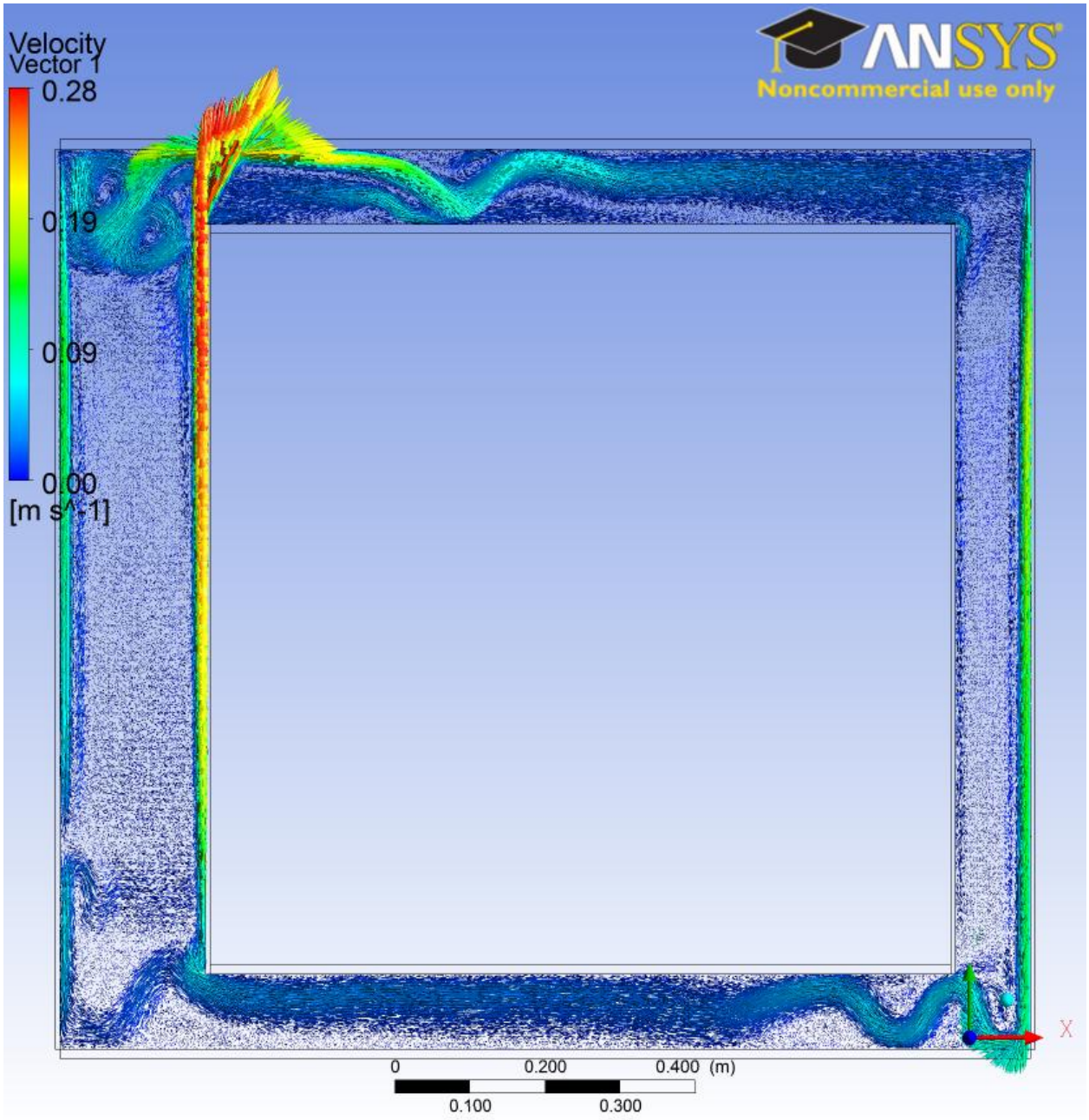


**Figure 4-6: Numerical velocity vectors for Experiment 2, B/H = 0.167**

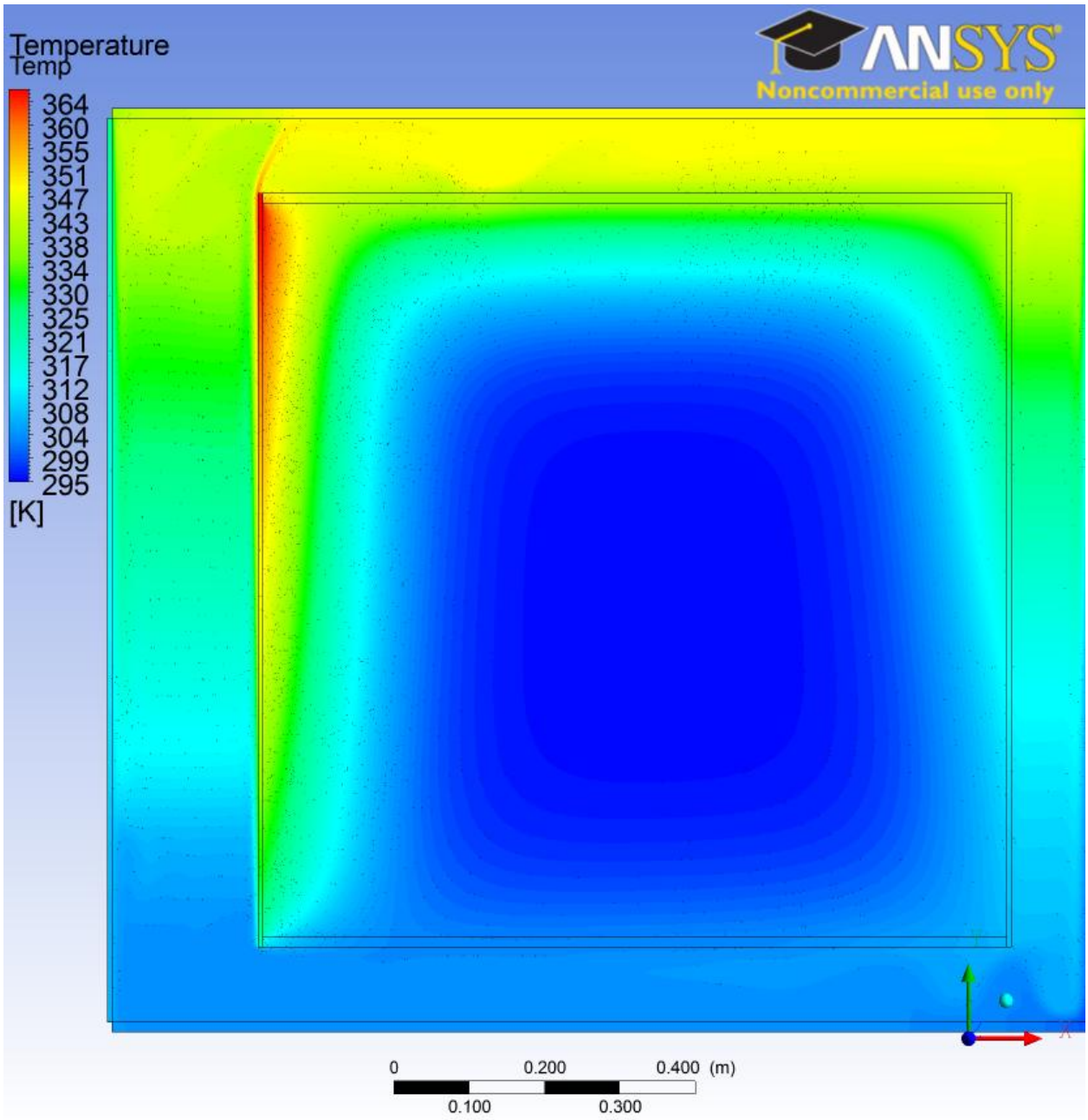


**Figure 4-7: Numerical temperature contour for Experiment 2, B/H = 0.167**

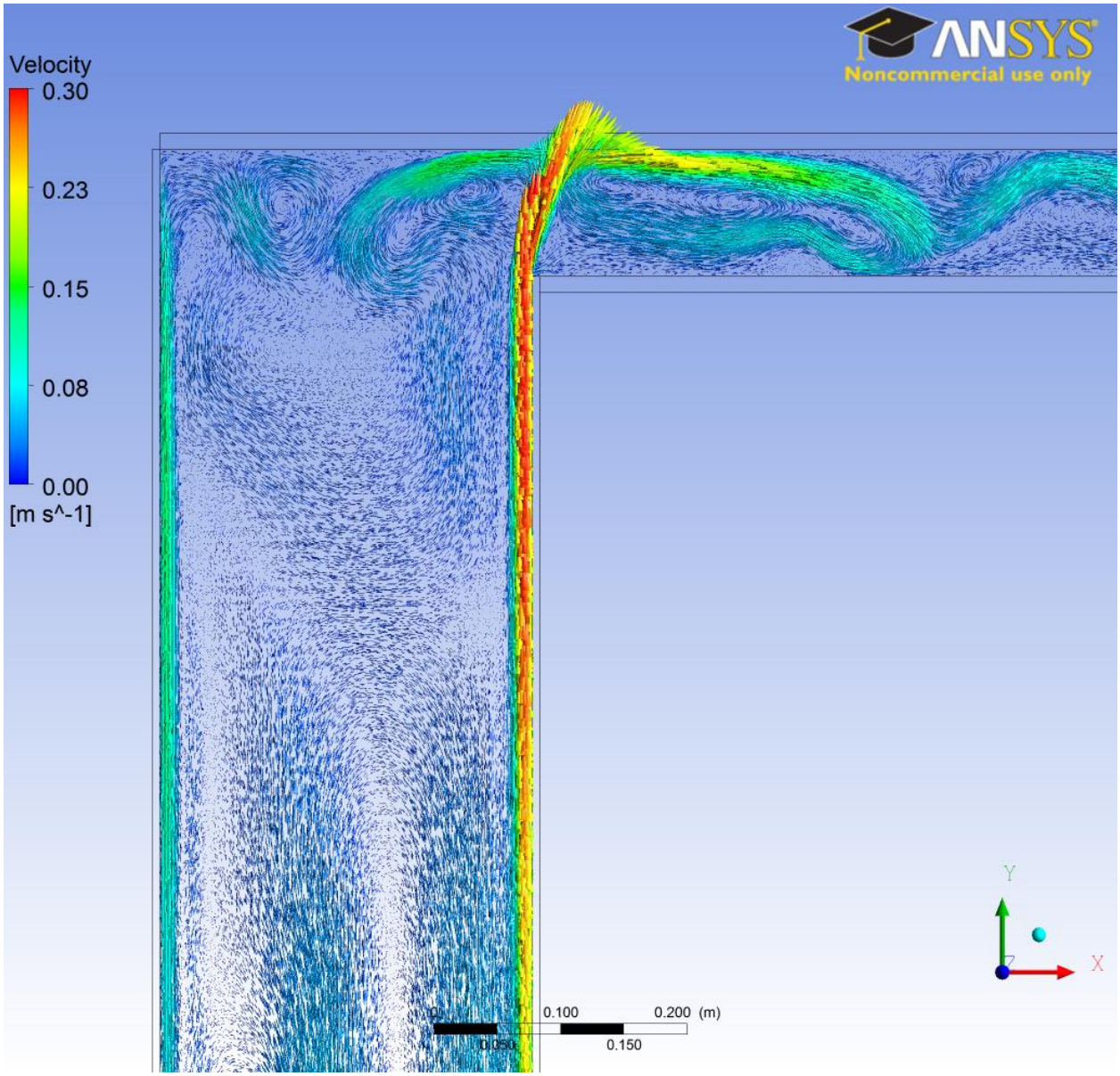


**Figure 4-8: Numerical velocity vectors for Experiment 3, B/H = 0.25**

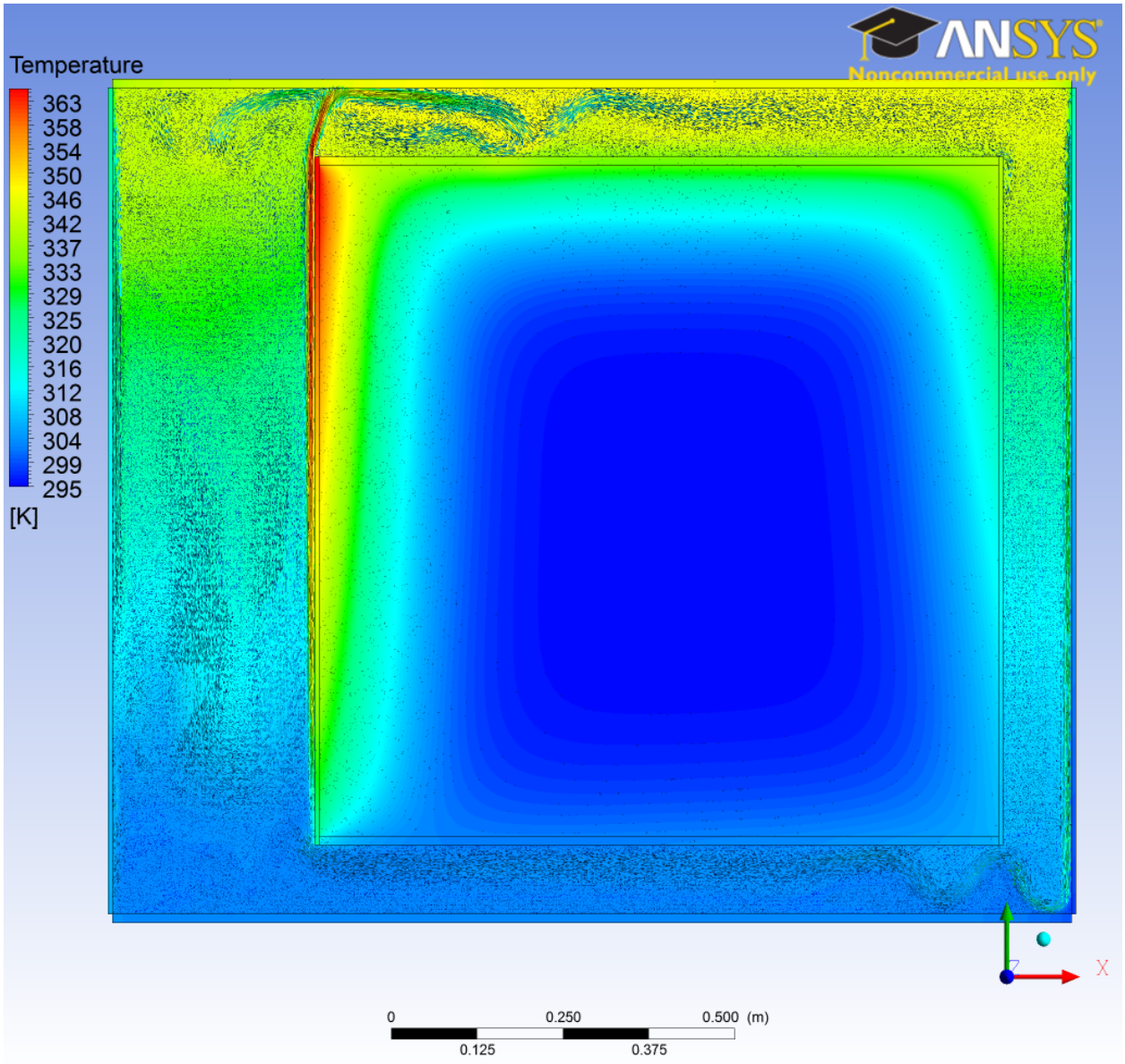


**Figure 4-9: Numerical temperature contour for Experiment 3, B/H = 0.25**

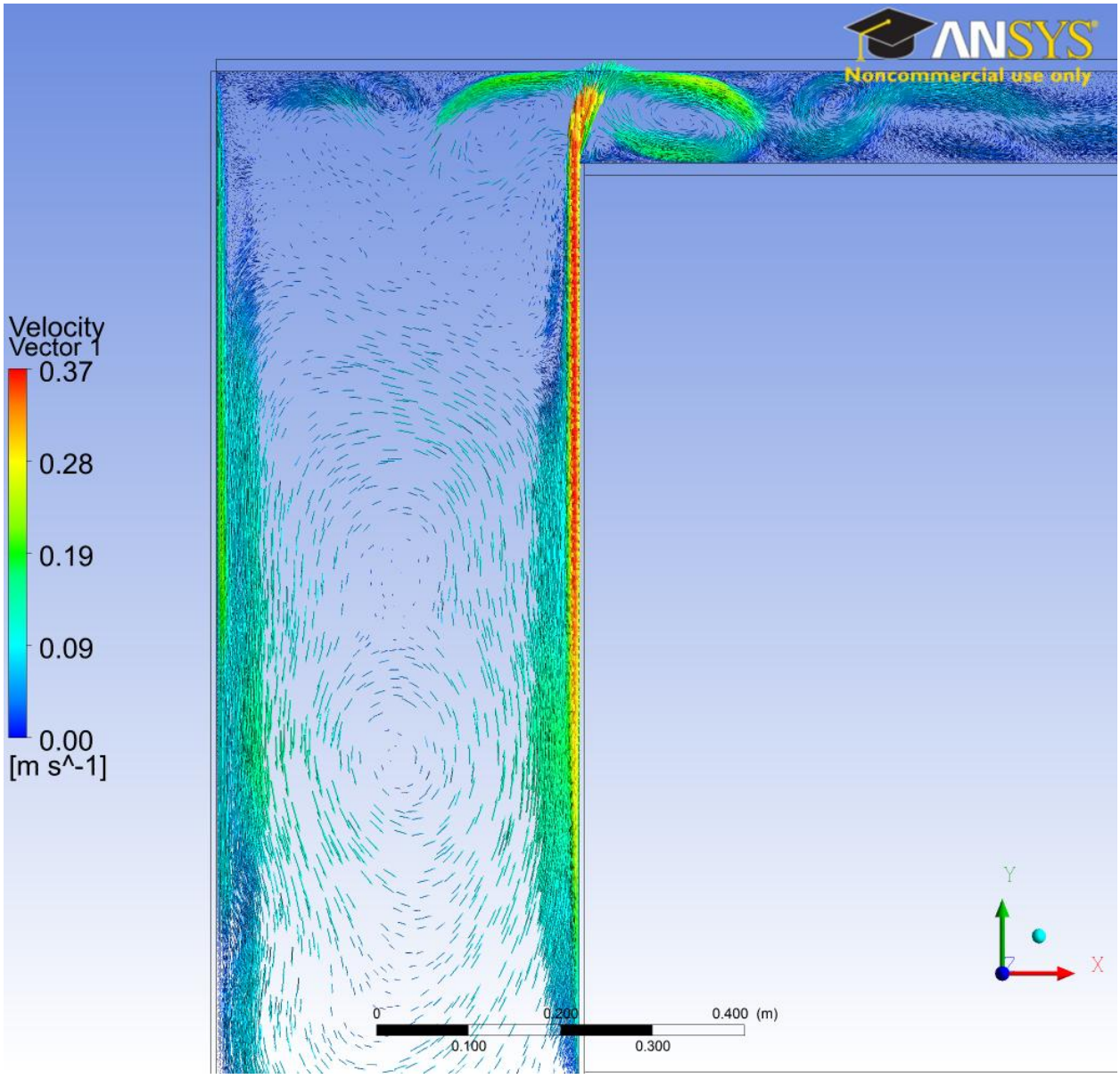


**Figure 4-10: Numerical velocity vectors for Experiment 4, B/H = 0.34**

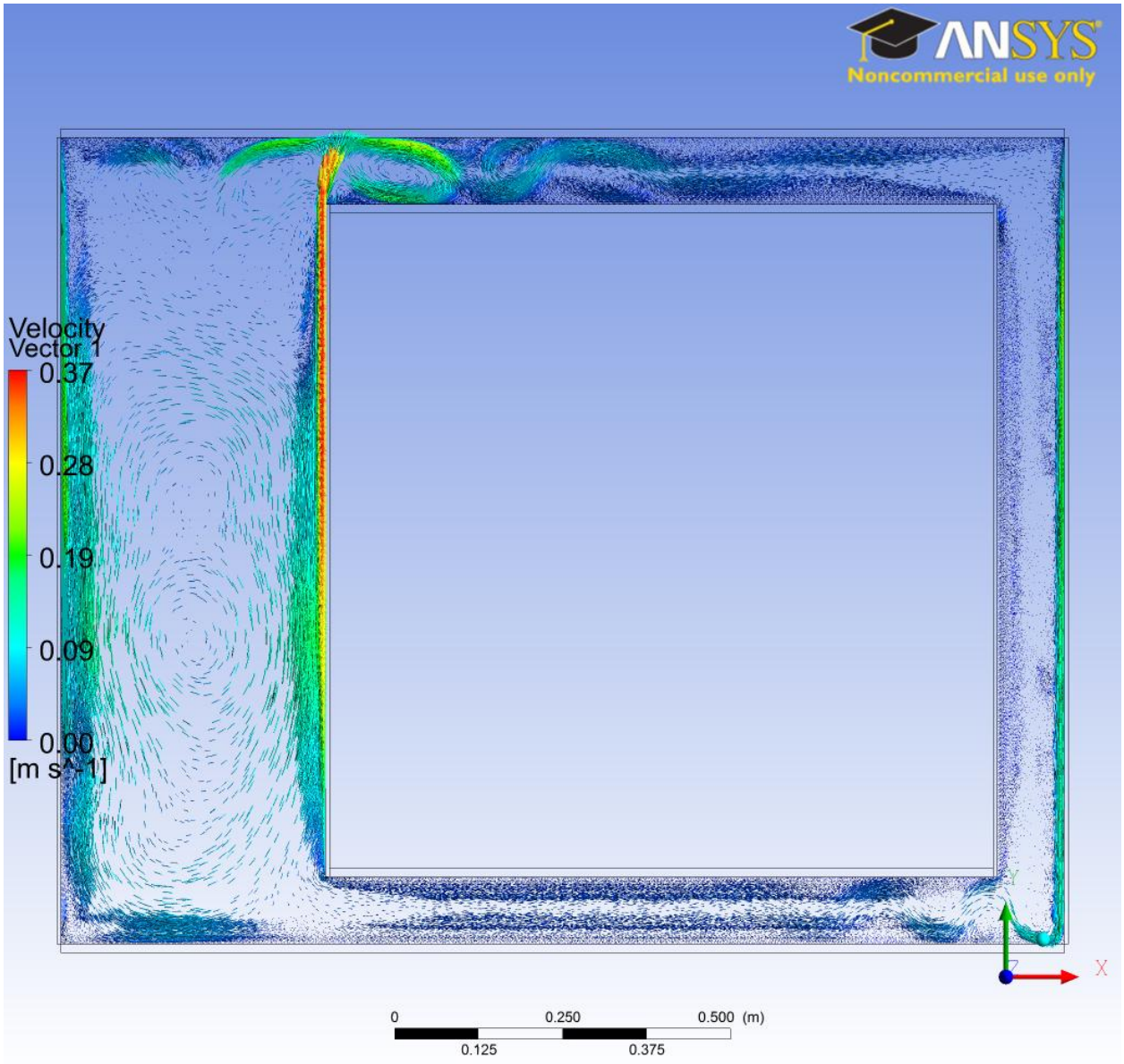


**Figure 4-11: Numerical velocity vectors for Experiment 4, B/H = 0.34**

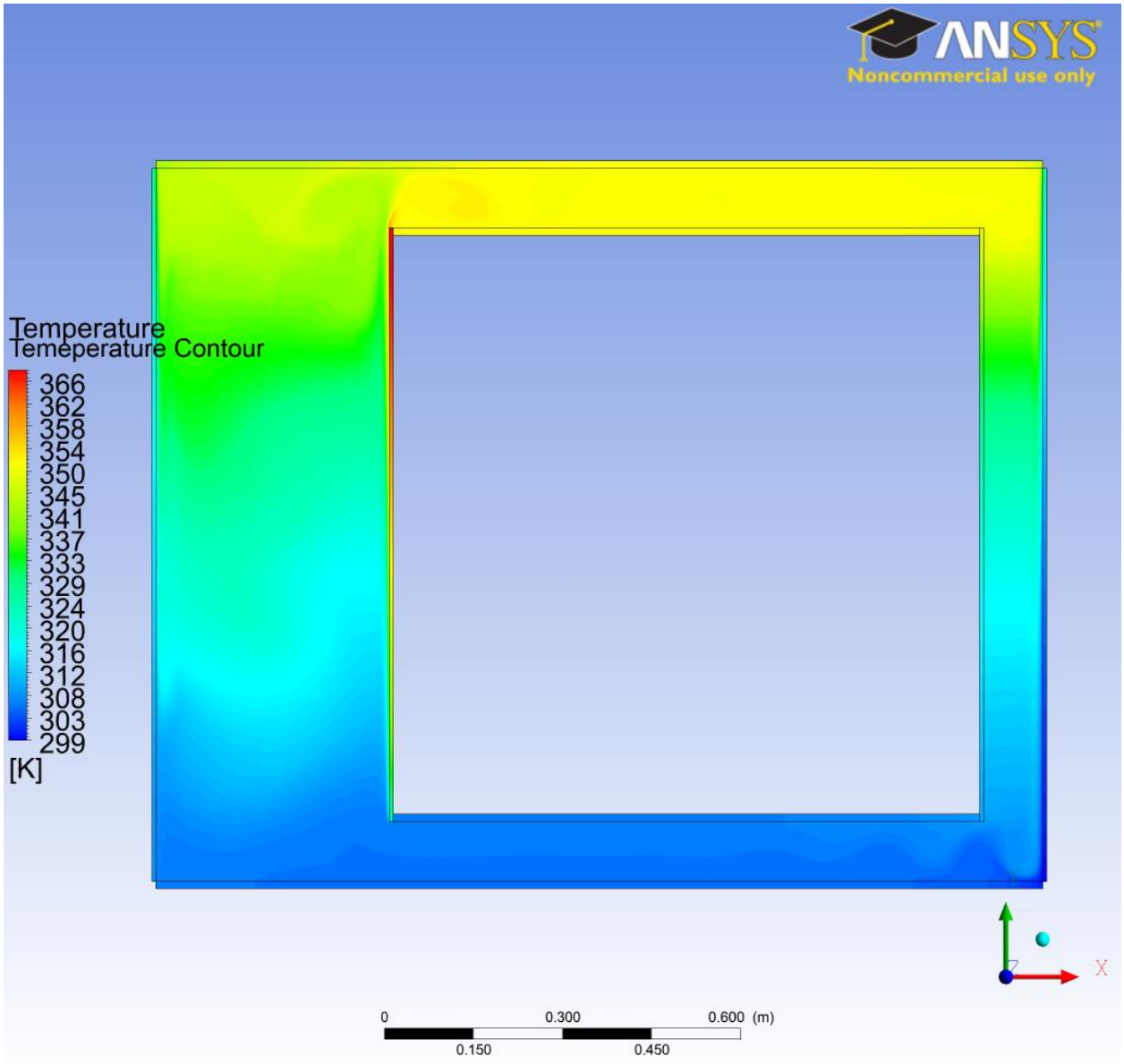


**Figure 4-12: Numerical temperature contour for Experiment 4, B/H = 0.34**

The mass flow rate can be compared between the numerical and experimental models. The average temperatures were also collected at the five locations with the hope to assist in comparing with the numerical model. The numerical and experimental trends are very close; however the numerical temperatures are relatively higher, well beyond the experimental uncertainty.

**Table 4-3 Experimental and numerical temperature difference comparison**

| Experiment | Experimental ($^oC$) | Numerical ($^oC$) | Difference (%) |
|---|---|---|---|
| | $T_{in}$ - location 1 | | |
| 1 | 30.7 | 34.0 | 10 |
| 2 | 30.8 | 33.5 | 8 |
| 3 | 31.6 | 33.2 | 5 |
| 4 | 30.4 | 32.0 | 5 |
| | $T_{out}$ - location 5 | | |
| 1 | 28.3 | 34.8 | 19 |
| 2 | 27.0 | 34.6 | 22 |
| 3 | 28.2 | 33.5 | 16 |
| 4 | 28.8 | 33.0 | 13 |

There are a few possible reasons for the numerically predicted temperatures being higher than those of the experiment. The assumed natural convection heat transfer coefficient on the outside of the glass may be too low for what happens in the experiment, resulting in lower temperatures in the glass. The assumption of the solar radiation energy absorbed in the glass may be too high. The heat transfer for the inner glass left for CFD to figure out in the numerical case, when in the experimental there would have been more heat transfer through the glass, resulting in a lower temperature during experiment. The numerical model may be calculating too low a heat transfer coefficient

compared to the real case. Given the large number of possible reasons for the temperature difference between the numerical and experimental models, it is obvious that more numerical investigation is required to verify the temperature difference.

To improve the confidence in the numerical model, another parameter was examined after the mass flow rates of the numerical and the experimental data were matched. The temperature difference between the numerical mass flow averaged inlet temperature being the location 1 (south side) and the imposed numerical temperature at the exit, which is the location 5 (north side), is compared with the experimental mass flow averaged inlet and exit temperatures in 4-5.

It has been shown that the numerical model is somewhat capable of predicting the major outputs of interest for TBZ operation, mainly mass flow rate and temperatures in the system. It was able to show the recirculation zones which was experimentally not possible due to such low velocities. However, given that there are still unknown values in the experiment that were assumed in the numerical set-up, and that the numerical simulations have a large temperature discrepancy due a constant heat flux used. As such more work is required to improve confidence in validation of the numerical model.

### *4.10.1. Effect of Bends on the Numerical Results*

To quantify the pressure drop due to the flow turning at the 4 bends in the current setup, the current setup was compared with a simple parallel plate configuration. An average heat flux of 380 $W/m^2$ was applied to one wall of the

parallel plate cavity. This is the same average heat flux that was applied in the numerical setup for Experiments 1, 2, and 3. All the boundary conditions were the same between the parallel plate case and the TBZ including the glass domain volumetric heating and heat conduction. The same constant heat flux was used in both numerical cases. The only difference was height of parallel plate cavity and the location of the inlet and outlet. The height of the parallel plate cavity was 1.0 m which is the same height where energy is added on the inside glass. The height of the TBZ setup is 1.2 m due to the TBZ cavity for the bottom and the top. The only effect on the mass flow rate through the cavity between the two configurations should then be the pressured drop added by the flow bending around the inlet and outlet in the TBZ.

A comparison between the numerical results can be seen in Figure 4.13. The numerically calculated mass flow rate for the parallel plate configuration is predicted to be considerably higher than the results for the numerically calculated for TBZ. This difference is likely to be due to the added pressure drop in the TBZ from the flow having to turn around the inlet and outlet and the recirculation induced by these bends. Also the mass flow rate for the parallel plate configuration is numerically predicted to increase with higher B/H aspect ratio. The numerically predicted mass flow rate for the TBZ changes slightly with the B/H aspect ratio for this range as well. The fourth experiment was not included because of huge recirculation zones on the south side. This numerical comparison shows that there is likely a large increase in pressured drop due to the bends in the TBZ over the parallel plate configuration, and this pressure drop increases proportionally with increasing B/H aspect ratio.

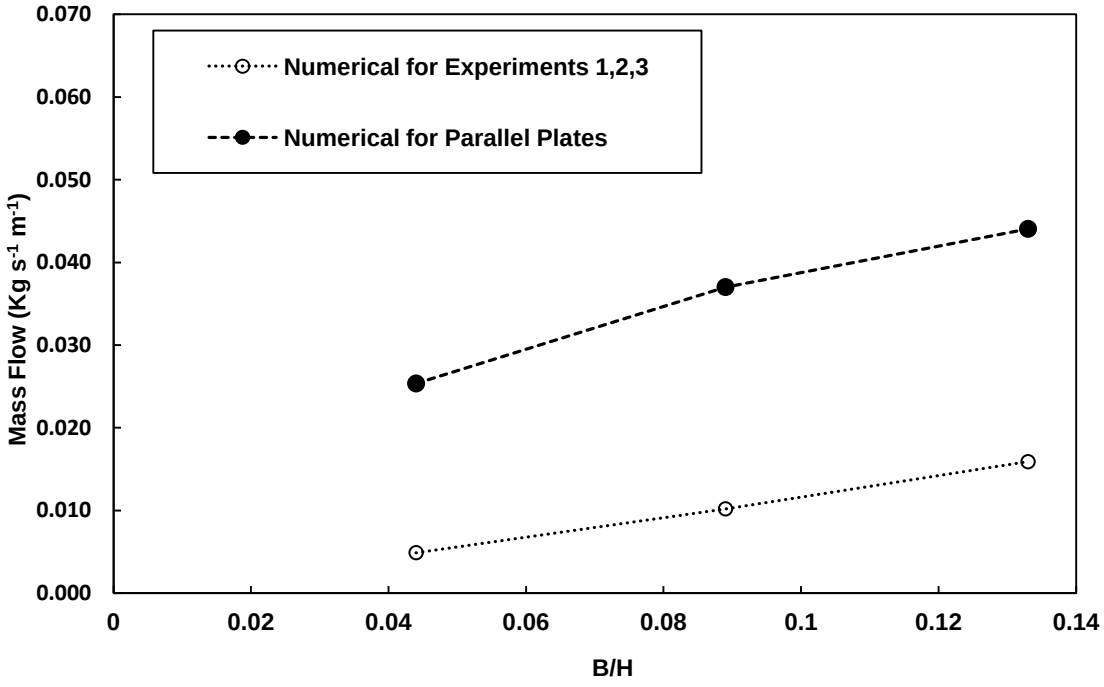


**Figure 4-13: Numerical mass flow rate comparison between parallel plate cavity and the TBZ for the same boundary conditions for Experiments 1, 2 and 3.**

# Chapter 5

# 5. Effectiveness of the Thermal Buffer Zone

## 5.1 Case Study

In order to give an idea of what the experimental and numerical results represent in a real world situation, a case study was developed. Two offices were used; one on the south side of the building floor and one on the north side, see Fig. 5.1. A square room, having an area of 1 square meter was chosen to show how much cooling/heating would be required by each office. The data used were obtained from the experimental results and the optical properties from the 2009 ASHARE handbook.

The representative day for the case study was chosen to be in January. As per ASHARE Fundamentals Handbook (2009), the average temperature in Ottawa in the month of January is 0 $^{o}$C. Assuming no humidity, the conditioned space at 21 $^{o}$C, and an average daily heat flux of 380 W/m$^{2}$ was applied. In order to show the benefits of the TBZ, it has to be compared to conventional building without a TBZ. For a building with no TBZ, all the calculations were based on optical properties obtained from the 2009 ASHRAE handbook.

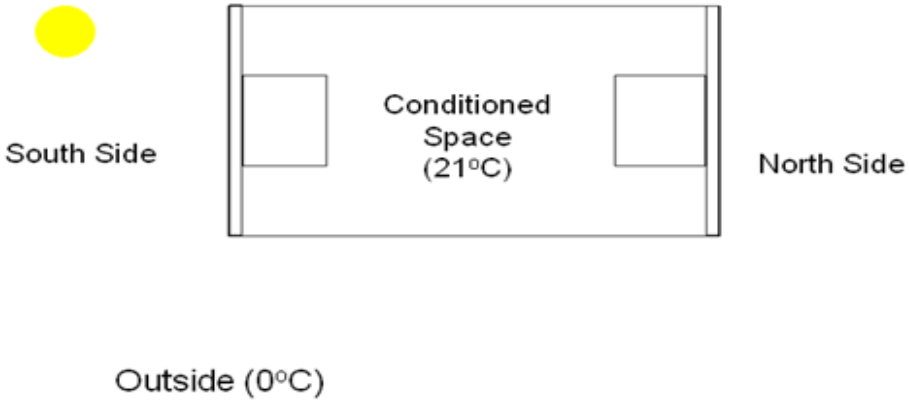


**Figure 5-1: A floor in a building with offices on South and North side**

The average daily heat flux on a perfectly clear day was 380 W/m$^2$ on the outside of the glass. An optimum B/H aspect ratio of 0.3m found experimentally was chosen for this case study. Table 5.1 shows the benefit of TBZ within a building. Having a TBZ saves over 70% of cooling on the south side and similarly on the north side of the building, TBZ can save up to 31% of extra heating required to keep the inside space at a comfortable temperature. Detailed calculations are included in Appendix E.

**Table 5-1 TBZ vs No TBZ, average daily heat flux of 380 W/m$^2$**

| | NO TBZ | TBZ |
|---|---|---|
| **South Side** | | |
| | Cooling (W/m$^2$) | Cooling (W/m$^2$) |
| Single glazing | 203 | 46 |
| Double glazing | 195 | 42 |
| Double glazing, low e coating | 184 | |
| Triple glazing | 204 | |
| Triple glazing, low e coating | 184 | |
| **North Side** | | |
| | Heating (W/m$^2$) | Heating (W/m$^2$) |
| Single glazing | 105 | 72 |
| Double glazing | 72 | 54 |
| Double glazing, low e coating | 63 | |
| Triple glazing | 55 | |
| Triple glazing, low e coating | 44 | |

The case study shows that the TBZ does have the potential to offset the heating and cooling load when the conditions used for deriving this case study are met. However, during other seasons, the TBZ will perform more efficiently by creating an exhaust air duct where the heated air can be dumped when not needed. Further research needs to be done to verify the above statement.

## 5.2 Practical Operation of the TBZ

One of the issues could be the possibility of slight overheating of the areas close to the thermal envelope on the south side which defeats the purpose of providing comfortable temperature for occupants. The cavity temperature rise due to stagnation can be reduced by shading the window from the outside, which

will reduce the heat flux and the glare coming into the conditioned space. The outer shading is most beneficial in winter and summer from an energy standpoint.

Since it is not always sunny, the potential/benefits of the TBZ decrease when averaged over a month's period. Since cloudy days only allow diffuse radiation to fall in the TBZ, after considering the number of cloudy days in Ottawa, the cooling/heating requirement would be the same as a conventional building. Another case scenario to look at in the future work would be the performance of TBZ at night time when the sunlight is not there.

TBZ still provides significant thermal energy which is of value and there are no concerns about external pressure forces causing loss of conditioned air. There is also no need for complex control systems. The thermal energy from the TBZ would be used to replace the heat lost by conduction through the walls. The case study and the discussion that followed have shown that the benefit of the TBZ is quite significant; however, a year round simulation needs to be carried to accurately predict the annual performance of the Solar Thermal Buffer Zone. To address the change in pressure which is caused by natural convention or byuoncy force, if the change in pressure is sufficient or not to drive the flow across the horizontal length or a booster fan will be needed. In theory the longer the width of the building the more will be the pressure drop. For the experimental model the bend effects are much more significant compared to the losses in the top and bottom. The model is not representative of the actual building when it comes to the width, the major and minor losses are switched when the width is increased and also depending on what kind of a pathway is provided.

In order to get the heated air from south side to the north side, hollow core slabs can be used as shown in Fig. 5.2 below. Hollow core slabs will be already made in the floor; therefore there would be no need for separate system to be installed. There is also a possibility of thermal storage in the concrete, to take advantage of heating for a certain time when the sun is set.

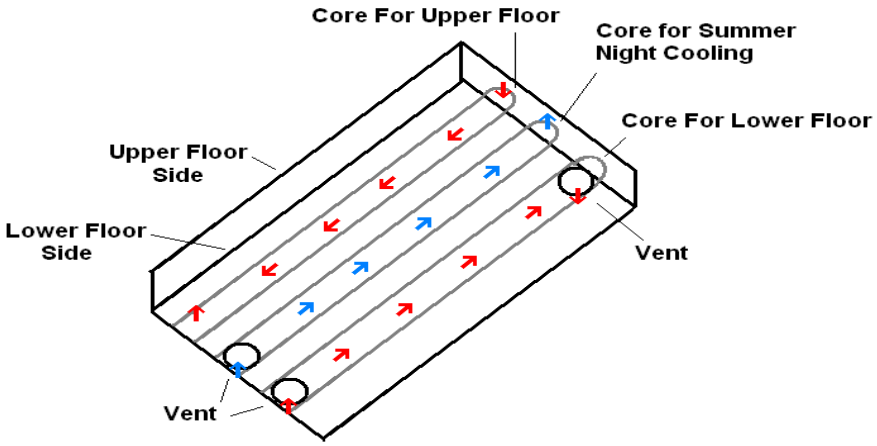


**Figure 5-2: Hollow Core Slabs**

## 5.3 The usage of the TBZ in the Summer

The performance of Solar Thermal Buffer Zone in winter was quite significant which takes us to look at its performance in i.e summer, the other extreme. Since we don't want any heat coming inside the conditioned space in summer, it needs to be put back in the atmosphere. The heated air will rise and exit into the atmosphere by an opening in the roof. Automatic valves are used which will close in the cavity in the roof and instead let the air rise up to the top and exit into the atmosphere. To prevent overheating, automatic blinds will also be used during the summer/the cooling season.

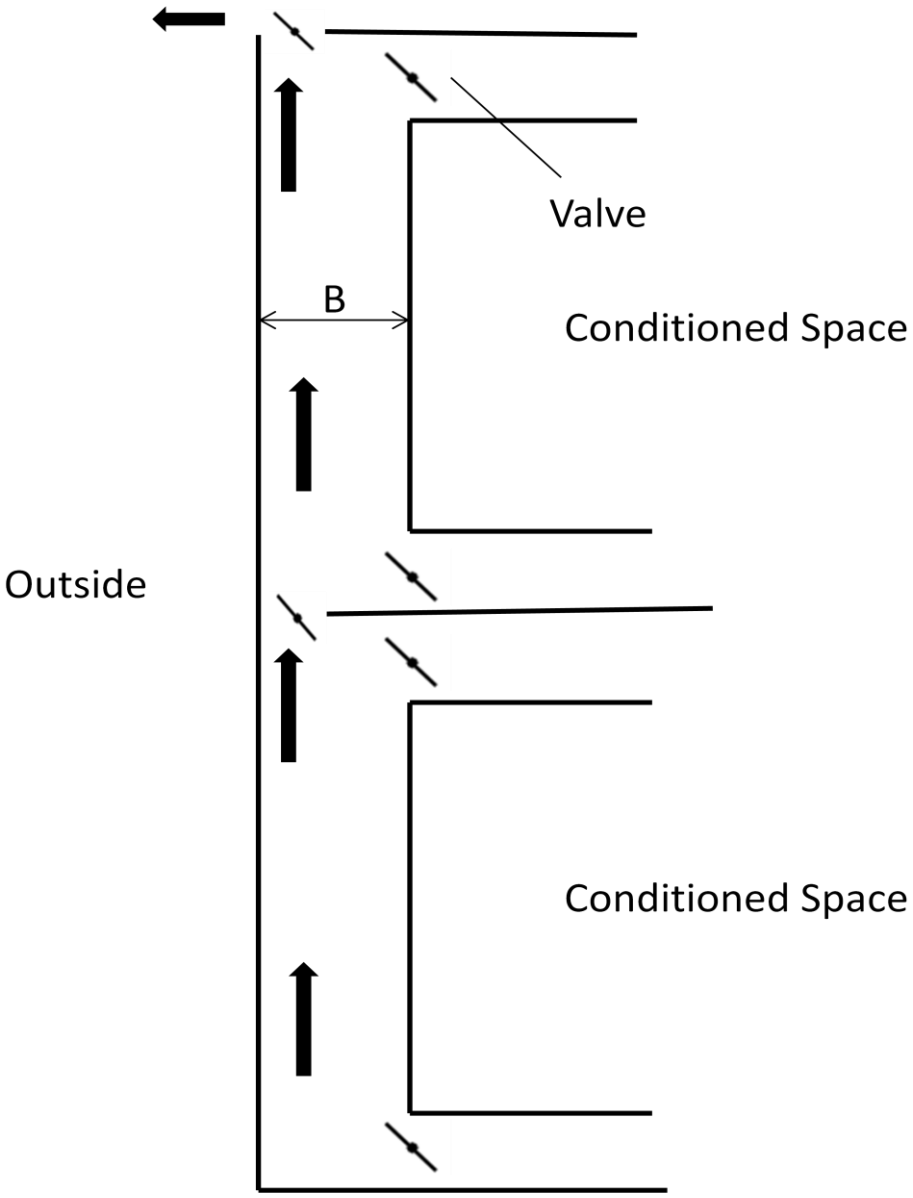


**Figure 5-3: TBZ in summer**

# Chapter 6

# 6. Summary and Conclusions

## 6.1 Summary of the Research Work

An investigation of the benefits of using TBZ in buildings has been carried out. From the literature review, it was found that there were no comprehensive correlations accounting for the various parameters that affect the performance of TBZ. These correlations are needed for performing a year round building energy simulation that would calculate the benefits of TBZ round the year. It was then decided that a CFD parametric study would be undertaken to assist with the experimental results. A numerical model was developed with the ANSYS CFD software package. To have confidence in the CFD numerical model, it was compared with results from a new comprehensive experiment. The experiment included radiation as the heat source, a feature which was used only once in experiments investigating solar thermosiphons by a previous graduate student. The testing apparatus allowed for adjusting geometrical parameters such as the spacing between the two glasses of both sides, and also changing the radiation intensity. However, for this project only the south side gap/ spacing was changed. These parameters have been noted by previous experimental researchers to have an effect on the performance of any solar thermosiphons.

Four configurations were tested with the experimental apparatus. The average outside of the glass vertical center line radiation intensity was 380 $W/m^2$ with four gap widths of 0.1m, 0.2m, 0.3m and 0.4m.

The numerical model was developed to include effects such as thermal radiation heat transfer in the cavity, glass conduction and volumetric heating all of which have not been included in previous numerical models. The inputs from the experimental setup were used in the numerical model so that it could predict and help with the experimental results. Some inputs into the numerical model had to be assumed as they were not measured in the experiment. However, the numerical model did not predict that the mass flow rate was dependant on the B/H aspect ratio whereas all the experimental work, including the current experimental work, has shown this dependence. Therefore, more work needs to be done before the numerical model can be validated and then used to generate correlations.

The experimental results were used in a case study for an office building located in Ottawa for the month of January. This case study showed the potential of a TBZ under optimal operating conditions. A discussion was done on the performance of TBZ in non-optimal operating conditions. TBZ still showed to be beneficial by making use of the solar energy when available.

Implementing this research also improves the thermal resistance of the building envelope. The research will provide building designers with the optimal configurations for a given climate along with the performance of the system under different environmental conditions. This will allow the designers to predict how other components in the HVAC system will interact, so that they may properly size all the components. The research will also provide data on when these methods are not effective, indicating the need for other methods of ventilation and heating. Given the initial cost of implementing these methods, it is

more likely that they will be applied to new building design/construction; however, these systems can also be used in some retrofit cases.

To decrease the sun glare, one can use the Double-Glazed High-Solar-Gain Low-E Glass. Another option would be to use the second glass a translucent one where only light can go through but not the glare. This option has been used at some places in the Engineering Technology Building at McMaster University. TBZ allows solar gain from the whole south side instead of just spandrel areas (**3 times** the potential just due to larger surface area). It is fully integrated with the building, and does not need to rely on the HVAC system for mixing like SAWs do. TBZ provides heating even when ventilation is not needed (unlike the supply mode or an active transpired system like SolarWall which always has to provide ventilation). Basically it is a better version of the indoor air curtain.

# Chapter 7

# 7. Recommendations and Future Work

The main objective of this project was to achieve Net Zero Energy Buildings. This study showed significant savings only by having a TBZ in a building. The benefit that came out of this research is the development of a properly calibrated passive method for the heating of a building in order to maintain the inside space at a comfortable temperature. The methods to be researched should provide a means of utilizing the renewable resource of solar energy such that, by means of natural heating, the use of external energy sources is reduced, and a net zero energy building is achieved. Therefore, future research should stay focused on reducing the use of fossil fuels in the buildings.

Considering mechanical ventilation, the energy required to heat air is far greater than the energy required to pump it into the building. Most energy used to pump air in a mechanical ventilation system is to provide recirculation of air throughout the building through all the duct work, rather than to draw air in from the outside.

This seems quite trivial at the outset, as more insulation would reduce losses from the building. However, for almost any level of insulation used, the most important aspects of the system while making use of solar energy are the optical properties of glass. Optical properties have been studied in great detail in standard flat plate solar thermal collectors and the findings in this field would be directly applicable to the current study of solar thermal buffer zone. Having dealt

with conductive and radiation losses, all that is left is convection losses on the inside of the cavity as the outside surface is exposed to the weather, and is beyond the control of the designer. From the current work and other studies, changing the spacing between both the glasses had little effect on the thermal efficiency. Hence, from a thermal efficiency point of view, the effects of changing different parameters have all been researched and found. Quantifying the exact thermal efficiency for a given set of parameters is yet to be done. The summation of this would be a multivariate analysis of all the important parameters leading to correlations for the implementation in year round building energy simulation.

The TBZ is capable of offsetting more external energy used in buildings than any other solar thermosiphon. It is much easier to implement in a practical sense and research of it is much simpler as there is essentially no pressure difference between the inlet and outlet like it is in the case of SAW. The only factor that would not be accounted for with the current equipment, when performing experiments with the TBZ, would be the outside temperature cooling the glass.

Constructing a test facility to study the TBZ with different inside and outside temperatures and different pressure differentials applied would be more useful and applicable, which could be used in the shoulder seasons of spring and fall. It is almost as important to study the performance of TBZ at optimal operating conditions as it is at non-optimal operating conditions such as night time and summer time. This is because the increase in energy load during these non-optimal times could outweigh the energy saved in optimal operation conditions. Correlations for the performance during the non-optimal operation

conditions are required in a year round energy simulation, to fully account for the impact on the total energy used due to implementation of TBZ.

It is clear by now that, to have a larger reduction in external energy used, more experiments are needed in different conditions, so that the savings at one time of the year are not offset by losses at another time of the year. TBZ in the winter time is good to add thermal energy to the building passively, but it's important to look at the operation of the TBZ in summer to prevent excess thermal energy that comes into the building which would increase the cooling load. As noted before, the time to perform one numerical simulation is much shorter than performing an actual experiment. The current testing equipment that was used to get all the temperatures and velocity profiles, took at least ten times longer than running a numerical simulation. However, the numerical model could benefit from more experimental data/results to improve the validation.

The current numerical model does not encompass solar radiations, and hence the change in optical properties with changing glazing is not accounted for. Experimental tests should be carried out with different window panes to obtain the effect of the change of the optical properties, which was not accounted for by the current numerical model. Keeping the inside at constant temperature is also important as this had more influence on the heat losses and mass flow rate than any other parameter. In order to validate the numerical model for the performance of TBZ at lower outdoor temperatures, only a couple of tests would need to be carried out.

# 8. Appendices

## 8.1 Appendix A - Velocity Measurement Conversion

The conversion from voltage to velocity is based on the Log Square transfer function. *Eq. 8-1*

$$LSQ = \ln^2(1 + gV)$$

Where $g$ is the gain factor optimized for a specific probe type. For the omnidirecitonal probe, $g$ is set as 150.

*Eq. 8-2*

$$LSQ = A_0 + A_1 e + A_2 e^2 + A_3 e^3 + ..$$

Where $A$ values are found from the manufacturer provided calibration, and $e$ is the measured voltage. The resulting equation can then be written.

*Eq. 8-3*

$$V_e = \left[exp\left((A_0 + A_1 e + A_2 e^2 + A_3 e^3 + ..)^{1/2}\right)\right]/g$$

The pressure is then accounted for by the following.

*Eq. 8-4*

$$V_p = V \frac{p}{101.325\ kPa}$$

Where $p$ is the measured atmospheric pressure. The correction for humidity and temperature is finally applied.

*Eq. 8-5*

$$V = V_p \left(1 + f\left(r \times f(T)\right)\right)$$

Where $f$ is a manufacturer provided calibration function for the respective values, $r$ is the relative humidity and $T$ is the measured temperature. This will result in an instantaneous velocity reading. To account for the turbulent nature of the flow many in instantaneous voltage readings need to be taken, and converted to velocity, then averaged to get a mean velocity reading at that location.

## 8.2 Appendix B - Pyranometer Readings

The following shows the pyranometer readings with the coordinates zero and zero referring to the location centered between the vertical height and horizontal width between the four bulbs. Two set ups, seen in Figure 8.1 and 8.2, had a smaller spacing between measurements used for the horizontal center line readings to see if there was variations from the courser gird. Figure 8.2 shows the decrease in the measured heat flux due to the shading caused by the thermocouple wire used to measure the surface temperature of the glass. This shows that there could be differences between what is measured in the courser grid and the actual heat flux on the surface. The occasional reading for the behind glass measurements that is well below the rest of the readings is attributed to shading from the thermocouple wire.

**Table 8-1 Pyranometer readings (W/m$^2$) on outside of glass for L = 1.38 m**

| Spacing (in) | 14 | 10.5 | 7 | 3.5 | 0 | -3.5 | -7 | -10.5 | -14 |
|---|---|---|---|---|---|---|---|---|---|
| 17.5 | | 284 | 299 | 320 | 363 | 355 | 315 | 285 | |
| 14 | 284 | 305 | 321 | 341 | 381 | 379 | 339 | 305 | 310 |
| 10.5 | 282 | 312 | 328 | 339 | 390 | 391 | 352 | 317 | 317 |
| 7 | 305 | 323 | 335 | 343 | 392 | 394 | 354 | 331 | 334 |
| 3.5 | 312 | 331 | 342 | 352 | 398 | 400 | 367 | 329 | 336 |
| 0 | 313 | 337 | 353 | 363 | 408 | 406 | 379 | 339 | 345 |
| -3.5 | 302 | 319 | 338 | 349 | 394 | 393 | 362 | 320 | 324 |
| -7 | 290 | 305 | 329 | 341 | 382 | 388 | 357 | 317 | 320 |
| -10.5 | 282 | 301 | 323 | 335 | 376 | 380 | 352 | 308 | 302 |
| -14 | 268 | 288 | 308 | 322 | 363 | 363 | 337 | 293 | 290 |
| -17.5 | 264 | 283 | 300 | 311 | 345 | 353 | 324 | 280 | 280 |

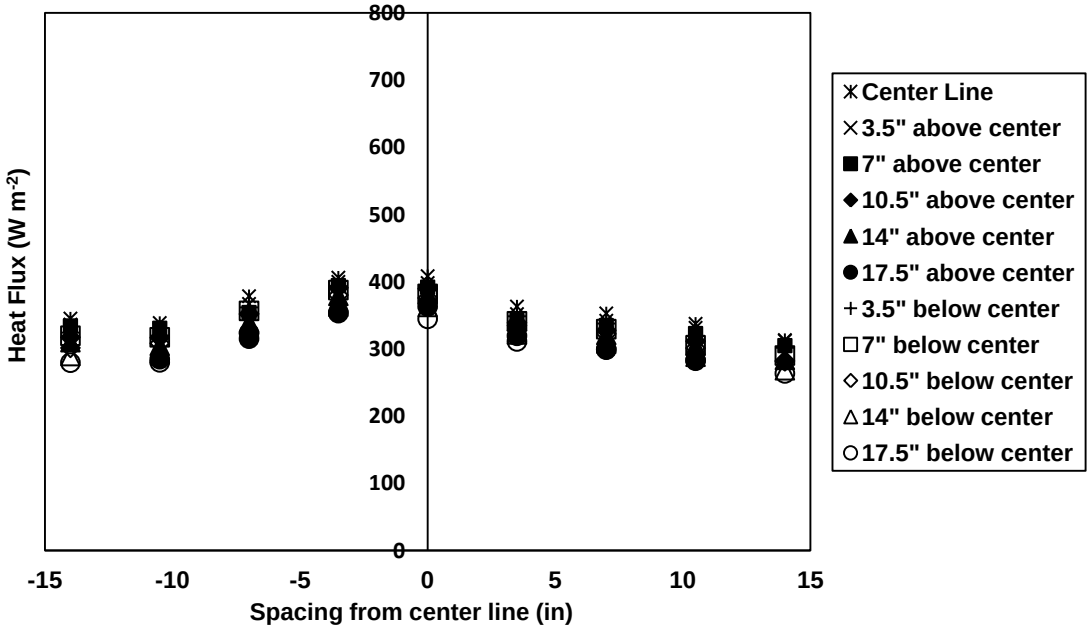


**Figure 8-1: Pyranometer readings on outside of glass for L = 1.38 m**

**Table 8-2 Pyranometer readings (W/m$^2$) 10 cm behind glass for L = 1.38 m**

| Spacing (in) | 14 | 10.5 | 7 | 3.5 | 0 | -3.5 | -7 | -10.5 | -14 |
|---|---|---|---|---|---|---|---|---|---|
| 17.5 | 201 | 209 | 216 | 225 | 226 | 266 | 237 | 212 | 200 |
| 14 | 207 | 214 | 223 | 229 | 262 | 269 | 238 | 212 | 202 |
| 10.5 | 214 | 218 | 225 | 229 | 214 | 271 | 244 | 220 | 208 |
| 7 | 218 | 224 | 231 | 236 | 271 | 279 | 254 | 225 | 217 |
| 3.5 | 220 | 228 | 237 | 240 | 272 | 284 | 259 | 231 | 223 |
| 0 | 223 | 233 | 241 | 245 | 279 | 289 | 263 | 236 | 228 |
| -3.5 | 216 | 228 | 238 | 245 | 280 | 284 | 262 | 231 | 224 |
| -7 | 207 | 221 | 231 | 239 | 271 | 277 | 253 | 223 | 217 |
| -10.5 | 200 | 214 | 224 | 232 | 264 | 272 | 252 | 218 | 211 |
| -14 | 194 | 208 | 218 | 227 | 258 | 266 | 246 | 209 | 205 |
| -17.5 | 184 | 198 | 212 | 219 | 250 | 258 | 238 | 204 | 198 |

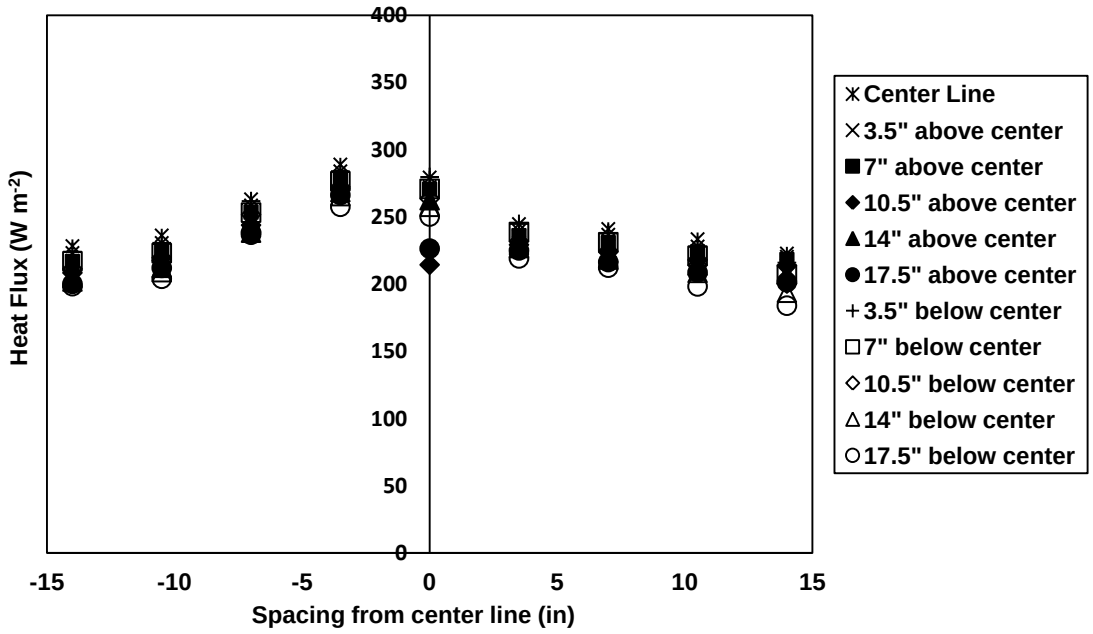


**Figure 8-2: Pyranometer readings 10 cm behind glass for L = 1.38 m**

**Table 8-3 Pyranometer readings (W/m2) 20 cm behind glass for L = 1.38 m**

| Spacing (in) | 14 | 10.5 | 7 | 3.5 | 0 | -3.5 | -7 | -10.5 | -14 |
|---|---|---|---|---|---|---|---|---|---|
| 17.5 | 143 | 157 | 163 | 174 | 197 | 205 | 191 | 178 | 160 |
| 14 | 156 | 165 | 169 | 180 | 208 | 201 | 201 | 185 | 169 |
| 10.5 | 159 | 170 | 174 | 185 | 212 | 214 | 208 | 183 | 176 |
| 7 | 166 | 176 | 180 | 190 | 211 | 222 | 214 | 183 | 184 |
| 3.5 | 178 | 184 | 187 | 196 | 227 | 223 | 219 | 192 | 192 |
| 0 | 178 | 188 | 191 | 200 | 232 | 227 | 229 | 198 | 203 |
| -3.5 | 167 | 192 | 193 | 203 | 231 | 235 | 235 | 212 | 209 |
| -7 | 178 | 193 | 194 | 209 | 237 | 208 | 238 | 197 | 181 |
| -10.5 | 143 | 192 | 194 | 208 | 224 | 249 | 242 | 185 | 208 |
| -14 | 136 | 192 | 195 | 205 | 231 | 246 | 239 | 180 | 206 |
| -17.5 | 147 | 193 | 196 | 199 | 224 | 221 | 239 | 184 | 210 |

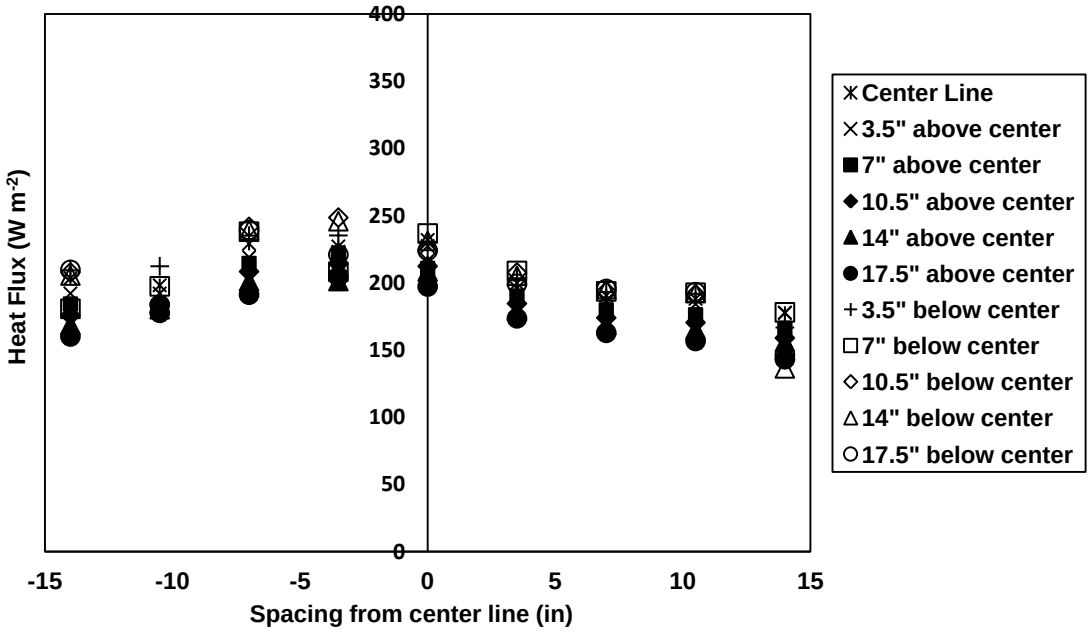


**Figure 8-3: Pyranometer readings 10 cm behind glass for L = 1.38 m**

**Table 8-4 Pyranometer readings (W/m$^2$) 30 cm behind glass for L = 1.38 m**

| Spacing (in) | 14 | 10.5 | 7 | 3.5 | 0 | -3.5 | -7 | -10.5 | -14 |
|---|---|---|---|---|---|---|---|---|---|
| 17.5 | 135 | 156 | 168 | 182 | 196 | 191 | 179 | 168 | 163 |
| 14 | 143 | 160 | 170 | 185 | 203 | 191 | 183 | 172 | 171 |
| 10.5 | 152 | 163 | 173 | 187 | 202 | 193 | 188 | 173 | 172 |
| 7 | 155 | 168 | 177 | 192 | 203 | 199 | 189 | 164 | 179 |
| 3.5 | 168 | 172 | 181 | 195 | 215 | 206 | 192 | 178 | 178 |
| 0 | 165 | 175 | 183 | 198 | 217 | 208 | 200 | 175 | 183 |
| -3.5 | 161 | 177 | 184 | 195 | 198 | 205 | 199 | 183 | 184 |
| -7 | 158 | 176 | 183 | 200 | 215 | 193 | 199 | 172 | 169 |
| -10.5 | 145 | 173 | 179 | 196 | 208 | 208 | 194 | 160 | 184 |
| -14 | 140 | 171 | 178 | 193 | 209 | 210 | 194 | 156 | 182 |
| -17.5 | 146 | 174 | 181 | 191 | 207 | 194 | 197 | 170 | 187 |

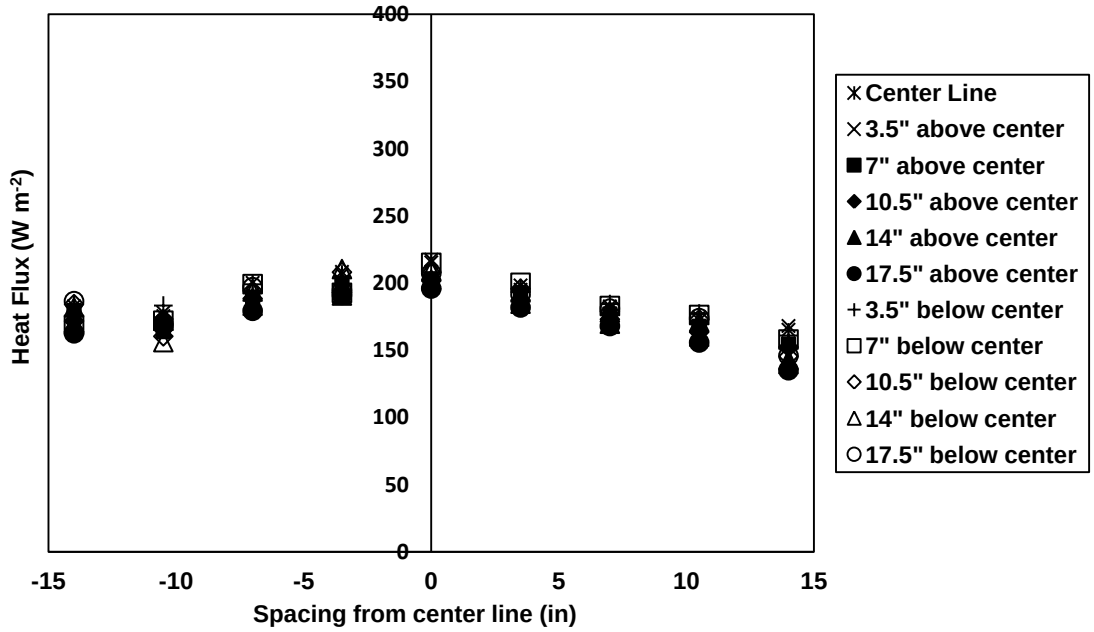


**Figure 8-4: Pyranometer readings 30 cm behind glass for L = 1.38 m**

**Table 8-5 Pyranometer readings (W/m$^2$) 40 cm behind glass for L = 1.38 m**

| Spacing (in) | 14 | 10.5 | 7 | 3.5 | 0 | -3.5 | -7 | -10.5 | -14 |
|---|---|---|---|---|---|---|---|---|---|
| 17.5 | 127 | 155 | 173 | 190 | 195 | 178 | 167 | 159 | 165 |
| 14 | 129 | 155 | 171 | 190 | 197 | 180 | 165 | 159 | 172 |
| 10.5 | 146 | 156 | 172 | 190 | 191 | 172 | 168 | 163 | 168 |
| 7 | 143 | 159 | 174 | 193 | 195 | 177 | 164 | 145 | 175 |
| 3.5 | 158 | 160 | 175 | 194 | 203 | 190 | 165 | 164 | 164 |
| 0 | 153 | 161 | 175 | 197 | 203 | 189 | 171 | 153 | 162 |
| -3.5 | 155 | 163 | 175 | 186 | 165 | 174 | 163 | 154 | 159 |
| -7 | 138 | 160 | 172 | 191 | 193 | 177 | 160 | 146 | 157 |
| -10.5 | 148 | 154 | 164 | 184 | 192 | 168 | 147 | 136 | 161 |
| -14 | 143 | 150 | 161 | 181 | 187 | 175 | 148 | 132 | 158 |
| -17.5 | 145 | 155 | 166 | 183 | 190 | 168 | 154 | 157 | 163 |

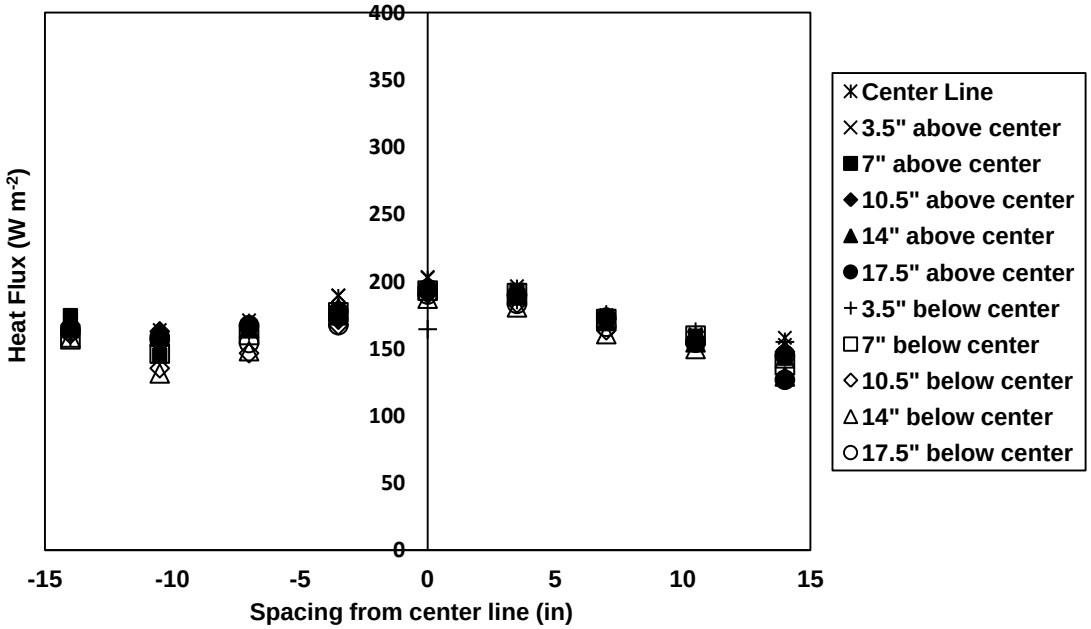


**Figure 8-5: Pyranometer readings 15 cm behind glass for L = 1.38 m**

## 8.3 Appendix C - Two Dimensional Mesh Visualization

The following figure represents a visual of the mesh used in the numerical model.

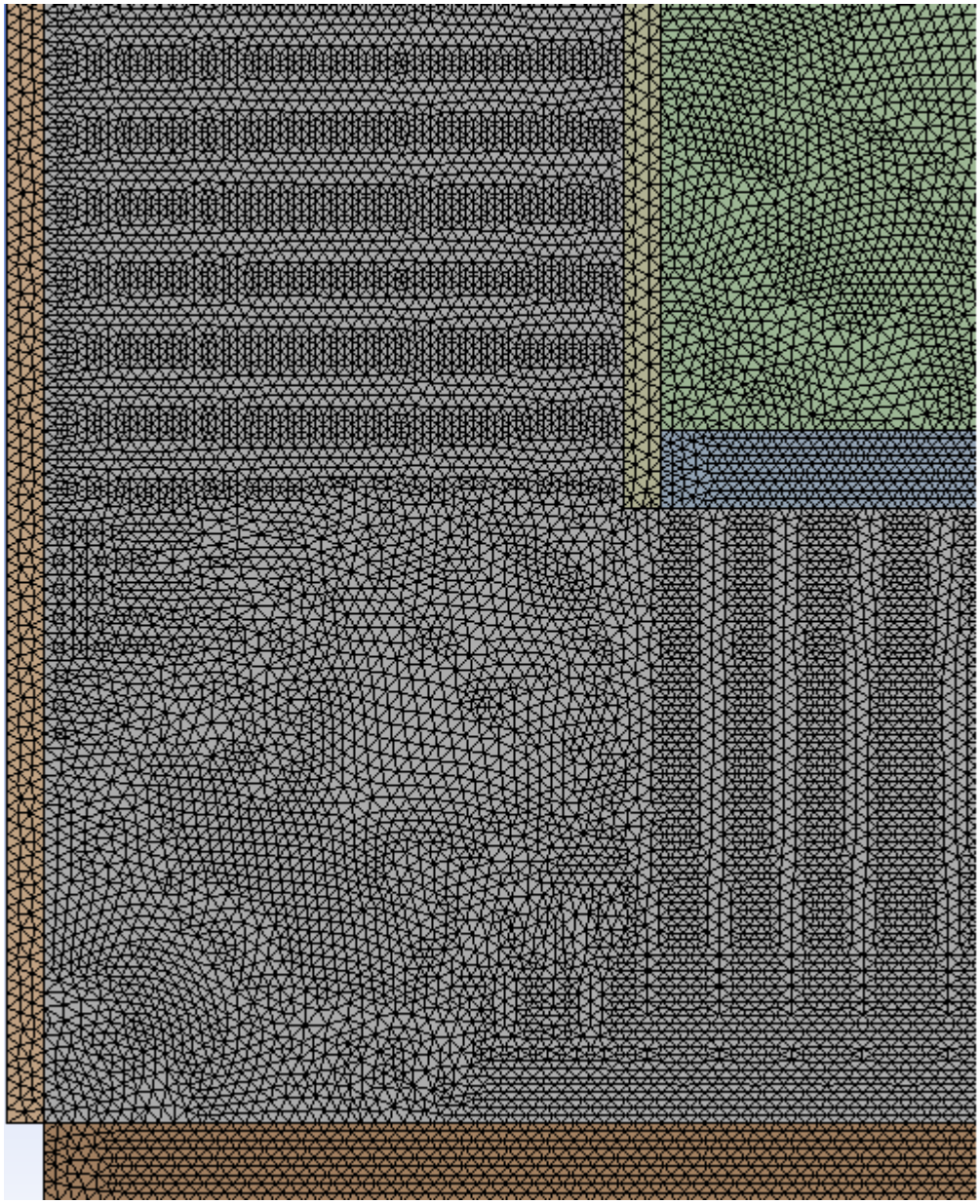

**Figure 8-6: Mesh used in the numerical model**

## 8.4 Appendix D - Numerical Results

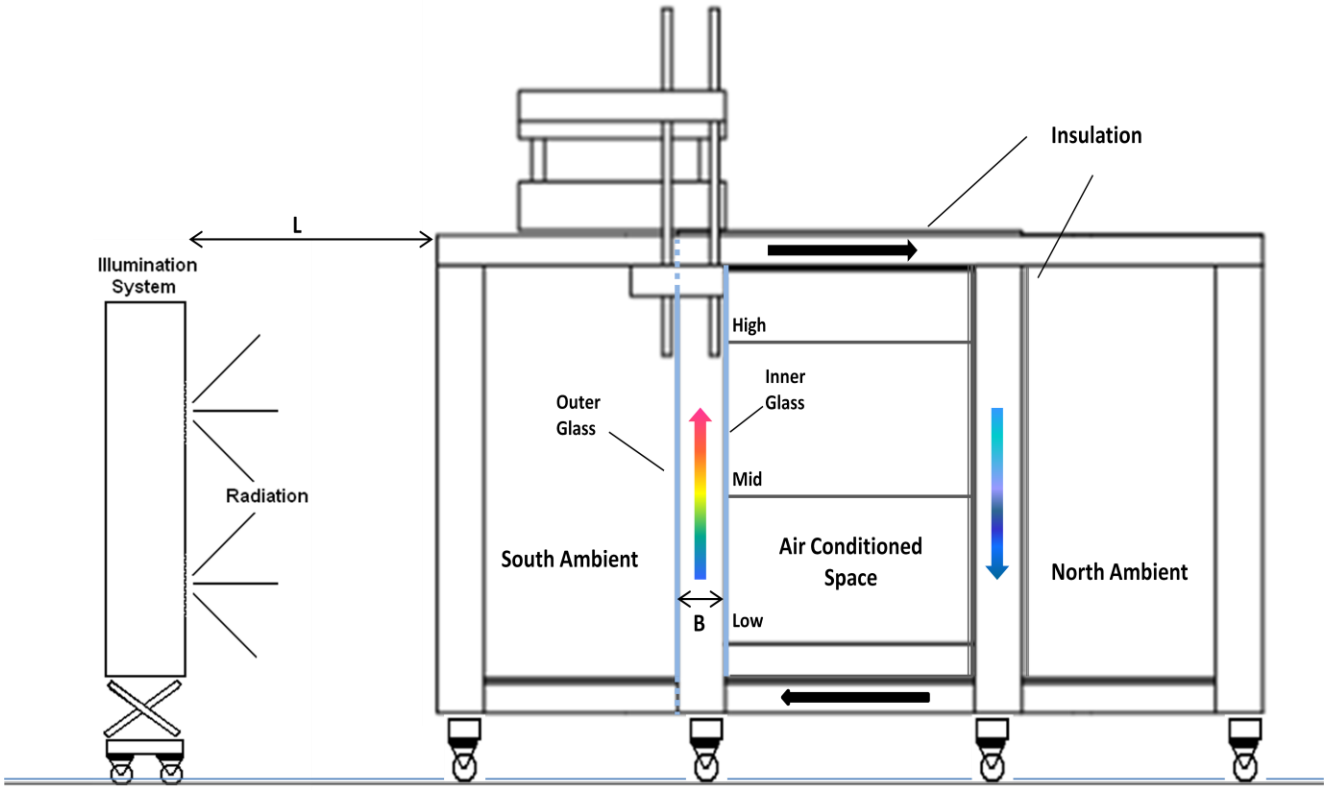


**Figure 8-7: Experimental Setup**

| Configuration | |
|---|---|
| Lite 1/4" (6mm) Clear | |
| Visible Light | |
| Transmittance (LT) | 88% |
| Reflectance - Outdoors (LR) | 8% |
| Reflectance - Indoors | 8% |
| Solar Energy | |
| Transmittance | 80% |
| Reflectance - Outdoors (ER) | 7% |
| U.V. Light | |
| Transmittance | 66% |
| Damage Weighted Index - ISO | 82% |
| U-Values | |
| Winter - Air | 1.02 |
| Summer - Air | 0.93 |
| Other Values | |
| Solar Heat Gain Coefficient (SHGC) | 0.84 |
| Shading Coefficient | 0.96 |
| Reflective Heat Gain - $BTU \cdot Hr^{-1} \cdot Ft^{-2}$ | 206 |
| Light to Solar Heat Gain Ratio | 1.05 |

| Configuration | |
|---|---|
| Lite 1/4" (6mm) Solarshield Grey | |
| Visible Light | |
| Transmittance (LT) | 45% |
| Reflectance - Outdoors (LR) | 5% |
| Reflectance - Indoors | 5% |
| Solar Energy | |
| Transmittance | 44% |
| Reflectance - Outdoors (ER) | 5% |
| U.V. Light | |
| Transmittance | 25% |
| Damage Weighted Index - ISO | 41% |
| U-Values | |
| Winter - Air | 1.03 |
| Summer - Air | 0.93 |
| Other Values | |
| Solar Heat Gain Coefficient (SHGC) | 0.59 |
| Shading Coefficient | 0.68 |
| Reflective Heat Gain - $BTU \cdot Hr^{-1} \cdot Ft^{-2}$ | 150 |
| Light to Solar Heat Gain Ratio | 0.76 |

**Table 8-6: Experimental Setup Glass Properties**

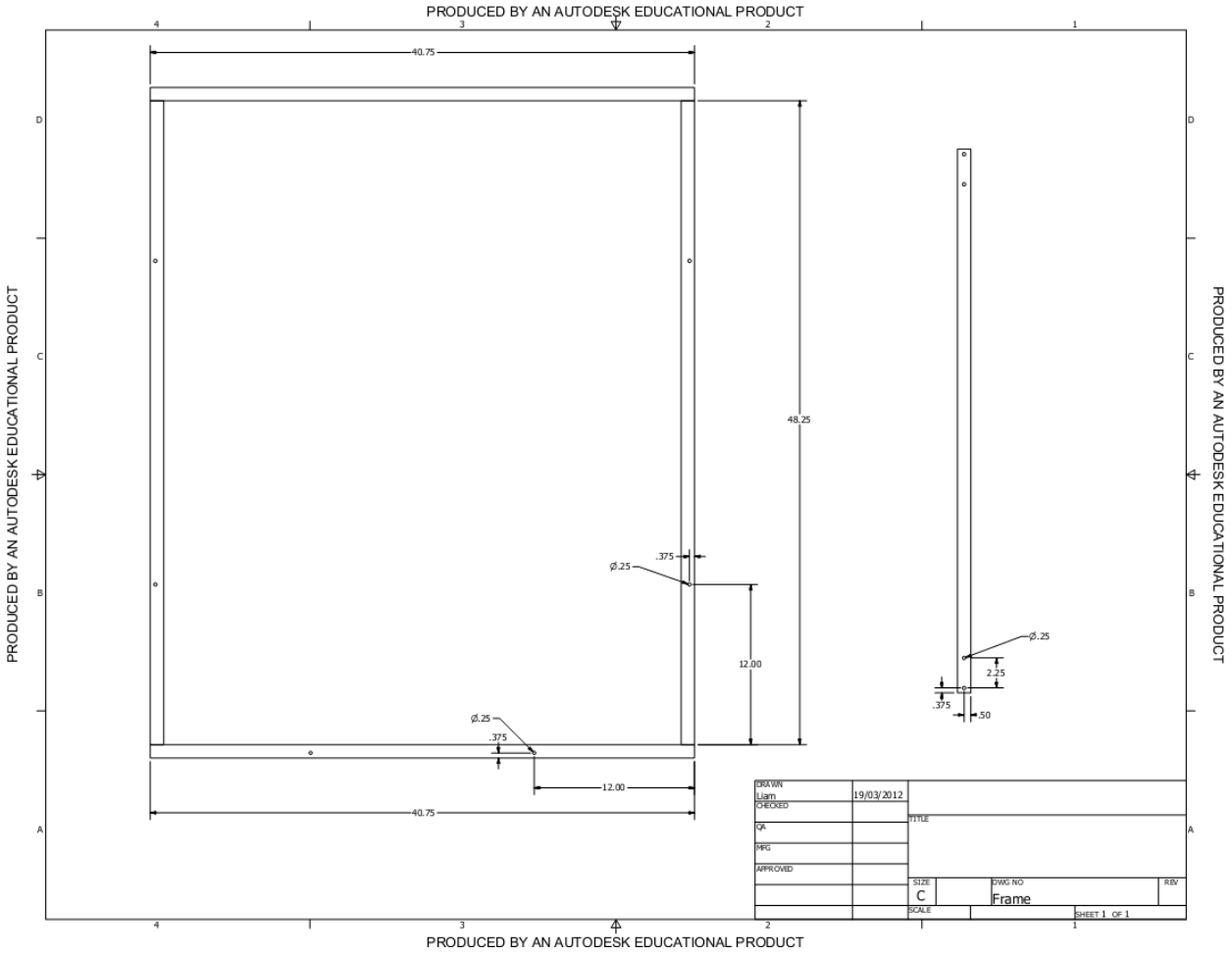


**Figure 8-8: Aluminum Frame Detail Drawing**

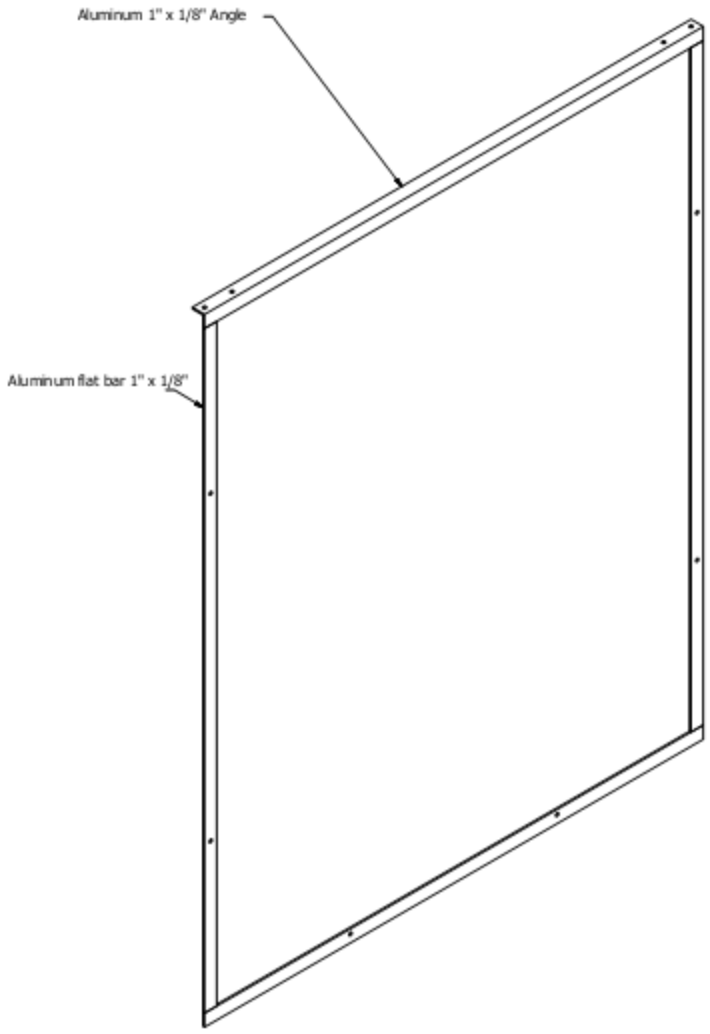


**Figure 8-9: Aluminum Frame Isometric**

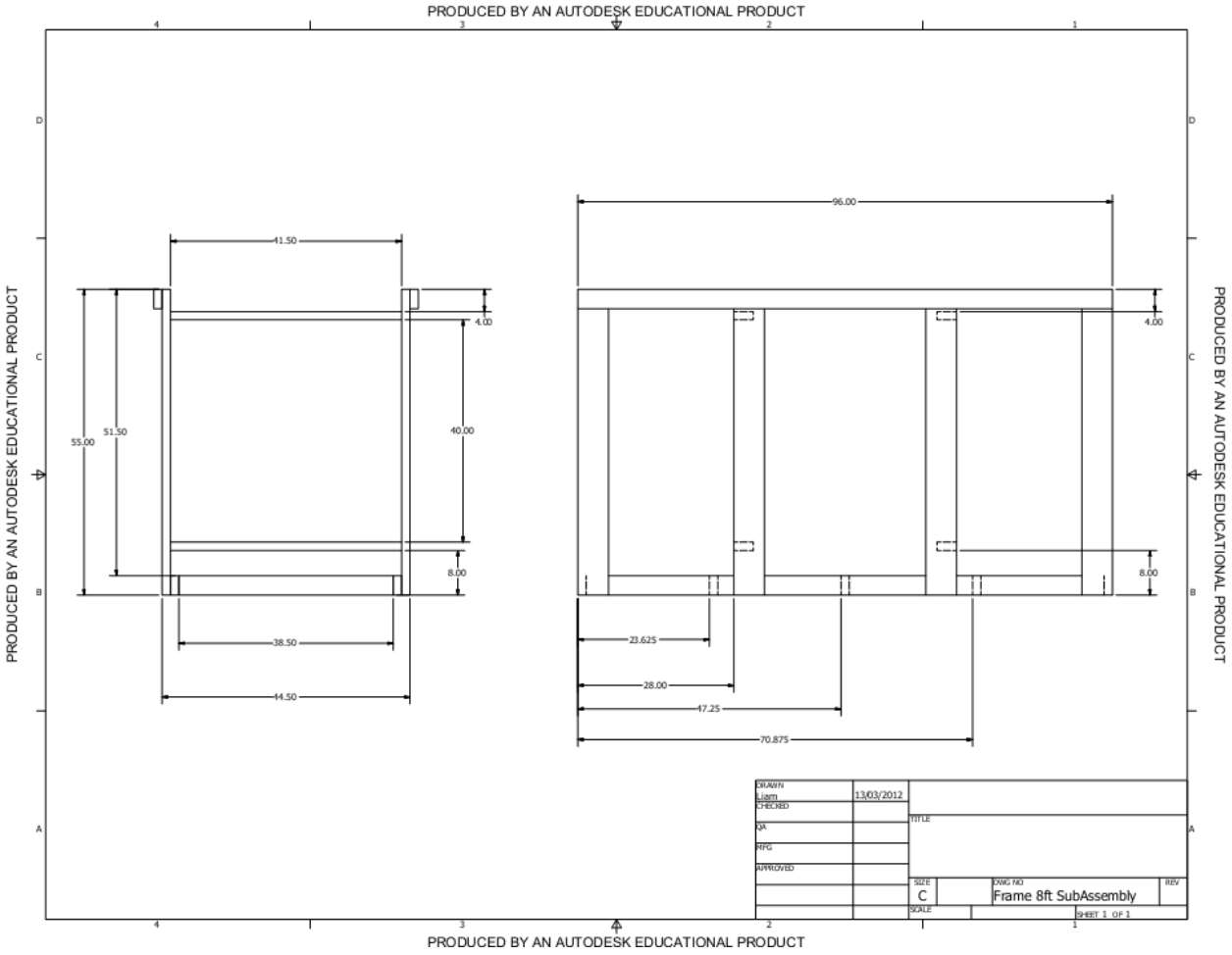


**Figure 8-10: Softwood Frame Detail Drawing**

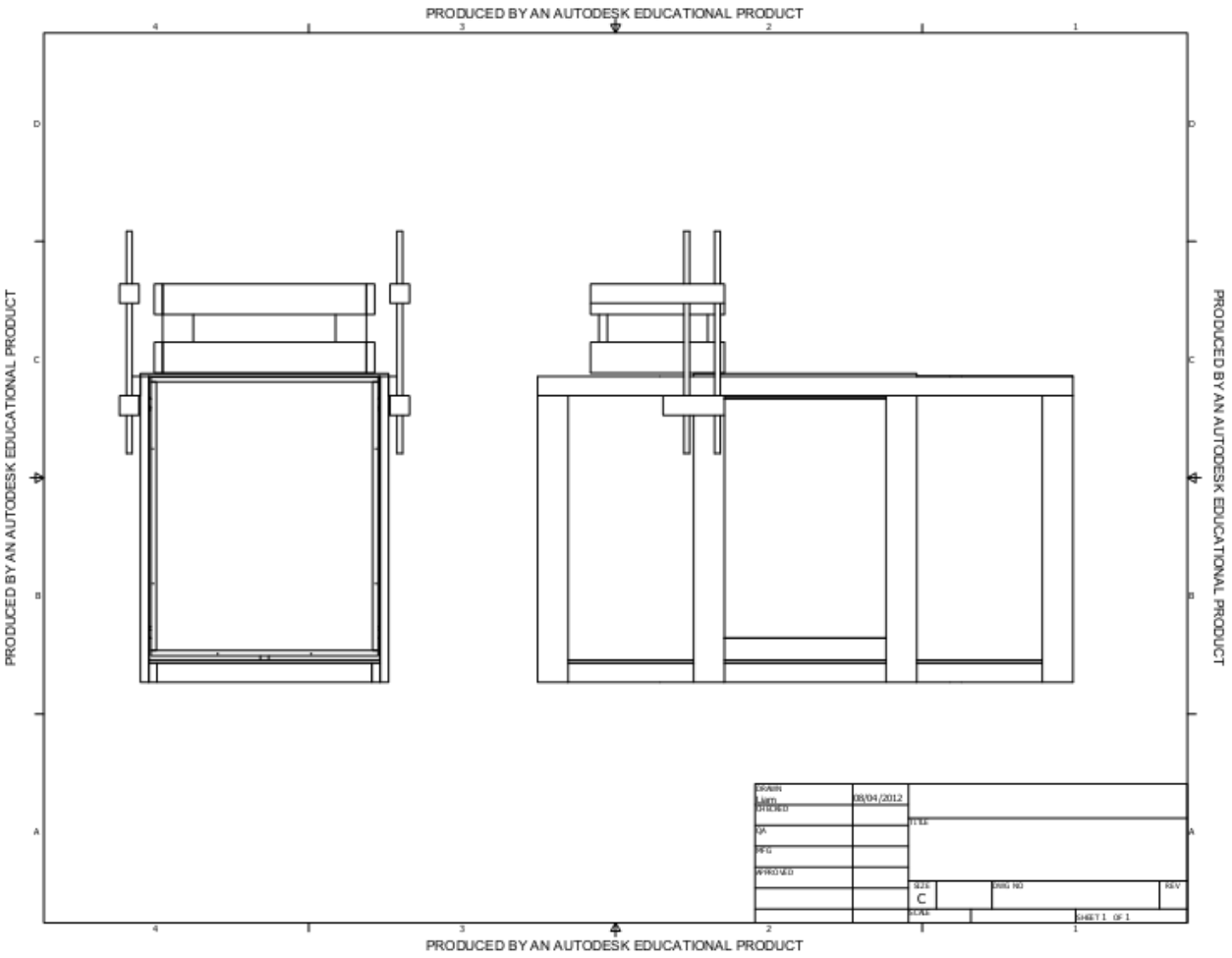


**Figure 8-11: Full Assembly Side Views**

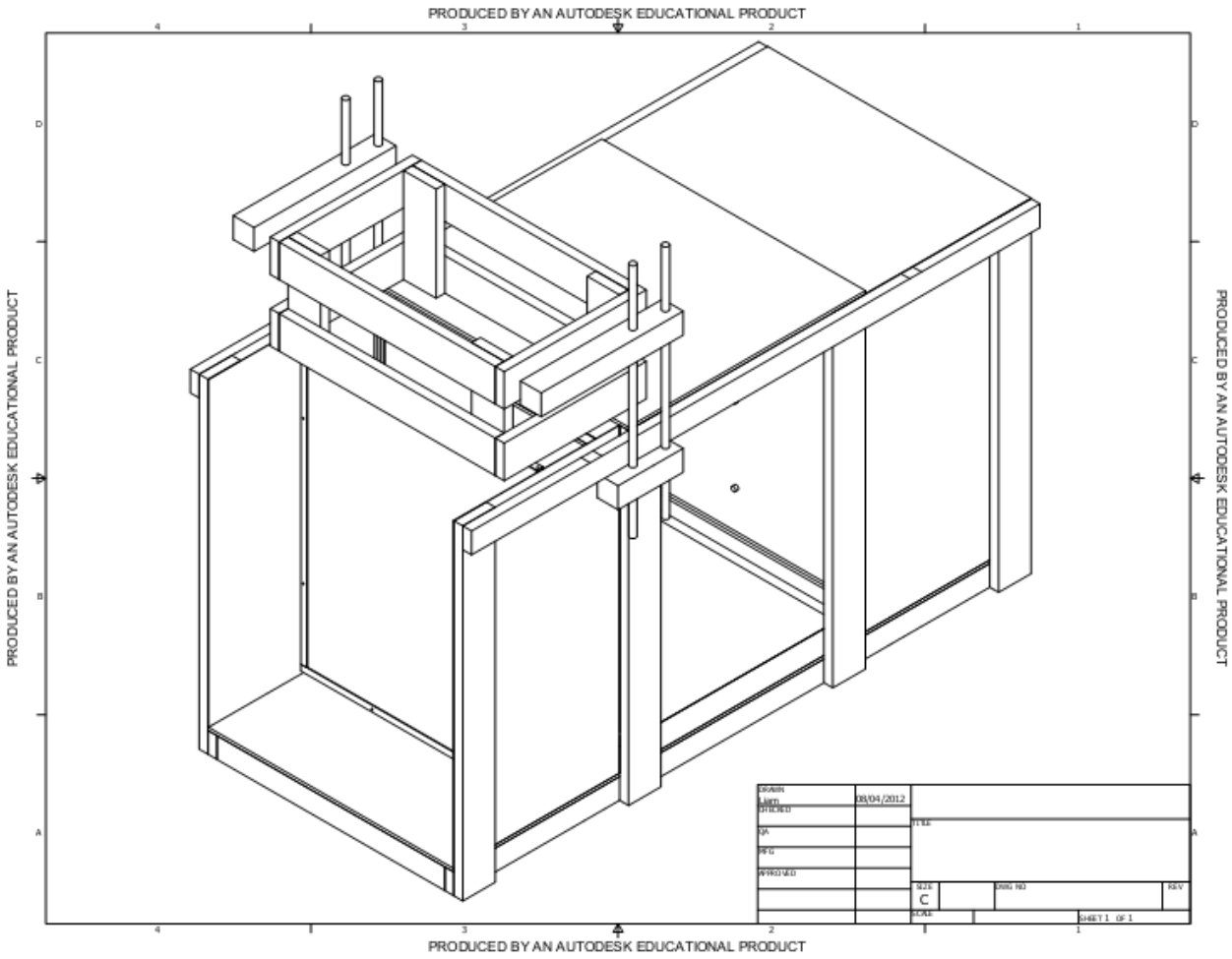


**Figure 8-12: Full Assembly Isometric View**

## 8.5 Appendix E - Case Study Calculations

**No TBZ South side Calculation:**

Single Glazing/Pane

Standard 6mm Clear Glass

SHGC 0.81 and U = 5 W/m$^2$.K

$$Q = U(T2 - T1) + q \qquad \textit{Eq. 8-6}$$

Where Q is heat coming into the conditioned space

U is the overall heat transfer coefficient

T2 is the inside temp; assumed to be 21$^o$C and T1 is the outside temp; assumed to be 0$^o$C.

q is the cooling needed to keep the conditioned space at 21$^o$C in Watts

Same formula with same temperature was used for the rest of the calculations below to obtain the amount of cooling required.

**Double Glazing/Pane**

6mm Clear Glass

SHGC = 0.70

U = 3.4 W/m$^2$.K

**Double Glazing/Pane with Low E-coating**

6mm Clear Glass

SHGC = 0.65

U = 3.0 W/m$^2$.K

**Double Glazing/Pane**

6mm Clear Glass

SHGC = 0.61

U = 2.6 W/m$^2$.K

**Double Glazing/Pane with Low E-coating**

6mm Clear Glass

SHGC = 0.53

U = 2.1 W/m$^2$.K

**No TBZ North side Calculation:**

Single Glazing/Pane

Standard 6mm Clear Glass

U = 5 W/m$^2$.K

$$Q = U(T2 - T1) \quad \textit{Eq. 8-7}$$

Same cases and values apply as in the case of south side.

Q is the amount of constant heat needed to keep the conditioned space at a comfortable temperature.

# 9. List of References

Aderson, R., C. Christensen & S. Horowitz. 2006. Analysis of Residential System Strategies Targeting Least-Cost Solutions Leading to Net Zero Energy Homes. ASHRAE.

Arons, D. (2000). *Properties and Applications of Double-Skin Building.* Massachusetts Institute of Technology.

Badescu, V. & B. Sicre (2003a) Renewable energy for passive house heating II. Model. *Energy and Buildings,* 35**,** 1085-1096.

--- (2003b) Renewable energy for passive house heating Part I. Building description. *Energy and Buildings,* 35**,** 1077-1084.

Badescu, V. & M. D. Staicovici (2006) Renewable energy for passive house heating model of the active solar heating system. *Energy and Buildings,* 38**,** 129-141.

Baumann, O., C. Reiser & J. Schafer (2009) LEED - The Green Building Rating System. *Bauphysik,* 31**,** 99-105.

Chantawong, P., J. Hirunlabh, B. Zeghmati, J. Khedari, S. Teekasap & M. M. Win (2006) Investigation on thermal performance of glazed solar chimney walls. *Solar Energy,* 80**,** 288-297.

DeHerde, C. a. (2004). *Double Skin facades for Office Buildings.* LUND University.

Erell, E. & Y. Etzion (2000) Radiative cooling of buildings with flat-plate solar collectors. *Building and Environment,* 35**,** 297-305.

Furbo, S., E. Andersen, S. Knudsen, N. K. Vejen & L. J. Shah. 2005. Smart solar tanks for small solar domestic hot water systems. 269-279. Pergamon-Elsevier Science Ltd.

Friedrich, K. (2011). Experimental and Numerical Investogation of Solar Air Flow Window. McMaster University.

Gan, G. H. (1998) A parametric study of Trombe walls for passive cooling of buildings. *Energy and Buildings,* 27**,** 37-43.

--- (2000) Effective depth of fresh air distribution in rooms with single-sided natural ventilation. *Energy and Buildings,* 31**,** 65-73.

--- (2006) Simulation of buoyancy-induced flow in open cavities for natural ventilation. *Energy and Buildings,* 38**,** 410-420.

Jaroš, C. Š. (2001). Numerical andExperimental Investigation of the Conditions in the Double SolarEnergy Façade. Sustainable and Solar Energy Conference.

J. Cuddihy, C. K. (2005). Energy use in Canada: Enviornmental impacts and opportunities in relationship to infrastructure systems. *Canadian Journal of Civil Engineering* , 32:1.

Lee, E. S. (2002). *High-Performance Commercial Building Façades. Building Technologies Program,.* Orlando Lawrence Berkeley National Laboratory (LBNL), University of California, Berkeley, USA.

M.A. Shameri, M. A. (2011). Perspectives of double skin facade systems in buildings and energy savings. *Renewable and Sustainable Reviews* , 1468-1475.

Natural Resources Canada. (2009, April 1). *Comprehensive Energy Use Database*. Retrieved October 20, 2011, from Natural Resources Canada: http://oee.nrcan.gc.ca/corporate/statistics/neud/dpa/comprehensive_tables/index.cfm?fuseaction=Selector.showTree

Pasquay, T. (2004). Natural ventilation in high-rise buildings with double facades, saving or wasting of energy. *Energy and Buildings* , 381-389.

R. Richman, K. P. (2010). Quantifying and predicting performance of the solar dynamic buffer zone (SDBZ) curtain wall thorugh experimentation and numerical modeling. *Energy and Buildings* , 522 - 533.

Richman R. C., K. (2009). A more sustainable curtain wall system: Analytical modeling of the solar dynamic buffer zone (SDBZ) curtain wall. *Buildings and Enviornment* , 1-10.

Saelens, D. (2002). *Energy Performance assesment of single story multiple-skin facades.*

Ternoey, S. e. (1985). *The Design of Energy-responsive Commercial Buildings.* New York: John Wiley.

Torcellini, P., S. Pless, M. Deru & D. Crawley. 2006. Zero Energy Buildings: A Critical Look at the Definition. U.S. Department of Energy.

Tyagi, V. V. & D. Buddhi (2007) PCM thermal storage in buildings: A state of art. *Renewable & Sustainable Energy Reviews,* 11**,** 1146-1166.

--- (2008) Thermal cycle testing of calcium chloride hexahydrate as a possible PCM for latent heat storage. *Solar Energy Materials and Solar Cells,* 92**,** 891-899.

Zamora, B. & A. S. Kaiser (2009) Optimum wall-to-wall spacing in solar chimney shaped channels in natural convection by numerical investigation. *Applied Thermal Engineering,* 29**,** 762-769.